# METAL ADDITIVE MANUFACTURING PROCESS-STRUCTURE-PROPERTY RELATIONAL LINKAGES USING GAUSSIAN PROCESS SURROGATES

A Dissertation

by

ROBERT N. SAUNDERS

Submitted to the Graduate and Professional School of
Texas A&M University
in partial fulfillment of the requirements for the degree of

DOCTOR OF PHILOSOPHY

| | |
|---|---|
| Chair of Committee, | Alaa Elwany |
| Co-Chair of Committee, | Dimitris Lagoudas |
| Committee Members, | Raymundo Arróyave |
| | John Michopoulos |
| Head of Department, | Lewis Ntaimo |

August 2022

Major Subject: Industrial Engineering

# ABSTRACT

Process-structure-property (PSP) relational linkages are necessary for designing, developing, and tailoring a material to exhibit desired properties, and ultimately, performance for a targeted application. Establishing PSP linkages typically involves building and testing materials from a given process until the desired properties are achieved. However, the process of generating and representing the data needed to establish these PSP linkages is often time intensive as it requires extensive experimentation and/or complex, multi-scale simulations. These PSP linkages are of particular interest for additive manufacturing (AM) processes due to the plethora of process parameters involved that are significantly more influential in the localization of microstructural morphologies, and the associated material properties, compared to those of conventional manufacturing processes. With sufficient understanding of PSP linkages, their control within AM can produce parts with previously unattainable properties, including spatial distributions of those properties at will.

The present works establishes and demonstrates a Gaussian process (GP) based framework to emulate experiments and simulations of AM PSP linkage components. The goal of this framework is to construct predictive surrogate models that significantly reduce the time to sample PSP linkages while maintaining a high predictive accuracy. The framework will consist of three primary components: 1) a multi-fidelity GP linking process parameters to printability and melt pool characteristics, 2) a multi-output GP linking the melt pool to microstructure statistics, and 3) a functional GP relating microstructure statistics to the mechanical properties. The application of the described framework will demonstrate a novel linkage directly from process parameters to microstructure properties. The results demonstrate approximately 95% accuracy in predicting mechanical properties for previously unseen process parameters that have been propagated through the PSP linkage. The use of GPs in the workflow limits the number of experiments/simulations needed, yields a reduced cost for acquisition of new predictions, and allows for a Bayesian treatment of the PSP linkages.

# DEDICATION

To my wife, Faith; my mother, Donna; and my grandparents, Gloria and Nelson.

# ACKNOWLEDGMENTS

I would like to begin by acknowledging the support of the Naval Research Laboratory (NRL) through the Edison graduate memorial training program and Virginia DeGiorgi for her help and support identifying a school and entering the program. I would also like to thank Edward Gorzkowski for his support as a branch head. I thank my section, Kirubel Teferra, Stephanie Wimmer, Gary Tan, Lukasz Kuna, and (formerly) Patrick Brewick, for their contributions; both technical and non-technical. Also from NRL, I thank Amit Bagchi and Yungchia (YC) Chen for their encouragement, feedback, and support throughout this process. I would like to thank John Michopoulos, for serving on the committee for this work, and the rest of the Computational Multiphysics Systems Lab, Athanasios Iliopoulos, John Steuben, Andrew Birnbaum, and Anna Kofer, for their technical contributions to this work. Finally, from NRL, I would like to thank Joseph Franke and Jose Mancias who supported this work while working at NRL during their summer breaks.

From Texas A&M University (TAMU), I would like to thank the rest of my committee, Dimitris Lagoudas, Alaa Elwany, and Raymundo Arroyave as well as their corresponding research groups. All have provided valuable feedback, technical contributions, and support throughout this process. In particular, I would like to acknowledge Mohamad (Mo) Mahmoudi, David Shoukr, Bing Zhang, Chen Zhang, and Xueqin Huang for helping me during my time in Texas at TAMU and their technical contributions.

Finally, I would like to acknowledge Celia Butler, Synopsys Inc, Ajit Achuthan, Clarkson University, and Saad Khairallah, Lawrence Livermore National Laboratory, for their technical contributions to this work.

# CONTRIBUTORS AND FUNDING SOURCES

## Contributors

This work was supported by a dissertation committee consisting of Professor Alaa Elwany (chair) of the Department of Industrial and Systems Engineering, Professor Dimitris Lagoudas (co-chair) of the Department of Aerospace Engineering, Professor Raymundo Arróyave of the Department of Materials Science and Engineering, and Dr. John Michopoulos of the U.S. Naval Research Laboratory (NRL).

Finite element model description and data in Chapter 2 was provided by Dr. Athanasios Iliopoulos, NRL. Experiment description and data in Chapter 2 was provided by Anna Kofer and Dr. Andrew Birnbaum, NRL. In Chapter 4, Dr. Bo Wang, University of Leicester, shared implementation details for the functional Gaussian process, Dr. Celia Butler, Synopsys, provided meshed microstructures, and Dr. Athanasios Iliopoulos, NRL, shared the CDIM code for microstructure generation. The CAFE model in Chapter 3 and 4 was provided by Dr. Kirubel Teferra, NRL.

All other work conducted for the dissertation was completed by the student independently.

## Funding Sources

Partial support for this work was provided by the Office of Naval Research through the Naval Research Laboratory's (NRL) core funding. Additional support was provided by the NRL Edison Graduate Memorial Training Program. This work was supported in part by high-performance computer time and resources from the DoD High Performance Computing Modernization Program.

TABLE OF CONTENTS

LIST OF FIGURES

FIGURE Page

# LIST OF TABLES

TABLE Page

# 1. INTRODUCTION*

## 1.1 Additive Manufacturing

Additive manufacturing (AM) is an advanced manufacturing process whereby topological information from 3D models is translated into a real part by joining material, typically in a layer-by-layer fashion. Much of the work in AM has been accomplished in the past two decades but the ideas used in AM can be dated to as far back as the 1860s.[1] AM is referred to by many names in the literature including, but not limited to, 3D printing, rapid prototyping, and layer manufacturing.[2, 3, 1, 4] The general AM process has, however, been specifically defined by ISO/ASTM standards to be the "process of joining materials to make parts from 3D model data, usually layer upon layer, as opposed to subtractive manufacturing and formative manufacturing methodologies", which gives the area of AM a very broad scope. Likewise, by the same standards, major AM processes can be generalized into seven categories: fused deposition modeling (FDM), inkjet printing (IJP), laminated object manufacturing (LOM), laser engineered net shaping (LENS), stereolithography (SLA), selective laser sintering (SLS), and three-dimensional printing (3DP).[2, 5] As with the naming convention for AM, the naming of the processes can vary widely[1], where, for example, technologies that all use laser processing for metallic materials can be referred to by different names depending on how the powder is fed and melted.[6, 7, 8] AM can utilize a vast range of materials from plastics to metals to ceramics to foods and other biological/polymeric materials.[9, 10, 11, 12, 4] Typically, certain classes of materials are printed with certain method (*e.g.*, metals with SLS or LENS, plastics with FDM, *etc.*) but this is not a strict guideline and as research in the area expands, materials able to be printed using a given AM method will also expand.[13, 11] A summary of the classification of AM processes can be seen in figure 1.1 and the focus of this work will primarily be on powder bed fusion (PBF) and in particular, DMLS and SLM technologies for metallic materials.

*Portions of this chapter have been reprinted with permission from R. N. Saunders, "Metamaterials Using Additive Manufacturing Technologies," Def. Tech. Inf. Cent., no. NRL/MR/6353–20-10,057, 2020.

| CATEGORIES | TECHNOLOGIES | PRINTED "INK" | POWER SOURCE | STRENGTHS / DOWNSIDES |
|---|---|---|---|---|
| Material Extrusion | Fused Deposition Modeling (FDM) | Thermoplastics, Ceramic slurries, Metal pastes | Thermal Energy | • Inexpensive extrusion machine<br>• Multi-material printing<br>• Limited part resolution<br>• Poor surface finish |
| | Contour Crafting | | | |
| Powder Bed Fusion | Selective Laser Sintering (SLS) | Polyamides /Polymer | High-powered Laser Beam | • High Accuracy and Details<br>• Fully dense parts<br>• High specific strength & stiffness<br>• Powder handling & recycling<br>• Support and anchor structure<br>• Fully dense parts<br>• High specific strength and stiffness |
| | Direct Metal Laser Sintering (DMLS) | Atomized metal powder (17-4 PH stainless steel, cobalt chromium, titanium Ti6Al-4V), ceramic powder | | |
| | Selective Laser Melting (SLM) | | | |
| | Electron Beam Melting (EBM) | | Electron Beam | |
| Vat Photopolymerization | Stereolithography (SLA) | Photopolymer, Ceramics (alumina, zirconia, PZT) | Ultraviolet Laser | • High building speed<br>• Good part resolution<br>• Overcuring, scanned line shape<br>• High cost for supplies and materials |
| Material Jetting | Polyjet / Inkjet Printing | Photopolymer, Wax | Thermal Energy / Photocuring | • Multi-material printing<br>• High surface finish<br>• Low-strength material |
| Binder Jetting | Indirect Inkjet Printing (Binder 3DP) | Polymer Powder (Plaster, Resin ), Ceramic powder, Metal powder | Thermal Energy | • Full-color objects printing<br>• Require infiltration during post-processing<br>• Wide material selection<br>• High porosites on finished parts |
| Sheet Lamination | Laminated Object Manufacturing (LOM) | Plastic Film, Metallic Sheet, Ceramic Tape | Laser Beam | • High surface finish<br>• Low material, machine, process cost<br>• Decubing issues |
| Directed Energy Deposition | Laser Engineered Net Shaping (LENS) Electronic Beam Welding (EBW) | Molten metal powder | Laser Beam | • Repair of damaged / worn parts<br>• Functionally graded material printing<br>• Require post-processing machine |

Figure 1.1: Classification of AM processes by ASTM International. Reprinted from [14].

While AM has been around for decades, the technology remains an area of critical technological and strategic importance to the United States government (USG) and its allies.[15] AM has been actively researched for the past decade, but the adoption of AM, particularly of metals, in practice has been slow, in part due to a lack of understanding of the performance of as-built AM parts and the challenges with qualification/certification that stem from this lack of understanding.[6] The Office of the President of the Unites States recently set out to address this lack of understanding in AM with AM Forward, a partnership between the USG and the manufacturing industry to conduct research to improve the performance of AM techniques.[16] While this effort primarily focuses on lowering the cost and increasing the quality and adoption of AM parts in industry, there are additional USG-wide efforts to utilize AM technologies to create a more secure and resilient supply

chain.[17, 18, 19] In addition to these efforts, the US Department of Defense has identified AM as a crucial technology needing further development for US national security with the ability to create lighter, stronger, and more resilient components to better prepare and protect Warfighters.[20]

AM has gained popularity in both experimental [6, 8] and computational [21] domains recently as it has the potential to remove many of the design constraints imposed by traditional manufacturing processes and address the issues highlighted above. This can, in part, be attributed to the reducing cost of programmable controllers, lasers, and computer-aided design (CAD) software.[14] The process of creating a part to be built by AM begins with 3D solid modeling as a CAD file which is then sliced into many discrete layers that are used as inputs to the AM machine to build the part. The largely digital workflow of the AM process allows for significant design and geometric flexibility with high dimensional accuracy. The AM process is also cost efficient as there is no need for assembly of parts and there is very little waste material.[14, 13] Additionally, AM processes can be scaled to print parts that range from the nano/micrometer scale [22, 23, 24] to the scale of meters.[25, 26]

The two most popular categories of metal AM are powder bed fusion and directed energy deposition. These processes typically involve a metal powder being spread or sprayed then a laser or electron beam is used to melt the powder in specific locations within a layer.[14] The molten material then cools and solidifies to create the desired geometry of a layer. This process is repeated until a full part is complete. The repeated thermal cycling of the powder and underlying solidified material in conjunction with the high thermal gradients is known to create microstructures that can be vastly different from conventionally manufactured components.[6, 27] Additionally, the AM process can lead to parts containing numerous defects.[8] Thus, it is critical to understand and control the AM process in order to create high quality, defect-free microstructures with desirable properties.[28] The foundation of this is to understand how AM process parameters influence the resulting melt pool and how that then influences the microstructure and resulting mechanical properties.[29]

## 1.2 Process-Structure-Property Relational Linkages

The process used to manufacture a material governs its morphological structure, which in turn drives the values and spatial distributions of the properties of the processed material and consequently its performance. Process-structure-property (PSP) relational linkages are necessary for designing, developing, and tailoring a material to exhibit desired properties, and ultimately performance, for a targeted application.[30] Establishing PSP linkages typically involves building and testing materials from a given process until the desired properties are achieved. However, the process of generating and representing the data needed to establish these PSP linkages is often difficult as the process is somewhat slow and expensive so it is challenging to obtain sufficient data using experimental methods alone.[31] An alternative to these experiments is to leverage one of numerous simulation capabilities.[32, 33, 34, 35, 21, 36] While these simulations can reduce the data collection burden, high fidelity simulations can still be expensive and low fidelity simulations can generate large amounts of data that present analysis and management difficulties.

One of the most prominent, emerging fields that call for PSP linkages is AM.[37, 38, 39, 28] As stated above, the texture morphologies produced by AM, particularly in metals at the microscale, can vastly differ from their conventionally manufactured counterparts. These differences often lead to undesired (or unexpected to say the least) properties in the finished part. With adequate understanding of PSP linkages in AM, these differences can be used to enhance the resulting properties to previously unattainable levels [27]. As with conventional materials, many works have attempted to understand PSP relational linkages in AM using experiments [40] and high-fidelity, multi-scale simulations [34, 35], which can achieve high accuracy predictions. While these simulations are generally less costly than their corresponding experiments, they can still have long run times, especially with high-fidelity, multi-scale simulations that provide the most physically consistent and accurate results. As a consequence of their high computational cost and high accuracy, these simulations are well suited gain increased insight into the underlying physics of the problem, but are not well suited generate large quantities of simulation results required for problems in optimization and uncertainty quantification (UQ) [41] nor problems in online, real

time production updating.[42] This challenge can be addressed through proper use of materials informatics and machine learning (ML) [37, 38, 43].

### 1.3 Machine Learning for AM and PSP Linkages

Recent advances in the field of data science and data analytics have made managing, interpreting, and extracting information from “big data" a more tractable activity.[44, 45, 46, 47, 48] The process of applying data science principles to materials science and engineering is referred to as *materials informatics* [49, 50, 51, 52] and typically involves the use of machine learning (ML) and artificial intelligence (AI) techniques [51, 46, 48]. The advancement and adoption of materials informatics has provided notable potential to streamline and accelerate the determination of process-structure (PS) [53], structure-property (SP) [54, 55, 56], and even full PSP [57] linkages in conventionally manufactured materials. The extension of these principles to AM is a natural one and, as one could expect, ML is being leveraged extensively in AM.[58, 59, 60, 61, 62]

One prominent use of ML in AM is *in-situ* process monitoring.[63] By monitoring the process and collecting the data, ML models can be trained to predict thermal history and possible defect formation (*i.e.*, printability), and update the process to create high quality builds with desired properties or performance.[64, 65, 66] However, this work involves the continued collection of experimental data, which can be costly and time consuming, in order to train the ML models. A less-costly alternative is to use utilize one or more of the plethora of available modeling techniques that have been developed to simulate every level of the AM process.[35, 21] However, these models generally fall into one of two paradigms: fast and approximate or slow and accurate. In all cases, there will be some level of inaccuracy and uncertainty introduced by the modeling assumptions with more accurate models generally having fewer assumptions.[67] In the case of lower fidelity models, ML methods may not be necessary as the models can be interrogated relatively easily due to the low data acquisition cost but these models will, of course, have a lower accuracy. Thus, it is desirable to utilize higher fidelity models to the maximum extent. However with higher fidelity models, this can be prohibitively costly. As such, many authors implement ML or surrogate models, such as Gaussian process (GP) models, to interrogate the physics-based model, quantify

uncertainty, and calibrate the model parameters.[68, 69, 70, 71, 72, 73, 74, 75, 76, 77, 78] In doing so, the accuracy of the high fidelity model can be mostly preserved while the cost to acquire new (interpolated) data is reduced significantly. While GP models do make assumptions about the normality of the underlying data distribution, they allow ML models with relatively high accuracy to be trained with only a small data set. Furthermore during the pre-processing steps of training, the application of appropriate data transformations can result in output data that approximately follows a standard Normal distribution.

There are a significant number recent articles which discuss how AM PSP experiment and simulation capabilities can all be linked together using ML.[34, 8, 79, 80] However, in practice and to the authors' knowledge, only Wang *et al.* [75] have successfully demonstrated a full ML framework for PSP linkages in AM. In their work, the authors create Kriging surrogate models of thermal finite element (FE), phase field (PF), and fast Fourier transform (FFT) crystal plasticity finite element (CPFE) models then adjust those models using experiment data and propagate uncertainty through the surrogate models. The authors show a single demonstrative example using Ti-6Al-4V fabricated with selective electron beam melting (SEBM) of how uncertainty can propagate through the system and affect mechanical property predictions. While the authors demonstrate good validation scores for the thermal surrogate model, no information is presented about the accuracy of the microstructure and mechanical models. Likewise, no information is given about the number or type of experiments used to adjust the surrogate models. Regardless, a more desirable ML framework would not necessitate adjust of surrogates by experiments after the surrogate has been trained.

### 1.4 Overview

As such, this work will demonstrate a Gaussian process (GP) based framework to create PSP linkages in AM. The focus here will be on the laser powder bed fusion (L-PBF) process using 316L stainless steel, but the framework will be developed in such a way that it is applicable to other AM processes and material systems. The ML-based PSP linkages in this work will largely be based on mechanistic models [81] and, as a result, GPs are utilized since they are well suited to

operate with small datasets that will come from mechanistic models and experiments in AM.[82] This will be done in four stages. First, chapter 2 will show the development of multi-fidelity GP (MFGP) surrogates for classifying “printability" and then predicting (via regression) the melt pool dimensions for “good" prints from the AM process parameters. Following this, chapter 3 will describe a method to use the predicted melt pool geometry to drive a cellular automata finite element (CAFE) model. From the CAFE model, microstructure statistics such as grain size, shape, and orientation can be extracted and used to create a multi-output GP that links the melt pool to microstructure statistics. In chapter 4, the microstructure statistics will be related to microstructure mechanical properties using a functional GP (fGP). This fGP will be trained using crystal plasticity finite element (CPFE) data and have the ability to predict the full stress-strain history for a given microstructure rather than simple, scalar quantities, such a yield strength or hardening modulus. Finally in chapter 5, the linking of the developed surrogate models will be demonstrated. An overview of the framework is shown in figure 1.2. In each chapter, a brief overview of the literature in that modeling area will be given followed by a presentation of physics-based modeling and GP surrogate modeling methods used, results, and a summary. Chapter 6 will provide an overall summary of what has been accomplished and future direction for the linking, use, and extension of the developed PSP surrogate models.

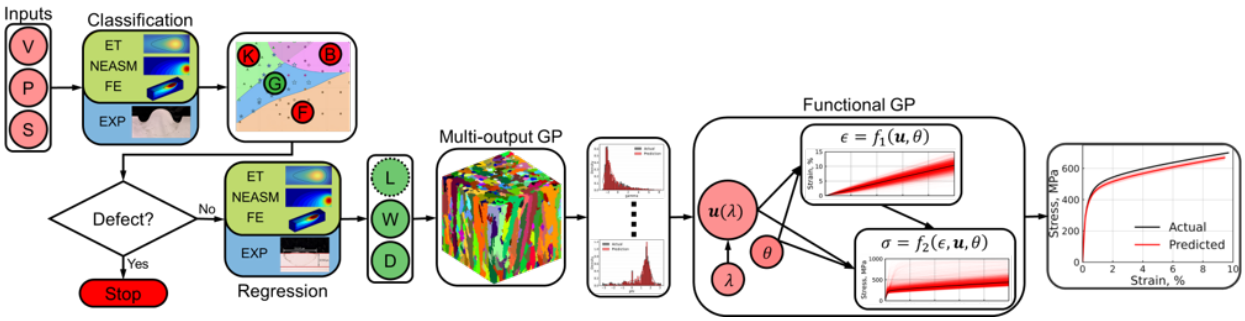


Figure 1.2: Relational AM process-structure-property surrogate framework being developed.

# 2. AM PROCESS MODELING SURROGATE

## 2.1 Introduction

In order to improve the performance of AM parts, particular metallic parts, the type of defects that arise during manufacturing and the reason for the defects must be better understood.[8] A key aspect to understanding the defects that are formed is understanding how the AM process parameters influence the resulting melt pool, or the liquid interface between the powder particles and the energy source.[29, 83] Too little energy being deposited will result in a melt pool not being formed, while a high energy will result in unsteady melt pool dynamics that can have unintended consequences.[6] In both cases, porosity defects will occur. In the no melting case, a lack of fusion defect can form and lead to a lower density part with irregular-shaped voids from unmelted powder. In the high energy case, defects, such as keyholing and balling/beading, can lead to entrapped gas and again result in a part with a lower density. In order to avoid these defects, the so-called *printability* needs to be assessed. Printability in this work is defined as the the process parameter map that can tell whether or not a porosity defect (*i.e.*, lack of fusion, keyholing, balling/beading) will occur for a given set of process parameters.[84, 64, 73, 65, 66, 85]

Many of the developed AM modeling capabilities focus solely on predicting the thermal history and corresponding melt pool geometry as functions of input process parameters.[86] These process models range from analytical [87] and semi-analytical methods [88, 89, 90, 91, 92] to finite element/difference models [93, 94, 95, 96, 97, 98, 99, 73] to multi-physics models at the scale of the metal powder [100, 101, 102, 103, 104, 105, 106]. GPs, as discussed, are a popular tool to emulate AM process models as they limit the number of simulations required and can provide accuracy comparable to the model they are emulating at a nearly negligible computational cost.[71, 73, 83]

A popular variation of the standard GP is the multi-fidelity GP (MFGP) developed by Kennedy and O'Hagan [107], commonly referred to as the Kennedy-O'Hagan or KOH model. In this framework, multiple sources of information at varying degrees of fidelity can be incorporated into a

single model. This limits the number of expensive simulations and/or experiments needed to build a model by leveraging information from cheap low fidelity solutions to the same problem. One example of this is using a few experiments to adjust a computer simulation.[108, 109] Recently, Mahmoudi *et al.* [70] applied this same methodology to a finite element (FE) AM process model to perform calibration of the model parameters and were able to achieve a high predictive accuracy.

In this chapter, an MFGP scheme that fuses information from experiments and multiple fidelities of simulations is shown. Two MFGPs are shown, one that performs regression to determine melt pool dimensions and another that performs classification to determine printability. The MFGPs are trained using a combination of experiments and simulations for a model material of 316L stainless steel, and the data generation is scaled based on the fidelity (*i.e.*, a few experiments, but many analytical solution data points). In doing, so the MFGP is made to be as efficient as possible when compared to a standard single fidelity GP. The remainder of this chapter will be structured as follows: section 2.2 overviews the AM process models utilized to generate data; section 2.3 provides a brief overview of the MFGP regression along with a novel MFGP classification approach; section 2.4 explains the data generation process from the models as well as how the regression and classification models are trained; section 2.5 shows the validation of the MFGP against a test set of experiments, demonstrates how different combinations of fidelities can yield the best overall model, and analyzes how each process model contributes to the overall MFGP; and finally section 2.6 summarizes the process surrogate model.

## 2.2 AM Process Modeling

This work utilizes 4 different fidelity information sources to generate the data needed to train the MFGPs. These are, namely, the analytical solution of Eager and Tsai [87], the Naval Research Laboratory (NRL) enriched analytical solution method [88, 89], a conduction-based FE model implemented in COMSOL, and laser powder bed fusion (L-PBF) experiments. The Eager-Tsai and NRL enriched analytical solution method are both briefly detailed below and the interested reader is referred to the referenced works for full details. The COMSOL FE model and experiments are detailed in full as they are both previously unpublished. The computational models are setup to

simulate the L-PBF process with 316L stainless steel as used in the experiments. Additionally, each model takes as input the 316L material properties and 3 process parameters, namely the laser power, velocity, and spot size[1]. Note that none of the simulations are specifically calibrated to the experiments and only use material parameters obtained from literature for a general 316L material. Temperature fields from each simulation are used to extract melt pool dimensions once a steady state thermal solution is achieved. Due to the high acquisition cost of the higher fidelity information and limitations of the lowest fidelity model, only single-track simulations are considered to maintain consistency between the fidelities.

### 2.2.1 Eager-Tsai Analytical Solution

The Eager-Tsai (ET) analytical solution is the lowest fidelity source used in this work and calculates the temperature field due to a traveling Gaussian distributed heat source on a semi-infinite plate and uses the calculated temperature field to compute melt pool dimensions. The solution is based upon fundamentals of heat transfer, albeit with a number of simplifying assumptions, such as non-temperature dependent material properties and only heat conduction. The ET solution was originally developed to describe the impact of welding process parameters on the geometry and temperature distribution of weld melt pools.[110] However, it can be readily applied to develop a first order approximation for temperatures in the L-BPF process since L-PBF can be thought of as a repetitive micro-welding process.[111, 85, 112] While the ET solution is not highly accurate for predicting all aspects of the L-PBF process, it is extremely fast and takes very little computational resources thus providing a good starting point for further analysis. A single simulation can run in seconds.

### 2.2.2 NRL Enriched Analytical Solution Method

The NRL Enriched analytical solution method (NEASM) was developed by modifying the ET solution to incorporate several enrichments to better capture the features seen in the AM process. These are: 1) using the linear heat equation to approximate the non-linear heat equation solution

[1]More specifically, spot size is used to denote the distance equivalent to four standard deviations of a Gaussian beam profile, commonly referred to as D4$\sigma$

via fixed point iteration, 2) using the method of images to account for finite domains, 3) inclusion of mass accretion by accounting for mass conservation, and 4) including phase transformation. Enrichments 1 and 4 allow for temperature-dependent materials to be included in the NEASM while enrichments 2 and 3 account for realistic part geometries and effects of multiple layers, respectively. In general, the NEASM is capable of predicting the thermal history of full AM part builds including rastering within a layer and the effects of multiple layers. However, for this work, only single-track data is needed thus it can be assumed that boundary effects are negligible (*i.e.*, the laser is sufficiently far from all boundaries and enrichment 2 is not necessary).[113] Additionally, under certain circumstances, the NEASM can produce results with accuracy comparable to finite element modeling.[89] Each simulation in this work using the NEASM takes under 1 minute.

### 2.2.3 Finite Element Modeling

The finite element analysis (FEA) parametric simulation was implemented in COMSOL Multiphysics ® 5.6 [114] in conjunction with the LiveLink™ capability enabling direct communication between COMSOL and MATLAB®[115]. The MATLAB scripting capability offers the opportunity to automate the generation of the datasets required to construct the surrogate models. The developed simulation capability is based on an advective Eulerian approach that significantly reduces the computational cost as compared to a traditional Lagrangian approach. The solved equation expresses the local balance of energy and reduces to the advective heat conduction equation in the form:

$$\rho\left(T\right) C_p\left(T\right) \mathbf{u} \cdot \nabla T - \nabla \cdot \mathbf{q} = 0, \tag{2.1}$$

with $T$ the temperature, $\mathbf{q} = -k\left(T\right) \nabla T$, the heat flux vector defined by the Fourier constitutive equation, $\rho\left(T\right)$ the temperature dependent density, $C_p\left(T\right)$ the temperature dependent heat capacity, $k\left(T\right)$ the temperature dependent thermal conductivity, $\mathbf{u} = \left\{-v\mathbf{i}, 0\mathbf{j}, 0\mathbf{k}\right\}^T$ the velocity vector, and $v$ the velocity magnitude of the deposited beam power source in the x-direction.

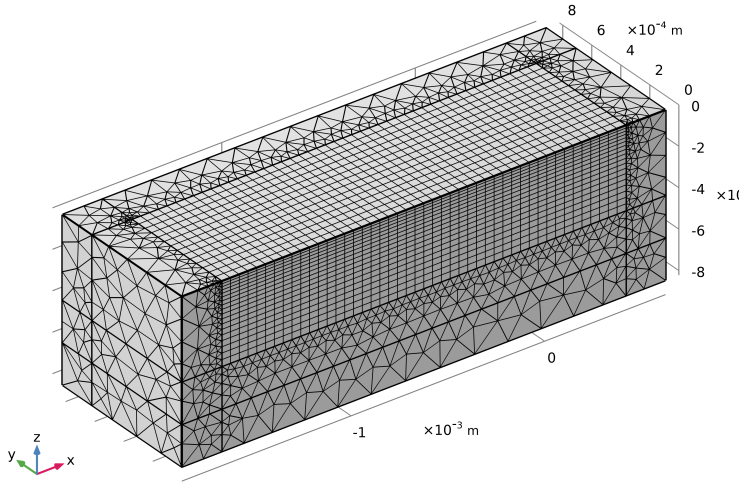


Figure 2.1: One realization of the parameterized, discretized domain used in the COMSOL heat transfer simulations.

One realization of the discretized domain is shown in figure 2.1. The $xz$ plane at $y = 0$ is considered a symmetry plane by enforcing $-\mathbf{n}\cdot\mathbf{q} = 0$, with $\mathbf{n}$ the normal vector of the surface. The domain is discretized with tetrahedral elements utilized the feature of COMSOL Multiphysics® for enabling semi-infinite domains with the intent to simulate an arbitrarily large geometry with a finite domain. A convective heat flux boundary condition was applied using $-\mathbf{n}\cdot\mathbf{q} = h(T_\infty - T)$ to simulate the presence of material at the outside of these domains. $T_\infty$ was taken as the room temperature. The value of $h$ was identified after trial and error in a manner that simulates the convection as 316L material was the medium on the other side of the wall. The approximate value identified was $h = 500\mathrm{W}/(\mathrm{m}^2\mathrm{K})$. It should be noted that the results of the simulation are very insensitive to the actual value of $h$ since the infinite element domain already addresses simulating boundary conditions at very large distances. The deposited beam power was applied at the top boundary of the hexahedral elements in the form of a heat flux boundary condition given by:

$$-\mathbf{n}\cdot\mathbf{q} = \alpha P_0 f\left(\mathbf{O}, \mathbf{e}\right) \frac{|\mathbf{e}\cdot\mathbf{n}|}{\|\mathbf{e}\|}, \tag{2.2}$$

with $a = 0.45$ the laser coupling coefficient, $P_0$ the laser power and $\mathbf{e} = \{0\mathbf{i}, 0\mathbf{j}, -1\mathbf{k}\}^T$ the beam orientation vector. The function $f$ defines the deposited beam shape and was assumed to be of a Gaussian form according to:

$$f(\mathbf{O}, \mathbf{e}) = \frac{1}{2\pi\sigma^2} e^{-\frac{s^2}{2\sigma^2}}, \tag{2.3}$$

with

$$s = \frac{\|\mathbf{e} \times (\mathbf{x} - \mathbf{O})\|}{\|\mathbf{e}\|}, \tag{2.4}$$

where $x$ is the vector of coordinates of each boundary point and $\mathbf{O}$ is the center of the beam application, considered here to be at point $\{0, 0, 0\}^T$. The Gaussian distribution variance was assumed to be equal to $d/4$ with $d$ the apparent beam diameter (*i.e.*, D4$\sigma$ as defined previously).

One challenge with developing the automated dataset generation relates to the very wide extent of the parametric values, which entails different geometry sizes for different values of the parameters because of the different spread in temperature distribution. Since it is impossible to know *a priori* the extent of the melt pool, an iterative algorithm was developed to detect when the geometry needed to be adjusted to account for the size of the melt pool. The algorithm performs the simulation using nominal values, and if it identifies that the width or length of the melt pool is very close to the boundaries, it extends the length of the domain and executes another simulation. The process is repeated until the computational domain is at least twice as big as the extent of the melt pool in all three directions.

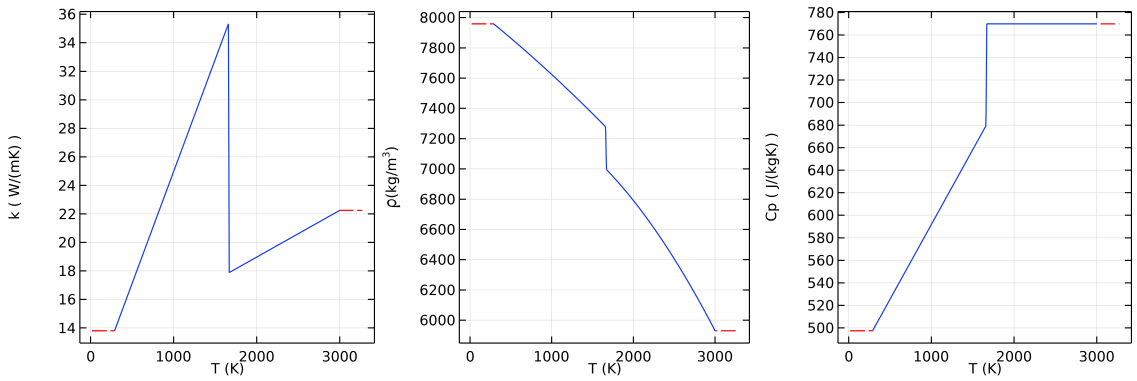


(a) Conductivity (b) Density (c) Heat Capacity

Figure 2.2: The temperature dependent material properties assumed for the heat transfer problem.

The simulations were performed using the temperature dependent material properties shown in figure 2.2. The extent of the melt pool in the three directions representing width, length, and depth, were calculated by finding the extrema of the temperature iso-surfaces for $T = T_{melt} = 1660\text{K}$. Three simulations showing temperature distributions and domain size changes with parameters are shown in figure 2.3. The computational time for each of the simulations on a 4-core laptop was at the level of 20-25s.

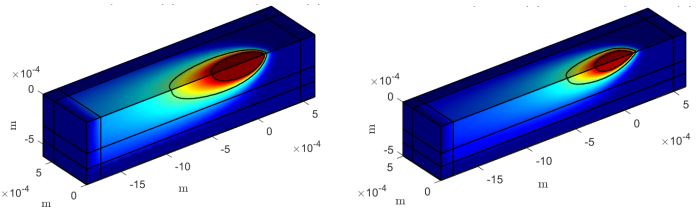

(a) $v = 105\text{mm/s}$, $P_0 = 396\text{W}$, $d = 92\mu\text{m}$ (b) $v = 150\text{mm/s}$, $P_0 = 257\text{W}$, $d = 252\mu\text{m}$

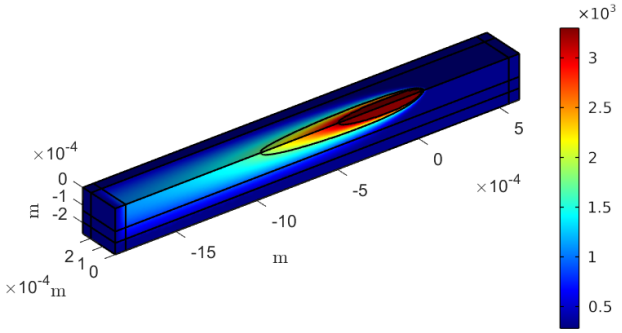

(c) $v = 956\text{mm/s}$, $P_0 = 398\text{W}$, $d = 58\mu\text{m}$

Figure 2.3: Example temperature distributions for three different parameter combinations.

### 2.2.4 Experimental Data

Experiment data used for training and testing the MFGP scheme are single-track experiments conducted on a GE/Concept Laser M2 selective laser melting (SLM) system on a 316L stainless steel plate.[116] The single-tracks were processed directly on the 316L plate. The nominal processing conditions for the system are 900 $\text{mm/s}$ laser velocity, 370 $\text{W}$ laser power, and 160 $\mu\text{m}$ laser spot size. The minimum and maximum ranges of the system are 10-7000 $\text{mm/s}$, 75-400 $\text{W}$, and 50-350 $\mu\text{m}$. These ranges are used to bound the data generation in the experiments as well as the other models with the exception that a maximum laser velocity of 2000 $\text{mm/s}$ is set. This velocity was chosen as a practical maximum given the maximum possible power of the system (*i.e.*, without an increase in power, such high velocities will seldom result in melted material).

Melt pool width and depth were extracted from the single-track experiments using optical microscopy. The samples were mounted and subjected to standard stainless steel grinding and polishing procedures (*i.e.*, 320 grip paper, 9 $\mu\text{m}$ diamond polishing, 3 $\mu\text{m}$ diamond polishing, then

4 nm OP-S polishing). 10% oxalic acid electroetching at 5V for 15s was used to reveal the melt pool. Once mounted and processed, optical microscopy was performed. Melt pool width and depth were extracted from the optical images. A representative output image from this process is shown in figure 2.4a In addition to melt pool width and depth, the melt pools were visually evaluated to determine if the run was in keyholing or conduction mode (figure 2.4b), whether beading (figure 2.4c), or if there was lack of fusion. Note that melt pool depth was measured from the surface in all cases for consistency.


(a) Measurements of melt pool width and depth.

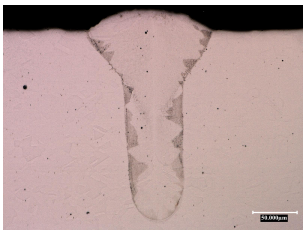

(b) Melt pool image demonstrating keyholing

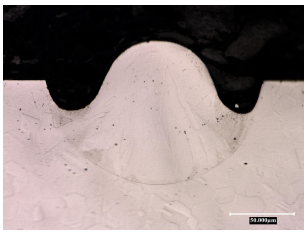

(c) Melt pool image demonstrating beading

Figure 2.4: Representative single-track experiment SEM images.

## 2.3 Multi-fidelity Gaussian Processes

The KOH model [107] has been demonstrated to be very effective at multi-fidelity information fusion over the past two decades. However, it has two primary limitations. First, there is a

linear correlation assumed between the higher fidelity data and the next lowest fidelity data. This linear correlation assumption is generally adequate but, in many computer models, this linear correlation only holds for specific ranges of the model. For instance, the ET model of this work always assumes conduction is the dominant heat transfer mechanism. When this is true, the ET model will likely be linearly correlated to higher fidelity models. However, at process parameters where conduction is not the primary mechanism, other models accounting for multiple heat transfer mechanisms could give a significantly different prediction that is not linearly correlated to the ET solution. The second limitation of the KOH model is that the computational complexity to train the model scales as $\mathcal{O}((\sum_{t=1}^{s} n_t)^3)$ where $s$ is the number of fidelities and $n_t$ is the number of data points at each fidelity. This computational complexity can quickly become intractable considering that the lowest fidelity models can easily generate hundreds or thousands of points. However, both of the stated limitations have been overcome in recent years with Le Gratiet *et al.* [117, 118] addressing the latter and Perdikaris *et al.* [119] addressing the former. In the following derivations, standard GP regression and classification theory is briefly mentioned but for complete details, the interested reader is directed to the book of Rasmussen and Williams [120].

First, assume that there is a dataset $\mathcal{D} = \{\boldsymbol{x}_i, y_i\} = (\boldsymbol{x}, y)$ for $i = 1, \ldots, n$ with input vectors $\boldsymbol{x}_i$ and responses $y_i$ for $n$ points. These data are assumed to be generated by some unknown latent function $f(\cdot)$ which follows an $n$-dimensional multivariate Gaussian distribution such that,

$$p(f(\boldsymbol{x}_1), \ldots, f(\boldsymbol{x}_n)) \sim \mathcal{N}_n(\boldsymbol{\mu}, \boldsymbol{k}), \tag{2.5}$$

where $\boldsymbol{\mu}$ is the mean vector defined by the mean function $\mu(\boldsymbol{x}_i) = \boldsymbol{\mu}_i = \mathbb{E}[f(\boldsymbol{x}_i)]$ and $\boldsymbol{k}$ is the covariance defined by the covariance function $k(\boldsymbol{x}_i, \boldsymbol{x}_j) = \boldsymbol{k}_{ij} = cov[f(\boldsymbol{x}_i), f(\boldsymbol{x}_j)]$. Now, the unknown latent function can be assigned a Gaussian process prior denoted as $f(\cdot) \sim \mathcal{GP}(\mu(\cdot), k(\cdot, \cdot))$. As is common, throughout this work it will be assumed that this and all other GP priors are zero mean (*i.e.*, $\mu(\cdot) = 0$).

In the context of multi-fidelity modeling, there are now multiple datasets from each fidelity

such that $\mathcal{D}_t = (\boldsymbol{x}_t, y_t)$ for $t = 1, \ldots, s$ with the $s$-level being the highest fidelity and the first level being the lowest. In the KOH auto-regressive model, the $s$ level are correlated as

$$f_t(\boldsymbol{x}) = \rho f_{t-1}(\boldsymbol{x}) + \delta_t(\boldsymbol{x}), \tag{2.6}$$

where $\rho$ is a scaling factor that linearly correlates the $t$ and $t-1$ fidelities and the bias of the lower fidelity is captured by $\delta_t(\boldsymbol{x}) \sim \mathcal{GP}(0, k_t(\cdot,\cdot))$. As mentioned above, the construction of the model in this way has a cost of $\mathcal{O}((\sum_{t=1}^{s} n_t)^3)$ due to the required inversion of the covariance matrix to compute the posterior. Le Gratiet *et al.* derived a more numerically efficient scheme by replacing the GP prior $f_{t-1}(\boldsymbol{x})$ with the corresponding posterior $f^*_{t-1}(\boldsymbol{x})$ while maintaining $\mathcal{D}_t \subseteq \mathcal{D}_{t-1}$. Since nested data ((*i.e.*, data from fidelity $t$ is a subset of the points in fidelity $t-1$)) have been assumed, the posterior predictive density $f^*_{t-1}(\boldsymbol{x})$ is deterministic at $\boldsymbol{x}$, which essentially decouples the MFGP problem into $s$ standard GP problems. It was shown that this scheme results in the exact same posterior as the KOH model, while being more efficient (computational cost of $\mathcal{O}(\sum_{t=1}^{s} (n_t^3))$) and yielding predictive models for each fidelity rather than only the highest fidelity as is the case in the KOH model.

To account for non-linear correlations, Perdikaris *et al.* modified equation 2.6 as

$$f_t(\boldsymbol{x}) = z_{t-1}(f_{t-1}(\boldsymbol{x})) + \delta_t(\boldsymbol{x}), \tag{2.7}$$

where $z_{t-1}(\cdot)$ is an unknown function that maps the lower fidelity to the higher fidelity. This unknown function is assigned a GP prior such that $z_{t-1}(\boldsymbol{x}) \sim \mathcal{GP}(0, k_t(\cdot,\cdot))$. By assigning a GP prior to $z_{t-1}(\cdot)$, the posterior of $f_t(\cdot)$ is no longer Gaussian and is considered a "deep GP". These deep GPs are generally very computationally complex, but can be made more tractable by following the scheme of Le Gratiet *et al.* where the prior of fidelity $t-1$ is replaced by the posterior as

$$f_t(\boldsymbol{x}) = z_{t-1}(f^*_{t-1}(\boldsymbol{x})) + \delta_t(\boldsymbol{x}) = g_t(\boldsymbol{x}, f^*_{t-1}(\boldsymbol{x})), \tag{2.8}$$

where $g_t(\boldsymbol{x}) \sim \mathcal{GP}(0, k_t((\boldsymbol{x}, f^*_{t-1}(\boldsymbol{x})), (\boldsymbol{x'}, f^*_{t-1}(\boldsymbol{x'}))))$. This formulation is made possible by the independence of $z_{t-1}(f^*_{t-1}(\boldsymbol{x}))$ and $\delta_t(\boldsymbol{x})$ as well as the fact that the sum of two GPs results in another GP. Perdikaris *et al.* note that this formulation retains the equivalent Markov property of the KOH model and the scheme of Le Gratiet *et al.*. Furthermore, with certain covariance kernel choices, the formulation of Le Gratiet *et al.* can be obtained. In this work, the covariance function of $g_t$ takes the decomposed form of

$$k_{t_g} = k_{t_\rho}(\boldsymbol{x}, \boldsymbol{x'}) \cdot k_{t_f}(f^*_{t-1}(\boldsymbol{x}), f^*_{t-1}(\boldsymbol{x'})) + k_{t_\delta}(\boldsymbol{x}, \boldsymbol{x'}), \tag{2.9}$$

where each $k_t$ is a valid covariance function. The covariance functions will take the common form of a stationary, squared exponential covariance as

$$k_t(\boldsymbol{x}, \boldsymbol{x'}) = \eta_t \exp\left(-\frac{1}{2}\sum_{k=1}^{p} \theta_{k,t}(x_k - x'_k)^2\right). \tag{2.10}$$

When $k_{t_\delta}(\boldsymbol{x}, \boldsymbol{x'})$ takes the form as specified, it will result in a nonlinear correlation, but in portions of this work, a linear correlation will be used for comparison and that will results in $k_{t_\delta}(\boldsymbol{x}, \boldsymbol{x'})$ taking the form of a bias or constant kernel. The parameters $\{\eta_t, \theta_{1,t}, \ldots, \theta_{p,t}\}$ for $t = 1, \ldots, s$ make up the set of so-called hyper-parameters, which allow "tuning" of the correlation between data points and fidelities, and are learned from the data at each fidelity along with the posterior of the previous fidelity.

Note that up this point, no differentiation has been made between regression and classification. In both settings, the unknown latent function has the form as given and the posterior distribution can be found as

$$p(f^*_t(\boldsymbol{x}^*)) = \int p(f_t(\boldsymbol{x}^*, f^*_{t-1}(\boldsymbol{x}^*))|y_t, \boldsymbol{x}_t, \boldsymbol{x}^*) p(f^*_{t-1}(\boldsymbol{x}^*)) d\boldsymbol{x}^*. \tag{2.11}$$

In the standard GP regression problem and the non-linear auto-regressive GP (NARGP) regression with $t = 2$, the likelihood is Gaussian and along with the assumed Gaussian priors, the poste-

rior predictive distribution is Gaussian and the integral can be computed analytically. However, NARGP regression with $t > 2$ and in all GP classification, the posterior is not Gaussian and alternative methods must be used to compute the integral to obtain the posterior predictive distribution.

### 2.3.1 Regression

Even though the posterior for the NARGP with more than two levels is not Gaussian, the process to compute it is still quite simple. First, each level of the model is trained individually. At the first level, this corresponds to a standard GP regression with $\mathcal{D}_1 = (\boldsymbol{x}_1, y_1)$. Subsequent levels require modifying the training dataset such that $\mathcal{D}_t = ((\boldsymbol{x}_t, f^*_{t-1}(\boldsymbol{x}_t)), y_t)$. Acquiring the posterior $f^*_{t-1}(\boldsymbol{x}_t)$ does not require approximating the integral of the previous fidelity, because the posterior of fidelity $t-1$ is deterministic at all points $\boldsymbol{x}_t$ due to the assumed nested structure of the data. This training process is repeated for all fidelities until the $s$-levels are trained. Once trained, the posterior predictive density at a new point $\boldsymbol{x}^*$ can be found at all fidelities $t > 2$ by using Monte Carlo (MC) integration of equation 2.11. For fidelity $1$ and $2$, the posterior can be analytically obtained since it is Gaussian. Note that using MC integration requires the propagation of all samples from the previous fidelity to the current fidelity while sampling at the current fidelity. In doing so, the number of samples required to approximate the posterior scales exponentially and at the highest fidelity requires $(n_{MC})^s$ total samples.

### 2.3.2 Classification

Unlike GP regression, GP classification always requires approximation methods to evaluate the posterior. In GP classification, the latent function is considered a nuisance function where its value is never observed and, once a value is determined, it is transformed through a nonlinear warping to make predictions of observations. For the case of binary classification, which this work will focus on, this results in $\pi(\boldsymbol{x}) \triangleq p(y = 1|\boldsymbol{x}) = \Phi(f(\boldsymbol{x}))$, where $\pi(\cdot)$ is a deterministic function and, in this work, $\Phi(\cdot)$ is the standard Normal cumulative distribution function (*i.e.*, a probit function is used for the warping). The probit function has the purpose of warping the latent function from $[-\infty, \infty]$ to $[0, 1]$, which is then used as a prediction of the class probability.

Since this work focuses only on binary classification, the data likelihood will take the form of a Bernoulli distribution.[121] For the case of a single fidelity classifier, methods to approximate the posterior have been well studied and the approximation can be done via Laplace approximation or expectation propagation (EP) [120] or MC methods such as Markov chain Monte Carlo (MCMC). However, multi-fidelity GP classification has not been as well studied. Recently, Sahli Costabal *et al.* [122] developed and demonstrated a multi-fidelity GP classifier that was based on the KOH model and used MCMC to approximate the posterior. Likewise, Klyuchnikov and Burnaev [123] presented a Laplace approximation method for Gaussian process classification with two fidelities. However, this again was based on the KOH model using a linear correlation structure.

In this work, a novel approach to MFGP classification is taken. In general, all equations derived up to this point still hold. However, each dataset $\mathcal{D}_t = (\boldsymbol{x}_t, y_t)$ now has labels $y_t$ take the form of binary classes $0$ or $1$, rather than continuous variables. This allows the predictive posterior for the data to be written as

$$\pi_t^*(\boldsymbol{x}^*) \triangleq p(y^* = 1 | y_t, \boldsymbol{x}_t, \boldsymbol{x}^*) = \int \Phi(f_t^*(\boldsymbol{x}^*)) p(f_t^*(\boldsymbol{x}^*)) d\boldsymbol{x}^*. \tag{2.12}$$

One can note that this posterior is the same as the posterior given in Rasmussen and Williams [120], except generalized to multiple fidelities and including a dependence (via equation 2.11) on the previous fidelity posterior prediction. By maintaining the assumptions given above, the problem of MFGP classification is reduced to fitting $s$ single fidelity classifiers as developed by Le Gratiet *et al.* [117, 118] and allows the nonlinear correlation structure developed by Perdikaris *et al.* [119] to be maintained (*i.e.*, this approach is nearly identical to the NARGP regression above). The primary differences between the NARGP regression and classification are in training. First, to train each fidelity classifier, one must implement an approximation method as discussed above. In this work, that approximation is made using EP. Using an approximate inference method like EP is useful here as it allows the computational efficiency to be maintained. If implementing an MC type approach, sampling $s$ fidelities can quickly become cumbersome and costly. From here, the approach to

training is exactly as it is in the case of regression where each fidelity is trained recursively and the posterior of the latent function is used as an input to the next fidelity. It is important to emphasize here that, while the latent function in classification is unobserved, it does provide information about the underlying relationship between the data. If posterior predictive distribution for the data is used here as the input the the next fidelity, the warping function will tend to map points that could be very far apart so that they appear close together and related. Once the models are trained, MC integration is performed exactly as is done in the regression case except posteriors for both the latent function and the data are needed. The latent function posterior samples are propagated to the next fidelity, while the posterior of the data is the prediction of the GPC for the current fidelity.

### 2.4 Data Generation & Model Training

In order to generate data to train the MFGP regression and classification, each of the four information sources detailed above must be sampled. The laser power ($P$), velocity ($V$), and spot size ($S$) are varied while the melt pool length ($L$), width ($W$), depth ($D$), conduction/keyhole mode class ($K$), beading class ($B$), and lack of fusion class ($F$) are output. The ranges for the input parameters are based on the experimental setup and are detailed above in section 2.2.4. Due to experimental limitation, melt pool length is not measured and is only available for simulations (*i.e.*, the 3 lowest fidelities). Conversely, the simulations do not contain sufficient physics to produce conduction/keyhole mode classifications. In lieu of direct class outputs for the simulations, empirical measures based on melt pool dimensions will be used to generate the needed output.[73] In this work, keyholing will correspond to a melt pool width to depth ratio of $W/D < 1.5$. Additionally, lack of fusion and beading classification will be predicted as $L/W > 2.3$ and $D/t < 1$, respectively, where $t$ is the powder layer thickness, which will be 25 $\mu$m. The set of these 3 classes will determine the so-called “printability" and give a predicted process parameter space where “good" (*i.e.*, defect free) printing should occur. The framework for MFGP regression and classification is shown in figure 2.5.

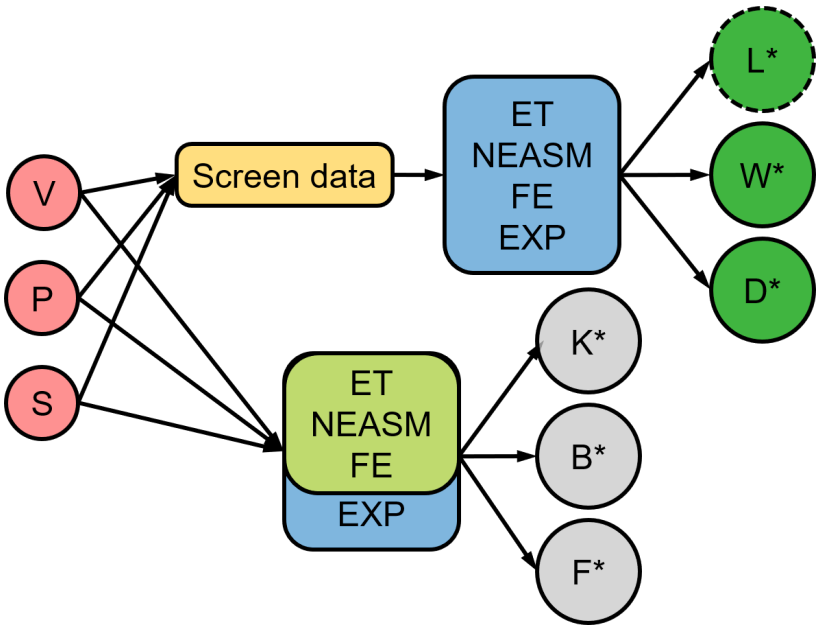


Figure 2.5: MFGP regression and classification framework. Process parameter inputs are shown at the left, these are fed into the NARGP regression (possibly after some data screening, discussed later) and classification, which are used to create predictions of melt pool dimensions and printability. For regression, melt pool length is only trained for NARGP models without EXP. For classification, empirical classes are used for all simulation data.

In the case of a single fidelity data source, data is typically generated via a space-filling design of experiments (DoE) method such as Latin hypercube sampling (LHS). However, simply sampling each of the thermal models used here from the different fidelities would result in multiple space filling designs that would almost certainly not be nested, thus violating the assumptions of the theory above. With multi-fidelity modeling becoming more common in the past decade, numerous space filling nested DoE (nDoE) methods have been developed.[124, 125, 117, 118, 126, 127] In this work, the relatively simple scheme of Le Gratiet *et al.* [117, 118] is chosen. In this nDoE method, a space filling LHS design of $n_s$ points is first created for the highest fidelity model. Subsequently, another LHS design is constructed for fidelity $s-1$ with $n_{s-1}$ points. From the $n_{s-1}$ points, the points that are closest in space to the higher fidelity $n_s$ points are removed and replaced by the points $n_s$. In this work, a simple Euclidean distance measure is used but any desired distance measure could equivalently be implemented. The process as described is recursively applied until

LHS designs are generated and modified for all $s$-fidelities. For this work, the ET model is sampled 500 times, the NEASM sampled 200 times, FE sampled 100 times, and experiments (henceforth referred to as EXP) sampled 50 times. For training, all data are used except 15 experiments, which were randomly selected from the 50 available. The 15 experiments not used for training are used for validation/testing of the trained GPs.

The NARGP regression and classification as well as the nDoE are all implemented in Python 3. The NARGP regression and classification are based on Emukit (`https://emukit.github.io/`) [128], although the implementation has been modified to perform classification and cross-validation (although not used for this work) in the regression setting.

### 2.5 Results & Discussion

In this work, the NARGP will be trained on all combinations of fidelities with 2 or more fidelities included. In addition to this, each of the combinations will be trained once with a nonlinear correlation between fidelities and a second time assuming a linear correlation between fidelities. This will result in 22 trained NARGP models (Table 2.1), which will be compared to standard GPs trained on a single fidelity. Each of the trained models will first be compared to the experiment test set and discussed, following this, a comparison of which fidelities included in the NARGP result in the best models for the least computational cost will be discussed.

Table 2.1: Multi-fidelity model combinations with corresponding labels of 1-22. Each design uses a binary labeling where a 1 indicates inclusion in the model and 0 exclusion. The nonlinear column specifies if a nonlinear correlation was used (1) or was not used (0)

| | **Nonlinear** | **EXP** | **FE** | **NEASM** | **ET** |
|---|---|---|---|---|---|
| 1 | 1 | 1 | 1 | 1 | 1 |
| 2 | 0 | 1 | 1 | 1 | 1 |
| 3 | 1 | 0 | 1 | 1 | 1 |
| 4 | 0 | 0 | 1 | 1 | 1 |
| 5 | 1 | 1 | 0 | 1 | 1 |
| 6 | 0 | 1 | 0 | 1 | 1 |
| 7 | 1 | 0 | 0 | 1 | 1 |
| 8 | 0 | 0 | 0 | 1 | 1 |
| 9 | 1 | 1 | 1 | 0 | 1 |
| 10 | 0 | 1 | 1 | 0 | 1 |
| 11 | 1 | 0 | 1 | 0 | 1 |
| 12 | 0 | 0 | 1 | 0 | 1 |
| 13 | 1 | 1 | 0 | 0 | 1 |
| 14 | 0 | 1 | 0 | 0 | 1 |
| 15 | 1 | 1 | 1 | 1 | 0 |
| 16 | 0 | 1 | 1 | 1 | 0 |
| 17 | 1 | 0 | 1 | 1 | 0 |
| 18 | 0 | 0 | 1 | 1 | 0 |
| 19 | 1 | 1 | 0 | 1 | 0 |
| 20 | 0 | 1 | 0 | 1 | 0 |
| 21 | 1 | 1 | 1 | 0 | 0 |
| 22 | 0 | 1 | 1 | 0 | 0 |

### 2.5.1 Experiment Validation

#### *2.5.1.1 Regression*

Since a classification is being trained to screen for defect inducing parameters and the purpose of the regression model is to predict good melt pool dimensions that can be propagated to subsequent models, the regression model can be trained in one of two ways. First, utilizing all data including data which produces melt pools that exhibit keyholing, beading, and/or lack of fusion. Or second, screen the training data beforehand and only training the regression model on the most relevant good print data. In the former case, more data will be available to train the model, but the data may be unnecessary since some regions will never be queried for predictions and won't necessarily reduce the uncertainty in relevant good regions. For the sake of comparison, models are trained using both data sets in this work. In both instances, a GP will also be trained on the highest fidelity model used in the NARGP. Melt pool length is not included here as melt pool length measurements were not able to be collected in the experiments. Mean absolute percent error (MAPE) is used to evaluate the error of the trained model on the test data. The results of training can be seen in figures 2.6a and 2.6b for the models trained on all data and models trained on only good print data, respectively. Note, that in all cases, only test data that does not produce a defect will be used to evaluate the model. Since the regression model will only be used to predict good prints, these filtered test data will be the most relevant to evaluate true model accuracy. The filtered data set has 7 test points remaining of the original 15.

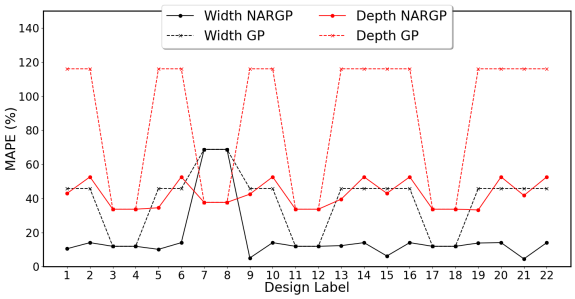


(a) MAPE when all training data is included.

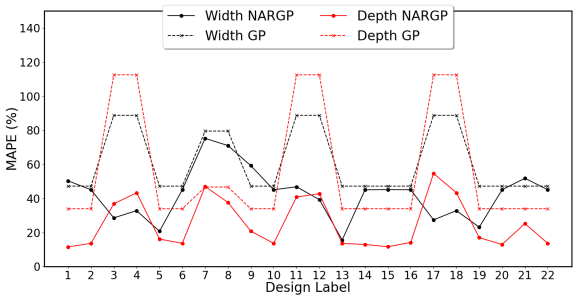


(b) MAPE when only good data is included.

Figure 2.6: MAPE evaluated on test set melt pool width (W) and depth (D) data for the NARGPs of Table 2.1 and GPs.

From figure 2.6a, it can be seen that the GP can achieve a minimum error of 11.9% for the melt pool width and 33.7% for the depth when it is trained using the FE data. In general, the NARGP achieves a substantial improvement in accuracy over just the GP and in the worst cases, achieves a similar level of accuracy. In the best case scenario the NARGP can predict the melt pool width with 4.5% error and the depth with 33.7% error. For the melt pool width, the best model combinations were the EXP and FE with a nonlinear correlation structure, while for the depth, the best was any model trained using FE without experiments.

For the GP only fitted to good data (figure 2.6b), a similar level of accuracy as the GP trained on all data is achieved. The GP achieves a minimum error of 47.2% for the melt pool width and 33.9% for the depth when it is trained using the EXP data. As before and as expected, the NARGP improves on or maintains the accuracy achieved by the GP alone with the best predicting the melt pool width with 15.6% error using EXP and ET and a nonlinear correlation and the melt pool depth with 11.5% error using all fidelities and a nonlinear correlation. Similarly, a melt pool depth error of 11.6% can be achieved with the same fidelities as the previous except excluding the ET data.

Regardless of the removal of data before training, the NARGP produces better results than a GP trained on a single fidelity. Furthermore, the NARGP demonstrates its value over traditional multi-fidelity GP modeling approaches as the nonlinear correlation between fidelities produces the models with the highest accuracy. As one might expect, the NARGP including experiments

produces the models with the lowest error. However, this is not the case for the GP where the model using FE data alone can produce a more accurate model than the one using experiments. This further highlights the need for multi-fidelity modeling to effectively increase the amount of information available for model training because, intuitively, experiments should always be used when available as they represent the ground truth. However, due to their high acquisition cost, only a limited number of experiments may be available and when taken alone may not produce the most accurate model as has been demonstrated.

Looking at the difference in the best cases when using all data versus only good data, it can be noted that the single best melt pool width prediction is obtained using all data, while the best melt pool depth prediction is obtained when using the screened good data. This can be attributed to how defects show up in the melt pool width and depth predictions. Melt pool width alone does not give a strong indication of a defect, unlike melt pool depth which can be a good indicator of keyholing and lack of fusion. Therefore, the melt pool width can be predicted more accurately when more data is available during training as is typically the case with GP-based models. For melt pool depth, the inclusion of data with defects and the fusion of information from models without the physics necessary to produce those defects tends to result in a model that is less accurate than a model trained on a consistent set of data (*i.e.*, one where simulations and experiments are both operating under the same physics). A similar trend on the difficulty of predicting melt pool depth can be seen in Tapia *et al.* [71].

In the best cases, an accuracy of around 5-10$\%$ could be achieved in prediction (slightly under for 5$\%$ for melt pool width and slightly over 10$\%$ for melt pool depth). Depending on the application this could be an acceptable level of error given the trade-off with computational time. Some recent works[70, 74, 76, 112] have demonstrated similar or slightly better accuracy on test data after training a GP model and using it to calibrate a physics-based model. Besides the obvious drawback of the increased computational time to query the model in comparison to the nearly negligible time to query a GP, this method has an additional drawback of a needing to use Bayesian method to perform the calibration. These Bayesian methods, while becoming more common, can

be costly and require some subject matter expertise to obtain convergence. The method implemented here uses a more naive approach. While each model has the same general material of 316L stainless steel, none of the models have been specifically calibrated to produce the same results. Thus, for a new material system, one could simply obtain data and/or model parameters from literature or utilize existing models to generate a new predictive model without the need to perform a new calibration.

There are a number of possible improvements that could be made to the NARGP to perform regression, such as the inclusion of simulation data from a multiphysics model, but one of the most notable improvements would be to change the NARGP from having multiple independent outputs to being a multivariate or multi-output model[70]. The process to convert the NARGP to a multivariate model would be relatively straightforward, though still beyond the scope of this work. Since the NARGP essentially only requires the iterative training of multiple GPs, rather a single multi-fidelity GP, the process to convert to a multivariate model would only entail converting each GP into a multivariate GP and training the NARGP as usual. Converting to a multivariate model could accomplish two objectives. First, it could potentially improve the regression model by leveraging information from both width and depth simultaneously while training. Secondly, by having a multivariate model, Bayesian methods could be used to impute the missing melt pool length data when it is unavailable. The imputation of the missing data would be possible without a multivariate model, but with a multivariate model, the coupling of the melt pool length, width, and depth at lower fidelities could greatly improve the imputation.

#### *2.5.1.2 Classification*

Unlike regression, classification will always be performed on all available data. For the sake of this work, classification will be conducted in a number of ways for comparison. First, it is performed as described by Section 2.3.2 for each of the three defect classes, where each class is binary 1 for defect and 0 if that defect is not present. A second approach is to group all the defects into a binary problem of defect (1) or no defect (0) if one or more of the defects is present. Finally, an approach similar to previous approaches[85, 73] where a trained regression model and

empirical measures, as detailed above, are used to predict if a defect will be present and what that defect will be. As the the beading metric requires melt pool length to approximate, any NARGP or GP that contains EXP will use the melt pool width and depth as normal but use melt pool length predictions based on the next lowest fidelity in the NARGP ((*e.g.*, an NARGP trained with EXP, FE, and NEASM will have melt pool length NARGP trained only on FE and NEASM and GP trained only on FE while EXP would be included in NARGP and GP for width and depth training)). To evaluate each of the classification models, a balanced accuracy score (BAS) is used. The BAS is a standard measure of classification accuracy except each class is weighted by the number of samples in that class. The BAS is used in this work since the number of defects in the test set for each defect type is relatively low (3 of each type over the 15 total points in the test set). Note that the BAS is 1 for a perfect classifier and is bounded between 0 and 1.

The classification results when predicting each defect individually are shown in figure 2.7. In the case of beading (figure 2.7a), a maximum BAS of 0.875 is achieved and is obtained using the regression-based NARGP and GP. The NARGP is only able to gain this level of accuracy using only the NEASM and ET models with a linear correlation. The GP on the other hand obtains this accuracy for a model trained on the NEASM. Interestingly, the NARGP and GP classifiers can only obtain approximately 0.8 BAS. This is obtained for a number of combinations but most notably, none of the combinations involve using experiments. For keyholing (figure 2.7b), a maximum BAS of 0.83 is obtained with the NARGP classifier as well as regression-based classifier. For the classifier, this BAS is achieved using EXP, FE, and ET runs with a linear correlation and for the regression, it is achieved with EXP and NEASM runs using a non-linear correlation. Interestingly, this maximum BAS regression case does not correspond to the regression results that best predict melt pool width and depth. In the case of lack of fusion (figure 2.7c), there a number of models that result in perfect predictions from all classifiers. The most notable result is with the NEASM and ET models combined or simply the NEASM, regardless of which method is used, can result in the highest BAS.

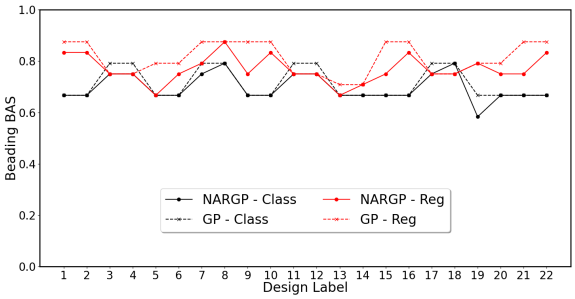


(a) Beading classification BAS.

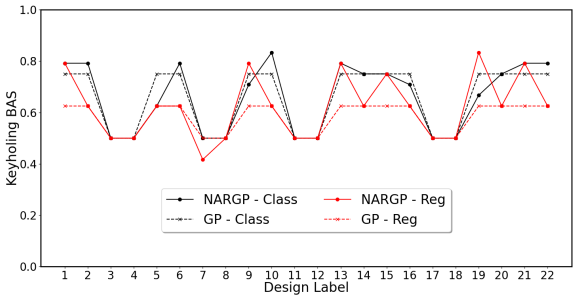


(b) Keyholing classification BAS.

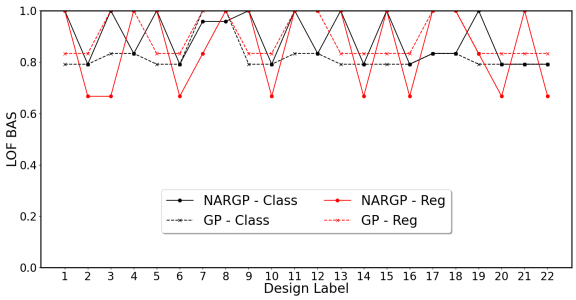


(c) Lack of fusion classification BAS.

Figure 2.7: Classification BAS for 3 defect types for the NARGP and GP classifiers and NARGP and GP regression-based classifiers.

Again, note that the previous classifiers were tested on a set of 15 points where only 3 points for each of the defects were present in the 15. This results in highly skewed classes and makes determining the true model accuracy harder. By combining all defects into a single class, the skew becomes much less noticeable as there are 7 defects of the 15 points. Combining the classes also reduces training time as only a single model needs to be trained for the classifier. For the regression-based classifier, 3 models are still trained since all melt pool dimensions are still needed to make classifications before being combined into a single class. The results of the binary defect classification are shown in figure 2.8. The results show a highest possible BAS of around 0.8 for the regression-based classifiers. These occur for GPs trained on experiment data and NARGP and GPs trained on NEASM and ET and NEASM, as was seen before.

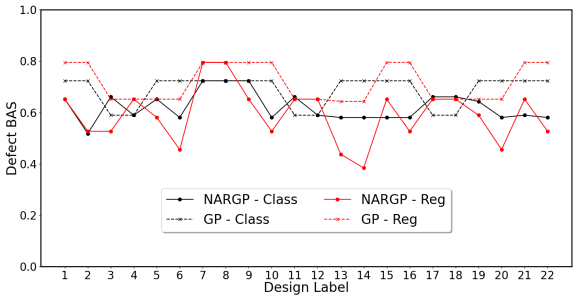


Figure 2.8: Grouped binary classifier BAS for NARGP and GP classifiers and NARGP and GP regression-based classifiers.

A few interesting points can be noted about both the combined and individual defect classifiers. First, it appears that in many cases, the regression-based classifier performs as well or better than the regular classifiers. Furthermore, the NARGP classifier does not appear to outperform a standard GP classifier in most cases. This is in contrast to the regression where the NARGP could greatly outperform the standard GP. One possible explanation for the lack of performance of the NARGP classifier is that the BAS is only indicating the mean performance of the classifier and not the full probability space. In testing of the NARGP on a pedagogical example, it was noted that the NARGP classifier produced fewer correct classifications but the overall probability map was closer to the true boundary used to generate the data. It is possible that this is again occurring here, however, without a concrete means to assess this, the BAS and similar metrics are the only option to evaluate a model. Comparing the two approaches to classification, grouped versus individual, there seems to be little impact on the BAS results. In the individual cases, the NARGP and GP classifiers both perform around 0.8, which is close to the highest level of achievable accuracy in the grouped cases. However, this conclusion is somewhat superfluous as the regression-based classifier appears to outperform the actual classifier and the regression approach only makes predictions without considering individual versus grouped during training. An interesting point that was mentioned earlier is that a GP classifier trained on the NEASM as the highest or only fidelity tends to produce the best or nearly the best results in all cases except individual keyholing predictions, where the experiments produce the best model likely because the experiments are the only fidelity with the

necessary physics to capture keyholing.

As with the regression there are some improvement that could be made to the classification. The most notable improvement would be to change to a multi-class classifier. This would nullify the need to decide between a binary defect/no-defect class or training individual classifiers. Much like the regression, changing to a multi-class classifier would be as simple as replacing the GP classifier implemented in this work with a new variant. The difficulty in changing to a multi-class classifier in the NARGP context is that the most common method to perform multi-class GP classification is via Bayesian methods, which become impractical when training multiple models sequentially. However, some recent works have begun to develop and implement non-Bayesian approaches to multi-class GP classification, which could be implemented in the NARGP framework.

### 2.5.2 Process Model Importance

In the previous section, each of the 22 trained NARGPs was examined and compared individually to the test set of experiments. Now, the NARGP results will be used to determine what fidelities included in the results tend to result in a better performing model. This is done by grouping the MAPE and BAS for each NARGP that includes each fidelity. This is further split by separating the linear versus nonlinear correlation models. Box plots of the data generated by this process are shown in figure 2.9 for the melt pool width and depth MAPE (for models with all data used for training and only good data used) and in figure 2.10 for the grouped BAS from the NARGP classifier and NARGP regression-based classification. For brevity, only the grouped classification results are examined.

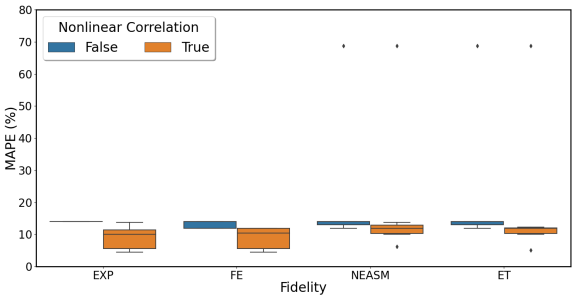


(a) Melt pool width with all data.

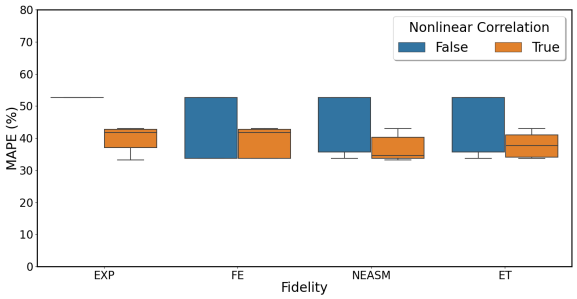


(b) Melt pool depth with all data.

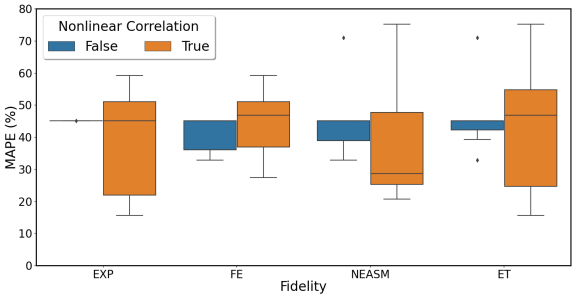


(c) Melt pool width with good data.

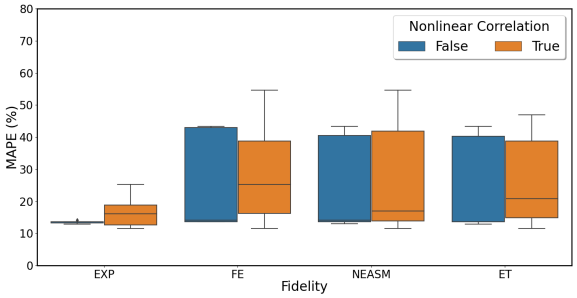


(d) Melt pool depth with good data.

Figure 2.9: Box plots showing MAPE ranges for NARGP models which included the given fidelity, both, with and without a nonlinear correlation.

In the case of the regression results for melt pool width, it can be noticed that a nonlinear correlation shows a wider spread of MAPE values, but tend to produce a better result in both cases of training with all data or only good data. In the case of the linear correlation, the melt pool width MAPE does not tend to change much as different fidelities are included in the NARGP. Whereas for the nonlinear correlation, the MAPE does tend to slightly decrease as higher fidelity data is added to the NARGP as one would expect. The results on melt pool width with all data versus good data also reinforce the conclusions above that a low MAPE can be achieved with a model trained on all data. With the exception of a couple outliers, the models trained on all data also show a lower variance than the models trained on good data only.

For melt pool depth, the conclusions from the previous section still hold, in that NARGP models trained on good data tend to produce lower error rates than a model trained on all data. Furthermore, the models trained using experiments result in the lowest MAPE values with the lowest vari-

ance. In the case of melt pool depth, the variance of linear correlation versus nonlinear correlation, as well as variance changes with fidelity, do not appear to change significantly until experiments are included. This, as stated, reduces the variance and tends to give the best results. Unlike melt pool width, the melt pool depth does not seem to improve significantly with higher fidelity data. The best model is any model multi-fidelity model that includes experiments. A similar conclusion can be made about melt pool width.

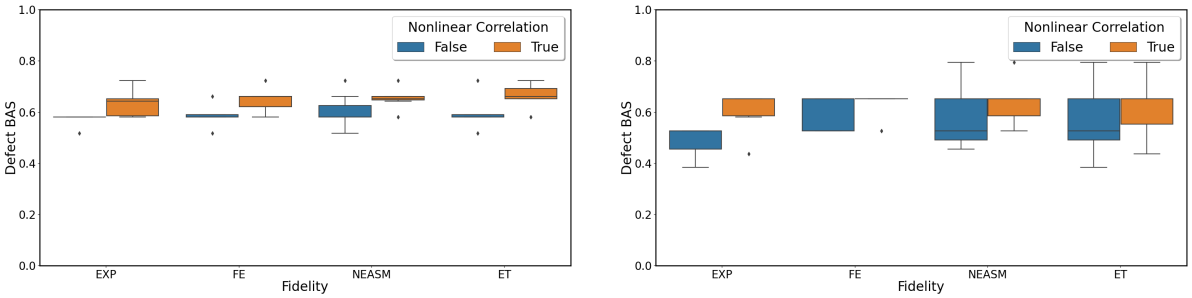


(a) NARGP classification.

(b) NARGP regression-based classification.

Figure 2.10: Grouped defect BAS box plots for fidelities included in the NARGP model for models with and without nonlinear correlations.

Unlike regression, the classification shows consistent BAS values regardless of NARGP fidelities or correlation used. In fact, there is a slight upward trend in the BAS for the NARGP classifier when lower fidelities are included. A similar trend can be noted for the regression-based classifier, although the trend is not as prevalent. The trends shown in the box plots offer additional insight into the previous conclusion about the regression-based classification outperforming the standard classification. The NARGP classification, as detailed in this work, does tend to perform as well or better then the regression-based version. However, the highest BAS obtained is with the regression-based models. The classification method presented in this work also shows a lower variance, which could be a desirable feature that makes selection of specific fidelity data sets less important.

#### *2.5.2.1 Model Selection*

Having several fidelities of data available to make the best model is obviously ideal, but training all combinations of models and generating data from so many sources is generally not practical. Here some best practices are discussed that result in generating data from the fewest fidelities that result in the best trained models. This is done for regression only models, classification only models, and then models for classification and regression.

For regression, two models will likely need to be trained regardless; one for melt pool width on all available data and another for melt pool depth where the data has been screened *a priori* to select only data which does not produce defects. While training two models is not ideal, the benefits could be worthwhile since a melt pool width prediction of $<5\%$ and depth prediction of $11\%$ is possible. Additionally, the NARGP is implemented with a maximum likelihood approach so training of a model is relatively fast. The drawback to achieve the level of accuracy shown is that at least 3 fidelities of data would be required, namely, EXP, FE, and NEASM. This could be a significant cost to acquire data from those sources and may not even be possible given that enriched analytical solutions are not widely available. Alternatively, a model using only EXP and ET data can be trained which results in a greatly reduced data acquisition cost with only a slight accuracy penalty, achieving $12.3\%$ width and $13.6\%$ error rates for the melt pool width and depth, respectively. While this level of error is somewhat high, it could serve as a good first order approximation and does not require specific calibration of the ET parameters using Bayesian methods.

In the case of classification, recommendations are much more difficult to make as clear trends are not seen as has been demonstrated in the previous sections. Using the NEASM model for any of the four classification methods shown (NARGP and GP classification and regression-based classification) appears to result in the best classifier for both individual and grouped classification except for keyholing predictions. Only models containing experiments are able to accurately predict keyholing to some extent. For the grouped classification, similar conclusions can be drawn. A GP regression-based classification with the NEASM or EXP provides the highest BAS around

0.8. Interestingly when combined in a multi-fidelity model, the result does not improve and tends to get slightly worse at 0.72 BAS.

Taking everything together, an NARGP model containing EXP, NEASM, and ET seems to be able to provide the best predictive model. The experiments improve keyholing and melt pool width and depth predictions, while the NEASM and ET have the purpose of predicting beading, lack of fusion, and/or grouped classification and add additional information to supplement the limited experiment data. While the resulting model would not be the best possible model, it would balance the data generation and model creation processes. Additionally, it would only require training a single NARGP regression model. While using the regression-based classification resulted in the best overall results, using the NARGP classification does have the potential to produce equivalent results to the regression-based version with less dependence on which fidelities are selected as was shown in the previous section.

## 2.6 Summary

This chapter has presented an analysis and discussion on predicting and classifying AM melt pools using multi-fidelity GP surrogates. The work examined four common sources of information at different fidelities, from analytical to experimental, and combined that information in a NARGP regression and novel classification models. The models were trained on a representative set of data and compared to a test set of experiments. All combination of fidelities were trained and compared to a standard GP. The NARGP regression demonstrated superior results over standard GP regression and require no model calibration (*i.e.*, Bayesian methods). Further, certain combinations of models, namely the experiments and Eager-Tsai model, were able to produce an accurate model which balanced data generation cost with attainable model accuracy. Depending on the fidelity of information available, a model was able to be produced, which matched or exceed the performance of existing GP modeling and calibration approaches. For classification, results using both grouped and ungrouped classes were examined along with regression-based classification using empirical measures and how that compared to using binary classification methods. The results showed that for ungrouped classification, experiments were necessary to accurately predict

keyholing, as one would expect, but using only the NEASM or a multi-fidelity model with the NEASM was sufficient to predict beading and lack of fusion. In the grouped classification setting, similar results were seen. In both cases, the regression-based classification was shown to produce a singular best model for classifying printability, but typical classification methods were able to produce more consistent results that were less dependent on the fidelities included in the model. While the NARGP classification approaches were able to produce some models that exceeded the performance of a standard GP, the results were not consistent. It was postulated that while the NARGP did not improve significantly on the classification accuracy for the available test set, it likely improved the predicted probability space.

# 3. AM PROCESS-STRUCTURE SURROGATE

## 3.1 Introduction

As was stated in chapter 1, there are a number of authors who have recently begun to analyze process-structure linkages for AM.[129, 7, 130] This linkage, is of great interest to the AM community, but much of the work to date has been on analyzing microstructures to extract information for ML, not necessarily linking the process to the structure for AM.[47, 131] Some of these methods use statistics to reconstruct microstructures from 2D sections.[132, 133, 134, 135, 136, 137] However, this has the obvious drawback of requiring information from experiments. More recently, spatial correlations have been used to reconstruct microstructures [138, 139, 140, 141, 142, 53] and these methods have been extended to incorporate ML methods.[143] In general, all of the reconstruction or feature extraction methods reference have been aimed at the case of general microstructure reconstruction. However, it must be recognized that AM microstructure are vastly different from typical microstructures and many of these methods may not be applicable. For instance, the use of the software DREAM.3D [135] to reconstruct a microstructure from a 2D section must make some assumptions about the 3D statistics based on the 2D statistics. In AM, the 3D information may not match the 2D (*i.e.*, a grain may have a certain appearance in a plane but have a vastly different shape in the transverse direction). Popova *et al.* [130] recently developed a PS linkage for AM microstructures generated by kinetic Monte Carlo (kMC) methods using an ML workflow and spatial correlation methods. But much work is still needed in this area, such as the inclusion of more physics-based models in the process-structure framework. The workflow presented in [130] is quite general and is implemented in this work albeit with a different methodology.

## 3.2 Microstructure Generation

There are a number of ways to approach modeling the microstructure formation phenomenon in AM.[144, 81, 145] The least physical approaches are purely statistical methods based on sim-

ulating the parameters of a tessellation model, with the drawback that these models are often too simplistic to capture the complex morphologies of AM microstructures.[146, 147] The next level of fidelity are statistical models, such as kMC methods, which simulate the time evolution of the grains growing in 3D and account for some idealized physics of the AM process.[148, 149] While these methods are capable of generating qualitatively good AM microstructures, they do not incorporate material texture or anisotropy and do not incorporate coupling of the thermal and microstructure models. The highest fidelity models incorporating the most realistic physical phenomena are phase field models that incorporate the kinetics of microstructure evolution into an energy functional to be minimized.[150, 151, 152, 153, 154] While this approach enables studying effects of competing mechanisms, it is too computationally demanding to simulate large numbers of polycrystalline microstructures for training an ML model. An alternative is to utilize the cellular automata FE (CAFE) model, which is a popular technique to simulate microstructure solidification because of its relationship between computational tractability and fidelity of physics.[155, 156]

In this work, a CAFE model that has been modified to optimally simulate the solidification of AM metals in large domains (on the order of 0.5-1 $cm^3$) is implemented for the generation of microstructures.[157] In this model, the small time scale of the solidification analysis is treated independently, as sub-cycles, within each larger scale discrete time step associated with the temperature field. Additionally, rather than growing the solidification front by using very small time steps in each sub-cycle, the time it takes for each solid voxel to capture its neighboring voxels is predicted and the simulation evolves sequentially based on priorities associated with the estimated time of capture. An additional modification to the CAFE model, which improves computational efficiency, is the determination and consideration of only the current active region(s) in the domain, which for AM is the region of the heat affected zone where the material is undercooled (*i.e.*, below liquidus temperature) but has yet to be solidified. The CAFE model is used to simulate the epitaxial grain growth from the base plate of the AM build by incorporating empirical models for analyzing competitive growth, such as preferential crystallographic growth or thermal gradient driven growth. An instantiation of the CAFE model consisting of 3 slightly overlapping tracks and

multiple layers is shown in figure 3.1.

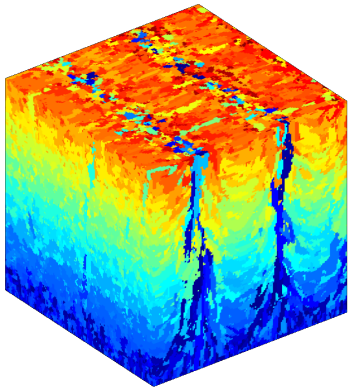

(a) Full 3D microstructure consisting of 3 tracks and multiple layers.

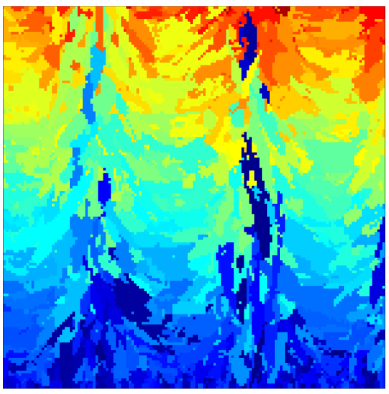

(b) A 2D cross-section of the same microstructure, which better demonstrates grains growing in the direction of the melt pools.

Figure 3.1: Polycrystalline microstructure generated using the modified CAFE model. Grain colors correspond to grain labels from 1 to $N$, where $N$ is the total number of grains.

### 3.3 Multi-output GP

As has been mentioned, a multi-output GP (MOGP) is implemented to emulate the CAFE model and link outputs from the process modeling surrogate to microstructure statistics needed for

the SP surrogate. A diagram of this linkage is shown in figure 3.2.

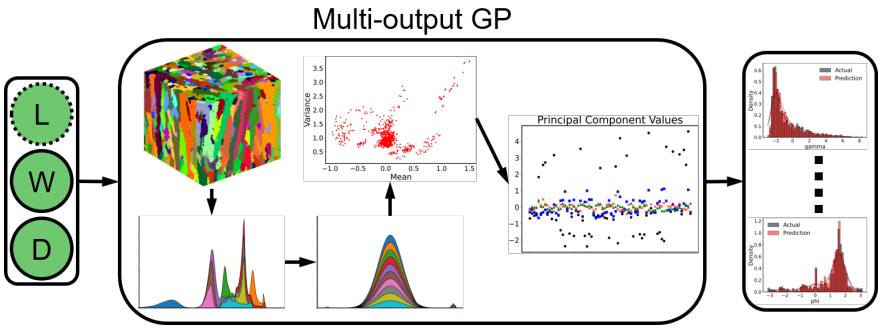


Figure 3.2: Diagram of the process-structure surrogate linking melt pool information, in this case dimensions of length (L), width (W), and depth (D), to microstructure statistics such as grain volumes and orientations.

In this work, each set of process parameters will generate a set of melt pool dimensions and each of those is subsequently used to generate a microstructure representative volume element (RVE). There are primarily two ways in which an RVE can be represented by an ML framework, as a 3D image or by dimensionality reduction. The former can be accomplished using unsupervised ML techniques and has begun to gain traction in the materials community with the advancement of generative adversarial networks (GANs).[158, 159, 160] However, these methods are quite new and as such emulating a 3D microstructure, especially one that exhibits the features seen in AM microstructures, is still an active research problem. The later method of dimensionality reduction is much more common, simpler, more interpretable, and implemented in this work following the workflow of figure 4 in [130].

First, in the data preprocessing stage, the output microstructures from the CAFE model are augmented by removing the base plate and disregarding simulations that did not result in complete melting. Next, in the microstructure quantification stage, the RVEs are processed to extract the 10 necessary parameter distributions for the SP surrogate. This process is accomplished by representing each grain in the RVE approximately as an ellipsoid then extracting volume, 3 radii, 3 orientation angles, and 3 size and shape dependent constitutive model parameters. The distributions from

all available microstructures are next merged into a unified data set where the dimensionality reduction stage begins. A quantile transformer is applied to each of the unified distributions to obtain 10 approximately normal distributions along with a reversible transformation process to achieve those normal distributions. This transformation is then applied to all available RVEs to extract 10 means and 10 variances from each RVE. This results in a set of scalar inputs that can be related to 20 scalar outputs. However, this is a large number of outputs and to make the problem more tractable, the outputs are reduced from 20 to 4 using principal component analysis (PCA), which captures approximately $99\%$ of the variance of the underlying data. The next stage in the process is the data-driven model estimation. In this stage, the MOGP is fitted to the training data. The training data consists of 74 CAFE model generated RVEs, each having a unique generating set of melt pool dimensions and corresponding process parameters. Each model consists of a base plate, which is trimmed off in the first stage, then a 4 printed layers each with 3 hatches. The hatch spacing is parameterized so that the tracks overlap based on the melt pool dimensions.[85] Each hatch is done in an alternating direction and the hatches on each layer are rotated $90^{\circ}$ from the previous layer. For the MOGP, either a coupled output [70] or independent output approach can be taken. In this work, an independent output model is used over the coupled (linear model of coregionalization [161]) output as during testing, it was noted that the coupled model only produced slightly better results on the first principal component (PC) but significantly worse results the other PCs. When considering a weighted error based on the explained variance of each PC, the independent model still outperformed the coupled model. Validation of the MOGP is accomplished by way of 10-fold cross-validation (CV) and a single left out test case. Since basic details of GPs has already been given in chapter 2 and the independent output model is essentially multiple standard GPs, further details are omitted.

### 3.4 Results

The CV results of the trained MOGP are shown in figure 3.3 with the explained variance ratio (EVR) of each PC shown. The CV results overall follow the 1:1 predicted:actual ratio that is ideal. The exception being the $3^{rd}$ PC which is shows a constant predicted value of approximately

0. This is likely a result of the inputs not adequately describing that PC. While this will affect the prediction accuracy, it should be a relatively minor effect since that PC only explains $1\%$ of the total variance.

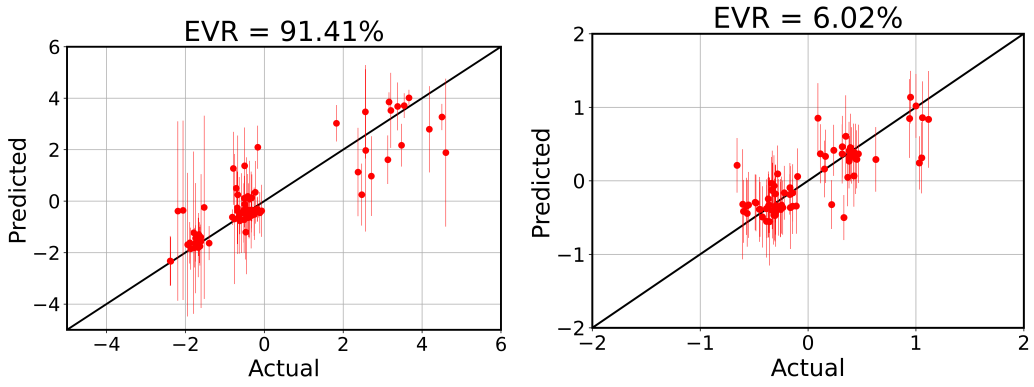


(a) $1^{st}$ PC. (b) $2^{nd}$ PC.

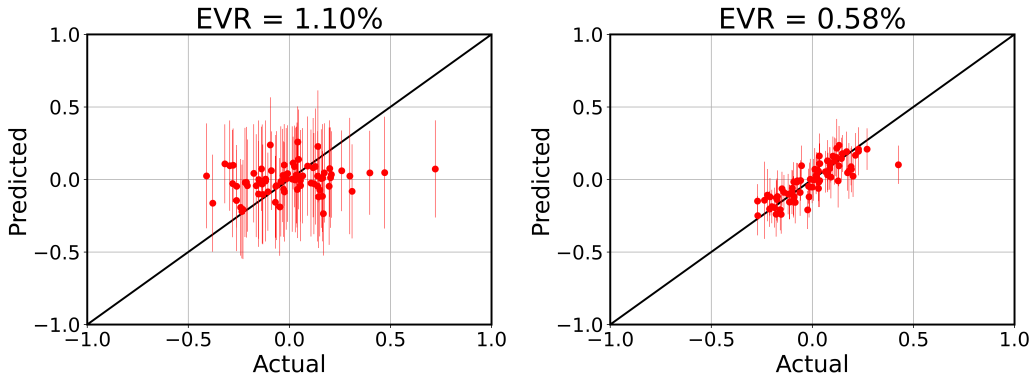


(c) $3^{rd}$ PC. (d) $4^{th}$ PC.

Figure 3.3: 10-fold CV parity plots for each PC of the MOGP surrogate. The explained variance ratio (EVR) is shown above each plot.

The predicted vs actual distributions of all 10 parameters for the left out test case are shown in figure 3.4. From these histograms and corresponding kernel density estimates, it can be seen that the predicted distributions have some differences from the actual but qualitatively they are mostly similar. To further assess this quantitatively, a number of tests for differences are applied, namely, the Kolmogorov-Smirnov (KS), Cramér–von Mises (CVM), $k$-sample Anderson-Darling (kAD), and Wilcoxon–Mann–Whitney (WMW) tests. Each of these tests, while distinct, have the same

purpose of testing how similar two sets of data are with a null hypothesis that the two sets of data are drawn from the same distribution. A value of 0.05 is applied to the results of the test to assess significance. On the training data, as expected, these tests return a value that does not reject the null hypothesis (*i.e.*, the underlying distributions are the same). However, when applied to the tests case, all tests except the WMW reject the null hypothesis that the data come from the same distribution. This is somewhat expected for predicted distributions such as figure 3.4g, but unexpected given the similarity in some predictions such as in figures 3.4i and 3.4b.

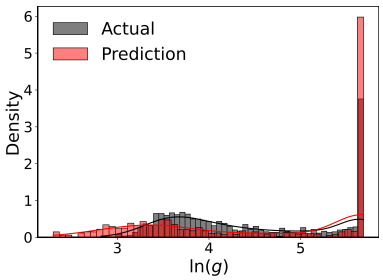


(a) Grain shear strength parameter

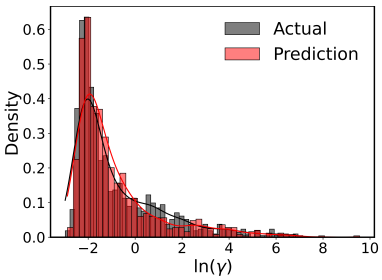


(b) Grain shear strain parameter

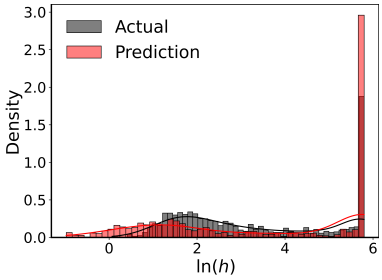


(c) Grain hardening modulus parameter

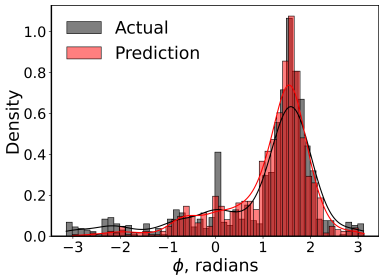


(d) Ellipsoid first Euler angle

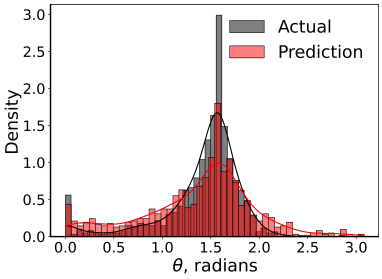


(e) Ellipsoid second Euler angle

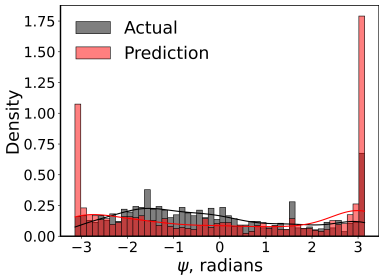


(f) Ellipsoid third Euler angle

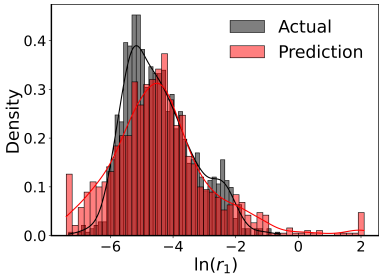


(g) Ellipsoid major axis radius

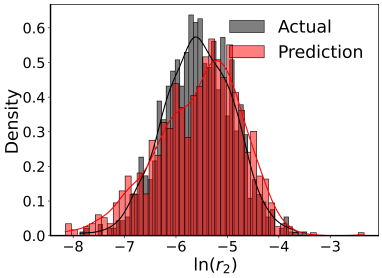


(h) Ellipsoid intermediate axis radius

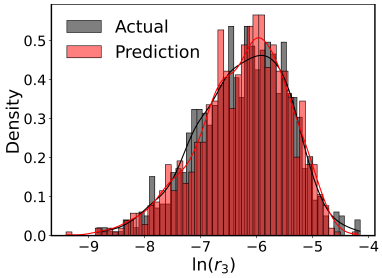


(i) Ellipsoid minor axis radius

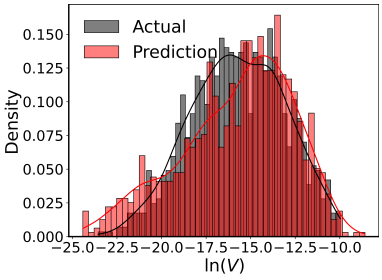


(j) Ellipsoid volume

Figure 3.4: Predicted versus actual distributions for the 10 parameter distributions. The natural log of the parameters is shown for all values except the Euler angles.

Rejecting the null hypothesis for the comparison tests is not ideal and suggests that there is potential for improvement in the MOGP, both during training and how the transformations are com-

pleted. However, two additional points can be made. First, even with the most realistic physics-based modeling, it is conceivable, especially with the large variability in AM, that two RVEs taken from the same larger microstructure could result in qualitatively similar microstructures and distributions but be dissimilar enough that tests for identical distribution could indicate that the RVEs were from different microstructures. Second, the purpose of the MOGP is ultimately to create a link from process modeling to the SP model and obtain an accurate property prediction. This link needs to be as accurate as possible, but the accuracy of the results after they are propagated through the whole framework will give much more insight into where time should be invested to make improvements (*i.e.*, changes in the MOGP accuracy may have a relatively minor influence on the predicted properties and it is not worth investing significant time in the MOGP to make minor improvements to the whole linkage). Therefor, the MOGP with qualitatively accurate predictive distributions and acceptable CV errors can be taken as is and reevaluated later for possible improvements.

### 3.5 Summary

This chapter has shown the development and demonstration of a multi-output GP with the purpose of linking process model outputs to microstructure statistics. In this case, the MOGP linked melt pool dimensions to 10 distributions of microstructure parameters. Microstructures were generated using a CAFE model and melt pool dimensions used to drive the CAFE and MOGP models were obtained from the models in chapter 2. Data from the CAFE model microstructures was extracted and transformed using quantile and normal distribution transformers such that mean and variance could be extracted. From the mean and variance of 10 distributions, 4 PCs were obtained that described 99% of the underlying data variance and these used to train the MOGP. 10-fold CV results on the PC components generally showed good agreement between the actual and predicted values. A withheld test case was used to further validate the MOGP. Qualitatively, the predicted de-transformed results were good, but when tests for differences were applied, most indicated the contrary. However, this was only a single test case so definitive conclusions cannot be drawn yet. Further test cases will be studied in chapter 5 when new data is propagated through

the full PSP linkage including the MOGP.

# 4. AM STRUCTURE-PROPERTY SURROGATE *

## 4.1 Introduction

In this chapter, the emphasis will be on understanding and generating ML-based structure-property linkages from simulated AM microstructures coupled with crystal plasticity finite element (CPFE) simulations. The CPFE method is a powerful tool for modeling the elastoplastic mechanical response of anisotropic, heterogeneous, polycrystalline aggregates by taking into account the effects of various microstructural features.[162, 163]

### 4.1.1 Columnar Grain Structures in AM

As mentioned in chapter 1, in AM processes, the continued melting and solidification involved in AM greatly influences the local microstructure. Furthermore, the microstructure of a multilayer build also is affected by the overlap of multiple scan tracks within a single layer along with the partial or full remelting of previously deposited layers.[164] A defining characteristic of the microstructure formed from AM processes is the presence of epitaxially grown columnar grains with different grain sizes and aspect ratios.[165, 166, 167, 168, 169, 170, 171, 172, 173] A consequence of the texture morphologies is varying mechanical properties with strong fiber $< 1\ 0\ 0 >$ textured microstructures, including a decrease in Young's modulus compared with non-textured AM microstructures.[165] Furthermore, elastic properties of AM parts can vary significantly depending on the orientation of the build direction with respect to the loading direction.[174, 175] AM materials with strong texture also are shown to have anisotropy in failure processes, such as fatigue crack growth.[166]

*Portions of this chapter have been reprinted with permission from R. N. Saunders, A. Achuthan, A. P. Iliopoulos, J. G. Michopoulos, and A. Bagchi, "Effects of the Microstructural Grain Size and Aspect Ratio on the Mechanical Properties of Additively Manufactured Parts via Computational Analysis," Def. Tech. Inf. Cent., no. NRL/FR/6353–20-10,411, 2020 and R. Saunders, C. Butler, J. Michopoulos, D. Lagoudas, A. Elwany, and A. Bagchi, "Mechanical Behavior Predictions of Additively Manufactured Microstructures using Functional Gaussian Process Surrogates," npj Comp. Mater., 7(1), 1-11, 2021.

### 4.1.2 CPFE Modeling in AM

A significant amount of work toward determining the mechanical behavior of AM metals exhibiting strong textures can be identified. Several experimental investigations have studied variations within an AM build.[176, 177, 178, 179] However, iteratively and exhaustively performing experiments can become prohibitively costly. As an alternative, CPFE simulations can be used to model the effects of AM microstructures on the macroscopic properties and performance of the material. Since grain morphology affects mechanical properties significantly, the computational models for the structural analysis of AM requires both a constitutive model that can capture accurately the microstructural dependence of the material behavior as well as a representative microstructure that features AM relevant elongated grain aspect ratios and crystallographic textures.[180, 181, 182] Few computational studies have utilized realistic, three-dimensional microstructures generated by simulations of the involved process. One effort utilized 3D CAFE model to model the AM process and CPFE simulations to simulate the spatial variation of microstructure and mechanical properties within a rectangular AM build.[183] In this study, the nucleation parameter used in the AM process simulation was varied to study the effect of grain size on response. Another recent study focused on microstructure and property variation between disparate AM processes rather than spatial variation within a single build.[184]

### 4.1.3 CPFE-based Machine Learning

Although the use of CPFE over experiments is, in general, more flexible and generates data at a lower cost, the computational cost can still be very high. One solution is to utilize ML. There are a number of ways in which an ML model can be trained to represent a CPFE model and link structure to properties.

One method is to use deep learning (DL) to learn the constitutive model response.[185, 186, 187] This method is applicable beyond CPFE and can incorporate true physical constraints of the problem during learning. However, DL requires a large training data set which can be infeasible to generate using the computationally CPFE model. Additionally, it is not clear whether this

method will yield acceptable performance when applied to polycrystalline microstructures, especially those with the complexity of AM microstructures, as this has not been addressed in existing literature studies. An alternative method to learning the constitutive model is to use microstructural features and directly relate them to certain quantities of interest (QoIs) [188, 189, 190, 191] ((*e.g.*, elastic modulus, yield strength, *etc.*)) or the full stress-strain behavior [192, 193, 194]. In an ML framework, it is conceptually straightforward to relate microstructural features directly to QoIs and this is very useful to characterize a given material or fit a given constitutive model. However, in characterizing the material by only a few QoIs a significant amount of information about the stress-strain history is lost and the constitutive model must be chosen *a priori*. It is anticipated that relating the microstructure morphological features to the full stress-strain history will provide benefits over just predicting certain QoIs but it is conceptually more difficult to predict the stress-strain response. Liu and Wu [192] propose a DL-like approach termed deep material network (DMN) where phases in a representative volume element (RVE) are characterized and then propagated through homogenization and rotation operations. The operations are done such that the analytical characterization, homogenization, and rotation acts nearly identically to the operations involved in a conventional artificial neural network (NN). Another approach by Frankel *et al.* [193, 194] directly implements a hybrid convolution, long short-term memory recurrent NN (ConvLSTM) to process a microstructure image and predict its full, spatially resolved stress-strain history. While the approaches of both methods differ substantially, both are able to show very high prediction accuracy on withheld data. However, both are based on DL, which as previously mentioned, has a large training data requirement. In the DMN and ConvLSTM models, hundreds of RVEs were generated for training, validation, and testing. In those works, generating hundreds of cases was feasible due to the relative simplicity of the constitutive models, dimensionality of the problem, and microstructures being examined. As mentioned before, AM microstructures do not exhibit such simplicity so the generation of hundreds of simulations for training will be prohibitively time consuming, even on the most advanced high-performance computing systems. Additionally, DL-based models do not have an inherent uncertainty quantification method.

#### *4.1.3.1 Functional Gaussian Process Modeling*

The recognition of the fact that CPFE models are displacement driven and the outputs of stress and strain are derived, continuous functions offers an opportunity for a new approach. Functional data analysis (FDA) is an area of statistics, which handles data that reside in an infinite dimensional space (*i.e.*, functions such as continuous time series data) [195]. As with traditional statistical methods, FDA has two methodologies, parametric [196] and non-parametric modeling [197, 198]. The latter set of methods deals with the case of modeling infinite dimensional functional data using non-parametric methods, which also follow a general infinite dimensional assumption. These methods are thus applicable to Gaussian processes (GPs) among other non-parametric methods. A number of authors have studied GPs with functional data and shown success in developing a functional predictive capability [199, 200, 201, 202, 203, 204]. Li *et al.* [205] even recognized the applicability of the functional Gaussian process (fGP) to AM thermal process simulations. As already pointed out, in CPFE a function (*i.e.*, displacement) can be related to another function ((*i.e.*, stress/strain)), but there is an additional requirement for the existence of a set of scalar parameters, such as grain morphology descriptors and constitutive model parameters that do not change with the displacement. The drawback of the fGP models developed in the previous works is that they are restricted to function-on-scalar ((*i.e.*, functional input, scalar output)) or function-on-function GP regression, but the current problem requires an approach to model function-on-mixed scalar and functional data. Recent developments by Wang and Xu [206] have addressed this restriction and allow for mixed scalar and functional input variables along with functional and/or scalar output variables.

### 4.1.4 Summary

In this chapter, an fPG framework is developed based on the fGP model of Wang and Xu [206] for predicting the stress-strain behavior of AM microstructures as they are related to microstructural morphology features. The GP-based system provides a fast, flexible, less data intensive alternative to existing DL methods and as a natural outcome, provides a predictive mean and variance

for the stress-strain history. Additionally, GP-based models, such as the one developed here, are easily generalizable to multi-output [207] and/or multi-fidelity [107, 208, 108, 109, 118] variants. The framework developed herein has the additional novelty of predicting stress-strain history on a per grain basis, meaning that the microstructures used for training can be much smaller (*i.e.*, fewer grains) than the microstructures to be approximated. The development of this framework will be shown and then trained using simulated microstructures from two sources. The initial training will use a low cost approximation to real AM microstructures to demonstrate feasibility of the framework. As part of this, the framework will be applied to previously unseen microstructures generated by the same method as the training/testing data and then be used to demonstrate how grain size and shape influence mechanical properties without the use of costly CPFE models. Once demonstrated, the fGP network is retrained using physics-based simulated microstructures and efficacy is addressed again. Finally, the work is summarized and discussed.

## 4.2 Methods

### 4.2.1 Data Generation

The crystal plasticity data in this work is based on a microstructural-informed CPFE model developed by Saunders *et al.* [209]. The microstructure-informed CPFE model is a phenomenological model, which has been modified to account for grain size and aspect ratio effects. This modification was directed specifically at capturing the non-conventional grain morphologies seen in AM parts. A brief description of the process used to generate, mesh, and simulate microstructures is given here but, for brevity, theoretical aspects of the constitutive model and full implementation details are omitted and the interested reader is referred to [209].

This work utilizes both a synthetic microstructure generation method known as the continuum diffuse interface model (CDIM) [210, 211] and the CAFE model as described in chapter 3 to generate microstructure data. The CDIM is capable of generating, in a matter of minutes, representative volume elements (RVEs) with features mimicking those seen in actual AM microstructures that can be used for crystal plasticity simulations. Once generated from either method, the microstructure

RVEs are automatically imported into Simpleware ScanIP (Synopsys, Mountain View, CA, USA) using a Python script, run through the Simpleware Scripting interface. The script then creates a single multi-label mask based on the greyscale information contained in the image data. Finally an unstructured volume mesh is generated and exported. The mesh comprises curved quadratic tetrahedral elements generated Simpleware's +FE Free algorithm. The density of elements is dependent on the geometry of the structure, with more smaller tetrahedra added where the surface requires greater representation. In regions of small or no geometric change, decimation is used to generate larger tetrahedral elements to reduce the size of the mesh files and so speed up simulation. The mesh settings chosen were optimized for the simulation hardware resources available. The simulation-ready meshes were exported in a *.inp format. Once meshed and exported, the RVE is processed again to incorporate periodic boundary conditions, assign constitutive model parameters, and apply the desired loading scenario. The RVE is simulated using Abaqus/Standard (Dassault Systems, Providence, RI, USA) and the constitutive model is implemented in a user material subroutine (UMAT). In this work, the microstructure morphology variations are the only input parameters being varied. Thus to generate the necessary data to train an fGP model, the process described above must be run iteratively to generate microstructures exhibiting a variety of different size and aspect ratio grains.

### 4.2.2 Functional Gaussian Process

A brief overview of GPs is first given before showing the extensions to a functional Gaussian process. For a complete derivation of GPs, the interested reader is directed to the landmark work of Rasmussen and Williams [212]. First, let the input variables be denoted by $\boldsymbol{X} = (\boldsymbol{x}_1, \ldots, \boldsymbol{x}_n)^T$ and let $f(\cdot)$ be an unknown stochastic process. A GP is a non-parametric statistical model in which $f(\cdot)$ is to follow an $n$-dimensional multivariate Gaussian distribution such that,

$$p(f(\boldsymbol{x}_1), \ldots, f(\boldsymbol{x}_n)) \sim \mathcal{N}_n(\boldsymbol{\mu}, \boldsymbol{k}), \tag{4.1}$$

where $\boldsymbol{\mu}$ is the mean vector defined by the mean function $\mu(\boldsymbol{x}_i) = \boldsymbol{\mu}_i = \mathbb{E}[f(\boldsymbol{x}_i)]$ and $\boldsymbol{k}$ is the covariance defined by the covariance function $k(\boldsymbol{x}_i, \boldsymbol{x}_j) = \boldsymbol{k}_{ij} = cov[f(\boldsymbol{x}_i), f(\boldsymbol{x}_j)]$. Now, the Gaussian process can be denoted as $f(\cdot) \sim \mathcal{GP}(\mu(\cdot), k(\cdot, \cdot))$. The standard problem of nonlinear regression takes the form

$$y_i(\boldsymbol{x}_i) = f(\boldsymbol{x}_i) + \epsilon_i, \tag{4.2}$$

where $f$ is as above and follows a GP, and $\epsilon_i$ are independent and identically distributed Gaussian random noise with 0 mean and $\sigma^2$ variance. It then follows that

$$\boldsymbol{y} = (y_1, \cdots, y_n)^T \sim \mathcal{N}(\boldsymbol{\mu}, \boldsymbol{K}), \tag{4.3}$$

where $\boldsymbol{\mu} = (\boldsymbol{\mu}_1, \cdots, \boldsymbol{\mu}_n)^T$ and $\boldsymbol{K} = \boldsymbol{k}_{ij} + \sigma^2 \boldsymbol{I}$, where $\boldsymbol{I}$ is the $n \times n$ identity matrix. The assumption of Normality is crucial to the GP framework as it allows the specification of a mean and covariance function that defines the presumed relationship between data points. As is common in many works, this work will assume that the mean function is $\mathbf{0}$. Furthermore, the covariance function will take the form of a Matérn $3/2$ covariance as

$$k(\boldsymbol{x}, \boldsymbol{x}') = \eta \left(1 + \sqrt{3 \sum_{k=1}^{p} \theta_k^2 (x_k - x_k')^2}\right) \exp\left(-\sqrt{3 \sum_{k=1}^{p} \theta_k^2 (x_k - x_k')^2}\right). \tag{4.4}$$

The parameters $\{\eta, \theta_1, \ldots, \theta_p, \sigma^2\}$ make up the set of so-called hyper-parameters, which allow "tuning" of the correlation between data points. The estimates of these parameters can be obtained through standard frequentist or Bayesian estimation. This work will utilize maximum likelihood estimate (MLE) throughout for simplicity. An additional outcome of the Normality assumption is that for a new input $\boldsymbol{x}^*$, the corresponding response is also Normally distributed and its mean and variance can be found as

$$\begin{aligned} y^* &= k(\boldsymbol{x}^*, \boldsymbol{X})^T \boldsymbol{K}^{-1} \boldsymbol{y}, \\ \sigma^{2*} &= k(\boldsymbol{x}^*, \boldsymbol{x}^*) - k(\boldsymbol{x}^*, \boldsymbol{X}) \boldsymbol{K}^{-1} k(\boldsymbol{X}, \boldsymbol{x}^*). \end{aligned} \tag{4.5}$$

In the derivation above, it has been assumed that $\boldsymbol{x}_i$ takes the form of a vector with scalar components. However, the data need not be of a scalar form and can take the form of functional data. With some modification to the above derivation, functional data can be incorporated into the GP. For the purposes of this work, the functional GP (fGP) will be restricted to functional outputs only. Extensions to scalar outputs are discussed following the derivation of the fGP.

The functional response $Y(t)$ can be defined as an $L_2$-continuous stochastic process on $\mathcal{T}$ such that the functional regression can be written as

$$Y_i(t) = f(\boldsymbol{X}_i(\cdot), \boldsymbol{z}_i) + \epsilon_i(t),\ t \in \mathcal{T}, \tag{4.6}$$

where $\boldsymbol{X}_i(\cdot)$ are now the $q$-dimensional functional parameters, $\boldsymbol{z}_i$ now represent $p$-dimensional scalar parameters, and the Gaussian noise is now functional as well with mean zero and variance $\sigma_\epsilon^2$. Utilizing functional principal component analysis (fPCA), $Y_i(t)$ can be decomposed as

$$Y_i(t) = \mu(t) + \sum_{j=1}^{J} \beta_{ij}\phi_j(t) + \epsilon_i(t),\ t \in \mathcal{T}, \tag{4.7}$$

where $\mu(t)$ is the functional mean of the stochastic process, the summation term is the decomposition of the stochastic process covariance truncated to the first $J$ terms, $\phi_j(t)$ are the stochastic process covariance eigenfunctions, and $\beta_{ij}$ is the $j$-th principal component of the $i$-th sample. The functional mean and eigenfunctions of the previous equation do not depend on the sample $i$ and as such can be determined using FDA methods without the use of a GP. Therefore, the problem of determining $Y_i(t)$ can be restated as two problems. First, determine the mean and eigenfunctions of the stochastic process as well as the noise variance using FDA. Second, relate the stochastic process principal components to the input parameters. The first process relies solely on the response data and acts as a linear shift and scaling of the data such that it has a zero mean. The second process can be stated as

$$\beta_{ij} = g_j(\boldsymbol{X}_i(\cdot), \boldsymbol{z}_i) + e_{ij}, \tag{4.8}$$

where $e_{ij} \sim \mathcal{N}(0, \sigma_j^2)$ with $\sigma_j^2$ being the Gaussian random noise variance of the $j$-th principal component and $g_j$ is an fGP for the $j$-th principal component. Following the process above for a standard GP, it can now be stated that

$$\boldsymbol{\beta}_j = (\beta_{1j}, \cdots, \beta_{nj})^T \sim \mathcal{N}(\mathbf{0}, \boldsymbol{K}_j), \tag{4.9}$$

where, with slight change in notation from above, $\boldsymbol{K}_j = \boldsymbol{k}_{lmj} + \sigma_j^2 \boldsymbol{I}$. The covariance $\boldsymbol{k}_{lmj}$ will again take the form of a Matérn $3/2$ as

$$\begin{aligned} k_j(\boldsymbol{X}, \boldsymbol{X}', \boldsymbol{z}, \boldsymbol{z}') = \eta_j & \left(1 + \sqrt{3 \sum_{k=1}^{p} \theta_{kj}^2 (z_k - z_k')^2}\right) \left(1 + \sqrt{3 \sum_{k=1}^{q} \omega_{kj}^2 ||X_k - X_k'||_k^2}\right) \\ & \exp\left(-\sqrt{3 \sum_{k=1}^{p} \theta_{kj}^2 (z_k - z_k')^2} - \sqrt{3 \sum_{k=1}^{q} \omega_{kj}^2 ||X_k - X_k'||_k^2}\right). \end{aligned} \tag{4.10}$$

As before, the scalar term containing $z_k$ is a standard Euclidean distance measure between data points that satisfies the properties of a metric space. However, the functional data term containing $X_k$ does not satisfy the requirements for a metric space so traditional distance measures are not sufficient. A semi-metric space is a relaxed version of a metric space and measures of distance can be developed in that space as discussed by Ferraty and Vieu [197]. This work will utilize the fPCA based semi-metric which defines the distance between functional data as

$$||X - X'||_r^2 = \sum_{k=1}^{r} \left( \int [X(t) - X'(t)] \, \nu_k(t) dt \right)^2, \tag{4.11}$$

where $\nu_k$ are the orthonormal eigenfunctions of the largest $r$ eigenvalue covariances, $\mathbb{E}[X(s)X(t)]$. Further discussion and practical implementation details are omitted here but can be found in [197]. Having specified the covariance, the hyper-parameter set can be identified as

$$\left\{\eta_j, \theta_{1j}, \ldots, \theta_{pj}, \omega_{1j}, \ldots, \omega_{qj}, \sigma_j^2\right\}$$

for every one of the $J$ truncated principal components. In order to determine the predictive functional response, $Y^*(t)$, given a set of inputs $(\boldsymbol{X}^*(t), \boldsymbol{z}^*)$, the predictive mean, $\boldsymbol{\beta}_j^*$, and variance, $\sigma_j^{2*}$, must be found as

$$\begin{aligned}\boldsymbol{\beta}_j^* =& k_j(\boldsymbol{X}^*(t), \boldsymbol{X}(t), \boldsymbol{z}^*, \boldsymbol{z})^T \boldsymbol{K}_j^{-1} \boldsymbol{\beta}_j, \\ \sigma_j^{2*} =& k_j(\boldsymbol{X}^*(t), \boldsymbol{X}^*(t), \boldsymbol{z}^*, \boldsymbol{z}^*) - \\ & k_j(\boldsymbol{X}^*(t), \boldsymbol{X}(t), \boldsymbol{z}^*, \boldsymbol{z}) \boldsymbol{K}_j^{-1} k_j(\boldsymbol{X}(t), \boldsymbol{X}^*(t), \boldsymbol{z}, \boldsymbol{z}^*).\end{aligned} \tag{4.12}$$

Now, the predictive mean and variance of the functional response can be found as

$$\begin{aligned}Y^*(t) =& \hat{\mu}(t) + \sum_{j=1}^{J} \boldsymbol{\beta}_j^* \phi_j(t), \\ \sigma^{2*}(t) =& \hat{\sigma}_\mu^2(t) + \sum_{j=1}^{J} \sigma_j^{2*} \phi_j^2(t) + \hat{\sigma}_\epsilon^2,\end{aligned} \tag{4.13}$$

where $\sigma_\mu^2(t)$ is the variance of the functional mean $\mu(t)$ and the $\hat{(\cdot)}$ notation has been introduced to denote values estimated using FDA methods. As an aside, the fGP utilized here has the capability to model any combination of functions/scalars to functions/scalars. The derivation above has shown function-on-function/scalar regression but one could reduce this to a case of function-on-scalar or function by simply eliminating, respectively, the first or second summation term in equation 4.10. Additionally, for scalar-on-function/scalar regression, the kernel of the standard GP (equation 4.4) can simply be replaced by the functional kernel (equation 4.10). The fGP is implemented in a Python class, while the FDA methods used to determine the functional mean and variance as well as the functional Gaussian noise variance are implemented in Matlab.

### 4.3 fGP Framework

The set of inputs needed for a CPFE model are the uniform kinematic displacement boundary conditions ($\boldsymbol{u}$, vector of functional variables) applied to the faces of an RVE over the duration of the simulation, constitutive model parameters ($\theta$, scalar variables) that define the material behavior, and the microstructure morphology (non-functional variables *i.e.*, scalar, vector, or tensor

variables). Additionally, a loading parameter ($\lambda$, scalar functional variable), such as amplitude over time, is used to incorporate history dependence into the model for situations where displacement or other quantities may be non-unique or non-monotonic (*e.g.*, loading-unloading experiments). During each time increment of the CPFE simulation, a step in displacement is taken based on the value specified by the loading parameter, and along with the previous state of stress and strain in an element, a new element strain is computed followed by a stress update for the element in the current increment. The output of this process at the end of the simulation is a stress-strain curve for each of the 6 stress/strain components at each finite element in the simulation. The stress and strain outputs at each element can be taken as is or processed further to obtain values such as equivalent strain and equivalent (von Mises) stress. Theses equivalent values, or the individual components, can then be homogenized over the whole RVE, over individual grains, or other subsets of the RVE. The process as described is shown in the directed graph of figure 4.1 and the same process can be emulated using fGPs. The same inputs to the CPFE model can be used as input to the fGP described in section 4.2.2. The loading parameter and displacement are treated as functional inputs while the constitutive model parameters and microstructural features are treated as non-functional inputs. Note, that the model as defined uses displacement as the driving deformation mechanism, but this could equivalently be replaced with a specified force or traction on an RVE face. These inputs are then used to train an fGP model that predicts the functional equivalent strain ($\epsilon$, denoted strain from hereon), and this in turn, is used alongside the previous inputs to train a second fGP, which predicts the functional equivalent stress ($\sigma$, denoted stress from hereon). The choice here to use equivalent stress and strain was made in order to obtain a scalar valued function that considers all components of stress/strain. However, this choice is inconsequential and any individual component of stress/strain could have also been used. In fact, all components of stress/strain could be considered by either training one fGP network per component or by modifying the fGP normality assumption to instead follow a multivariate normal. Further discussion on this extension is omitted as the implementation of a multivariate fGP is beyond the scope of this work.

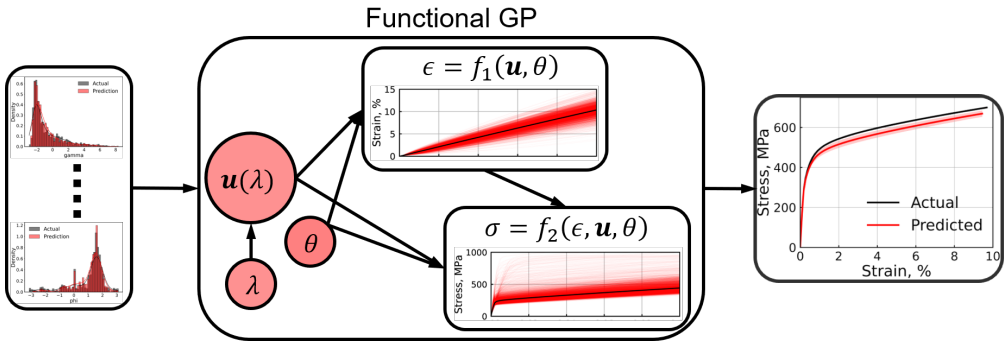


Figure 4.1: A functional Gaussian process graphical network, which uses a loading parameter ($\lambda$), displacement ($\boldsymbol{u}$), constitutive model parameters ($\theta$), and the microstructure morphology to predict stress ($\sigma$) and strain ($\epsilon$) in each grain and a mean response over a whole RVE.

In the illustrated graphical network, any set of microstructural features, such as those found by Mangal and Holm [213] and those discussed by Bostanabad *et al.* [214], that describe the RVE can be used. In AM, microstructures in many cases exhibit epitaxially grown columnar grains with different grain sizes and aspect ratios [184]. As such, in this work, a grain size- and shape-dependent CPFE model [209] is used to generate the needed crystal plasticity data. It follows that the features needed to describe grain size and shape, such as equivalent spherical diameter and grain volume, be used to represent the microstructural RVE as a set of non-functional scalar parameters. In general, this feature representation is done at the level of the whole RVE, but in this work, the feature representation is done at the level of each grain in an RVE. This, first, means that each time-consuming computationally-intensive CPFE simulation results in multiple stress-strain curves for each grain, rather than a single stress-strain curve for the whole RVE. This increases the amount of data available for training and testing the fGP models, which will help improve the predictive capabilities of the models. The drawback to this method of data collection is that the effect of boundary conditions and grain interactions is not considered. However, as will be shown in the following sections, these effects do not appear to significantly hinder the performance of the trained fGP model when given a sufficient amount of training data. Second, working at the level of the individual grain helps to directly relate grain size and shape features to the output stress-strain curve, rather than using dis-

tributions of grain size and shape for a whole RVE. By ignoring microstructure grain distributions and working with the individual grains, there are two means by which uncertainty is reduced. First, uncertainty in the microstructure feature distributions is effectively uncoupled from the mechanical property prediction, since there is typically not uncertainty associated with individual grains in a microstructure from the process-structure linkage. Second, by predicting individual grain behavior and then homogenizing, the variance of the predictive distribution, in general, is decreased since the variance of the mean decreases with sample size. Additionally, using the homogenized RVE response tends to mask the effect of small and elongated grains, which in the chosen constitutive model generally have higher stresses than large and equiaxial grains. This point is illustrated in figure 4.2 where some individual grains within a given RVE can have a stress of more than 3 times that of the homogenized RVE value at the same equivalent strain.

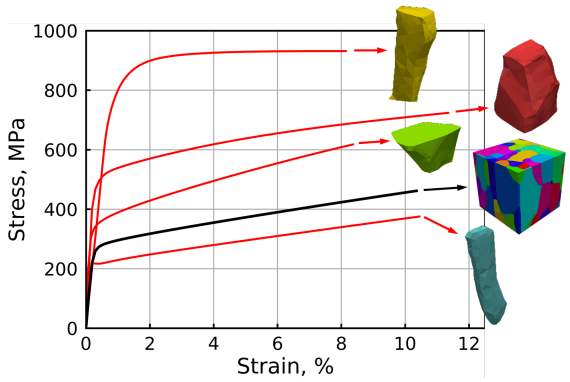


Figure 4.2: Comparison of homogenized RVE stress-strain behavior (black line) compared to individual grain behaviors from the same RVE (red lines) demonstrating how extreme gain behaviors can be masked through homogenization.

## 4.4 Initial Network Training and Evaluation

To train the initial network in figure 4.1, microstructural RVEs must be generated to be processed by the CPFE model. In AM, a single representative microstructure that is capable of representing the whole microstructure is generally not possible to construct. However, RVEs can be

constructed that contain a range of features (grain sizes, shapes, orientations, *etc.*) seen in the whole AM microstructure and that can be considered representative of the overall bulk material. As such, in this work, an RVE is defined as a volume element which contains a set of features representative of a larger AM build made with similar process parameters. For initial network training, 50 microstructural RVEs containing approximately 100 grains each are generated using a CDIM [211] and then meshed using Simpleware ScanIP (Synopsys, Mountain View, CA, USA). Complete details of the data generation process are given in section 4.2.1.

The generated RVEs contain features representative of those seen in single track AM microstructures [173] and a selection of the considered RVEs are shown in figure 4.3a. While the RVEs may not strictly resemble typically AM microstructures as the CAFE model microstructures do, they do provide a range of features, such as grain shape and size variations, that are seen in single track AM microstructures and that are needed to train the fGP network initially. The generated RVEs are cubic and have dimensions in the range of 0.1-0.8 $\text{mm}^3$. Periodic boundary conditions are specified for all faces along each axis and the loading parameter here is linear with time and monotonically increases from 0 to $10\%$ of the RVE edge length . The displacement is mapped such that it results in a linear, monotonically increasing displacement along the $Y$-axis in the $Y$-direction. The model setup represents the loading portion of a uniaxial tension test. If more complex loading behavior was desired, a simple change in definition of the loading parameter (amplitude) and $\boldsymbol{u}$ (direction) could accomplish that. The loading parameter definition will be valid as long it is a real, unique, continuous function and $\boldsymbol{u}$ simply maps that amplitude to a specific direction on an RVE face (*i.e.,* loading the $Y$-axis in the $Y$-direction is tension/compression and in the $X$- or $Z$-directions is shear). For instance, to address loading-unloading, the loading parameter would be specified as increasing (with no requirement on linearity) from some time $t_0$ until a future time $t_1$ then decreasing until another future time $t_2$. This type of specification could be extended to capture any non-monotonic or non-proportional behavior including cyclic or hysteretic behavior. Uniaxial tension is chosen here for simplicity and demonstration of the fGP network concept. The properties of 316L stainless steel are used for the constitutive model.

Running the simulations, extracting the stress-strain curves for each grain, and using 70% of the curves for training with the other 30% withheld for model evaluation, yields the data shown in figures 4.3b and 4.3c. The training and test sets are chosen at random. The mean strain of all these grains is around 10%, as expected based on the displacement magnitude and approximate size of the RVEs, with a stress of approximately 450 MPa at that strain. The range of strain for individual grains is between 8 and 15% with stress in the range of 325 MPa on the low end and, on the high end, some grains exceeding 1500 MPa. The importance of capturing grain stresses and strains far from the mean is based on the expectation that many grain with behaviors far from the mean will tend to have a high stress or strain energy density and will have a high probability of being a failure initiation site. Therefore it is crucial to be able to predict their their behavior. This also gives reason as to why it is necessary to train the fGP framework on a per grain basis.

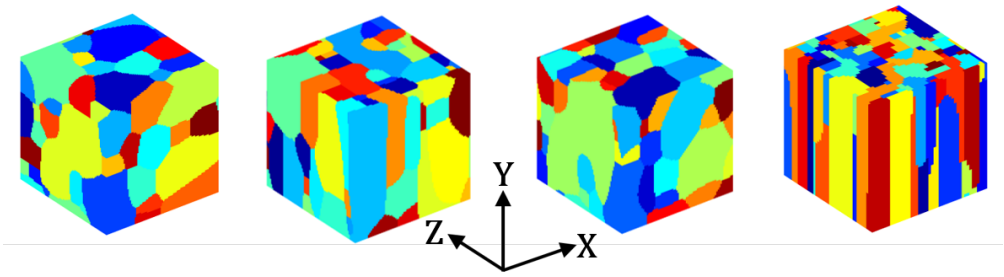


(a) Selection of 4 RVEs from the 50 generated and used for training.

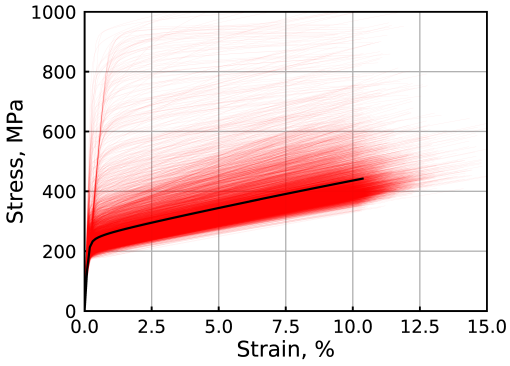


(b) Stress-strain curves of each grain (red lines) in the training data set along with the mean response of all the training data (black line).

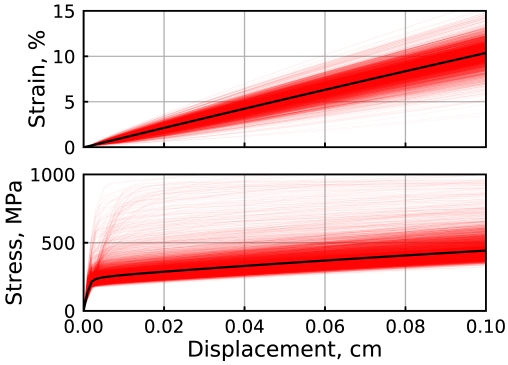


(c) Training stress and strain data shown against the commanded displacement.

Figure 4.3: fGP Training Data.

For the purpose of training the fGP models, only the properties in the constitutive model that are directly dependent on grain size and shape are considered. These are the grain yield strength, initial strain hardening modulus, and grain boundary resistance. Note that other constitutive model parameters, such as the stiffness tensor components, could readily be used in the parameter set but they are omitted here for simplicity. Additionally note, that any derived constitutive model quantities (*e.g.*, slip system strength, material axis rotation, *etc.*) are not explicitly considered, rather they are implicitly captured in the fGP since they will manifest as changes in the final stress-strain behavior. The microstructural features used to represent each grain are the grain total volume, three radii of an ellipsoid used to approximate the grain shape, and three angles representing the grains orientation relative to a defined, global axis. This set of morphological features is chosen

as they all can be directly and simply related to the size, shape, and orientation of the grains in the AM microstructure. As with the constitutive model parameters, additional morphological parameters (*e.g.*, texture, crystallographic orientation, Schmid factor, *etc.*) could be consider but are not implemented here for simplicity and interpretability. The selection of the features chosen for this work are specific for the AM process and the constitutive model used. In other manufacturing processes, other features such as Schmid factor may be more important or more relevant and these could be considered in the fGP in those instances. Furthermore, in ML, choosing a large number of features can be detrimental to model performance as it results in more hyper-parameters that must be tuned during training and more features can lead to lower model accuracy if those features are not strongly correlated to the output. The model, as described, results in 12 total hyper-parameters to be trained and training is done via maximum likelihood estimation (MLE). The number of functional principal components (section. 4.2.2, equation 4.7) used is $J = 3$ and this captures $> 99\%$ of the variability in the strain and the stress.

The overall results of the trained model on the withheld data can be seen in figure 4.4b, where the predicted mean nearly overlaps the mean of the CPFE data, and corresponding error rates are shown in table 4.1. Overall, the fGP network is able to predict the strain and stress to under $1\%$ error. These errors correspond to a prediction accuracy within $0.35\%$ strain and approximately 20 MPa stress. The prediction of the stress will in general be better than the prediction of the strain for two reasons. First, there is non-linearity in the constitutive model, which inherently means that uncertainty will between stress and strain will be different. Second, since the stress fGP will have additional information via the mean predicted strain, which helps to further differentiate data points that would otherwise be similar. Note, however, that when considering the full predictive strain distribution as the input to the stress fGP, uncertainty propagation methods would need to be utilized and may result in a less accurate predicted mean stress with a higher predicted variance.

Table 4.1: Error metrics for the trained fGP strain and stress models on the withheld grain data set. MSE - mean squared error, MAE - mean absolute error, MAPE - mean absolute percent error, SMSE - standardized mean squared error [212].

| | MSE | MAE | MAPE | SMSE |
|---|---|---|---|---|
| Strain | $3.282\text{e}{-5}$ | $3.546\text{e}{-3}$ | $7.834\%$ | $15.898$ |
| Stress | $1326.6\,\text{MPa}^2$ | $19.971\,\text{MPa}$ | $5.3\%$ | $22.995$ |

A selection of four grain stress-strain behaviors and the corresponding fGP mean prediction along with 95% prediction interval for those grains is shown in figure 4.4a. These results show mostly expected behavior in that if the grain stress-strain behavior is close to the mean behavior, the fGP can provide a good approximation, and as the grain behavior moves further away from the mean, the prediction intervals gets larger. In some cases, such as the left two images of figure 4.4a, the predicted behavior has very narrow prediction intervals and the CPFE data does not lie within those intervals. However, the important behaviors (*e.g.*, modulus, yield, and hardening) of individual grains tend to be captured very well by the fGP.

As mentioned above and as seen in figure 4.4a, the prediction of strain is more difficult than the prediction of stress. This can be attributed to a couple of training data deficiencies. First, in figure 4.3b, it can be noted that there is a high density of data around the mean, which will tend to bias the fGP toward that region. Next, it can be noted that, in general, the strain-displacement behavior is approximately linear for the majority of cases, but many grains can have significant non-linearity in this behavior. These grains tend to have the lowest prediction accuracy as they are outliers relative to the rest of the data. The reason for the presence of these non-linearaties is likely due to boundary/traction conditions around the grain. This could be the result of a grain being on the boundary of the RVE or the result of a grain being constrained by its neighboring grains. The latter problem could be addressed potentially by accounting for physical grain boundary conditions in the fGP. For instance, one could create a metric that defines the surface area of the grain in

contact with another grain. However, this would be quite challenging and may not result in a significant increase in model accuracy. To address the former problem, one would need to expand the training data set to include more cases that exhibit a non-linear strain response, which could be accomplished via different load paths, and would decrease uncertainty in the model. However, this could prove challenging as well since the fGP suffers from the need to perform an $\mathcal{O}(n^3)$ matrix inversion during training. Therefore with more than a few thousand data, a significant training time penalty will be incurred. This is known in the standard GP regression problem and exacerbated in the fGP problem where training must occur on each of the $J$ principal components. However, methods exist to circumvent this issue and these will be discussed later.

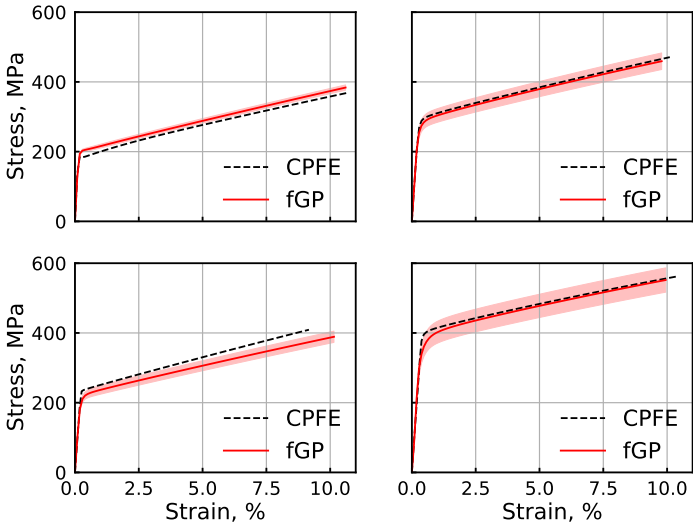


(a) fGP prediction with 95% prediction interval for four select grain data withheld from training.

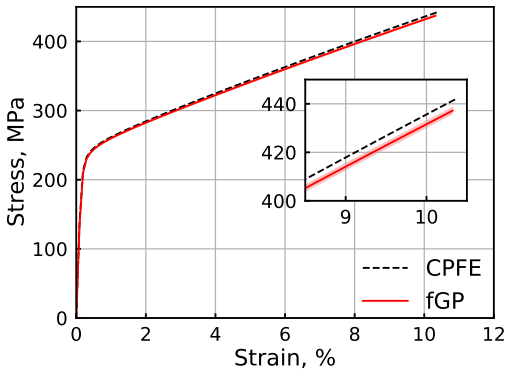


(b) fGP prediction with 95% prediction interval for the mean of all withheld data.

Figure 4.4: fGP Performance on Withheld Data

Recall that each RVE used during training contained approximately 100 grains. The fGP network is now applied to three RVEs of a more realistic size as will be seen with the CAFE model microstructures, containing upwards of 300 grains each, generated and simulated via the same process as before (*i.e.*, generation via CDIM, meshing via ScanIP, and CPFE simulation). The

generated RVEs in these cases are 0.125 $mm^3$. RVEs of this size generally take 60-90 hours of computational time to generate the stress-strain response for a whole RVE on a high performance computing system using 48 CPUs. This is in contrast to the 10-15 hours that the 100 grain RVEs used for training take on the same computing system. Additionally, a larger RVE will result in the boundary conditions having less influence on the overall RVE behavior and, in general, yield a more representative behavior. As mentioned, the fGP does not explicitly take into account the boundary conditions meaning that the learned behavior may be significantly influenced by the boundary conditions. Before running the CPFE simulations, fGP predictions were made using RVE features. Once the CPFE model was run, the stress-strain results for the whole RVE were extracted as shown in figure 4.5 alongside the fGP predictions.

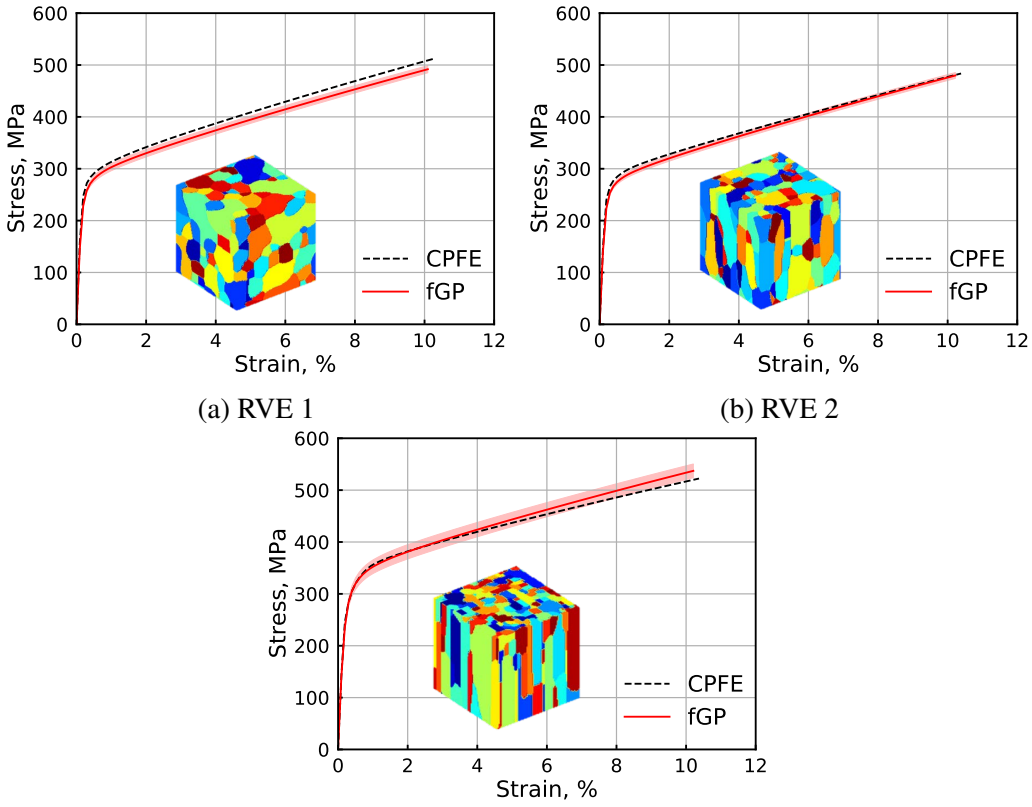


(a) RVE 1

(b) RVE 2

(c) RVE 3

Figure 4.5: Stress-strain results for three 300 grain RVEs not used for the training of the fGP network. CPFE results took approximately 3 days of computation time on average while fGP predictions with 95% prediction intervals took seconds.

The corresponding error metrics are shown in table 4.2 and in general show slightly higher error rates, as would be expected in ML on previously unseen data. However, the error rates are still of the same magnitude as those seen on the withheld training data and are sub-18% in the worst case, being sub-10% in the majority of cases, and in some cases are actually lower than the rates seen on the withheld training data. RVE 1 (figure 4.5a) shows the highest error rates of the three generated RVEs and can be attributed to a lack of sensitivity in the trained model. RVE 1 is nearly equiaxial and, as such, the distribution of grain sizes and shapes is relatively small. In the CPFE model, these small variations between grains are easily captured. However, in the fGP (as well as many other ML models), small local variations in input parameters are treated as similar to one another, even when they may not be, due to the characteristic length scale of the covariance being larger than the relative distance between some points.

Table 4.2: Error metrics for the trained fGP strain and stress models on the three new 300 grain RVEs as well as the total error rates for the combined data set consisting of approximately 900 grains.

| | | MSE | MAE | MAPE | SMSE |
|---|---|---|---|---|---|
| Total | Strain | 5.924e−5 | 4.954e−3 | 10.645% | 7.422 |
| | Stress | 6710.9 MPa$^2$ | 39.965 MPa | 8.284% | 19.094 |
| RVE 1 | Strain | 1.24e−4 | 8.064e−3 | 17.626% | 19.028 |
| | Stress | 5415.9 MPa$^2$ | 47.129 MPa | 10.486% | 41.846 |
| RVE 2 | Strain | 3.816e−5 | 4.124e−3 | 8.601% | 2.548 |
| | Stress | 3271.9 MPa$^2$ | 27.626 MPa | 6.327% | 8.982 |
| RVE 3 | Strain | 2.193e−5 | 3.004e−3 | 6.429% | 1.706 |
| | Stress | 10847.2 MPa$^2$ | 44.633 MPa | 8.107% | 8.375 |

Even considering the introduction of a small amount of error in the results, the reduction in

computational cost (by three orders of magnitude) makes the fGP framework much more tractable than running the CPFE model. As mentioned, RVEs of a sufficient size, such as those in figure 4.5, can take between 60 and 80 hours to simulate on an HPC system. In contrast, the fGP network data generation, training, and prediction took between 500 and 700 hours of time (50 RVEs at 10-15 hours on the same HPC system, 8 hours for training on a desktop, and prediction time was negligible on a desktop). While there is a significant time investment to construct the fGP network, the fGP network was trained in the same time as roughly ten CPFE simulations. However, the fGP network can provide a much more expansive data set than 10 CPFE simulations. To demonstrate this, the fGP will be used to examine how grain size and shape influence mechanical properties.

### 4.4.1 Grain Size and Shape Effects

To demonstrate the uses of the fGP network for future problems that may require many mechanical property predictions for various microstructures or microstructure distributions (*e.g.*, optimization or Bayesian sampling), a simple set of data with varied grain size and shape distributions will be created and mechanical properties predicted without the use of costly CPFE simulations. The data set consists of “microstructures" with average aspect ratios (shapes) of $1$, $3$, or $5$ and average grain volumes (sizes) of $1.891\text{e}{-5}$, $2.029\text{e}{-4}$, $2.178\text{e}{-3}$, $2.338\text{e}{-2}\,\text{mm}^3$. Distributions of grain sizes and shapes are generated via 200 random draws from a log-normal distribution with means as specified and standard deviations of $0.3$ for the grain shape and $1$ for the grain size. A full factorial analysis is performed to generate 12 representative microstructures with 200 grains each. Each of the 12 microstructure distributions is them simulated and homogenized via the fGP network to generate predicted mechanical behaviors as shown in figure 4.6. Note that $95\%$ prediction intervals are available for each curve but are omitted for figure clarity.

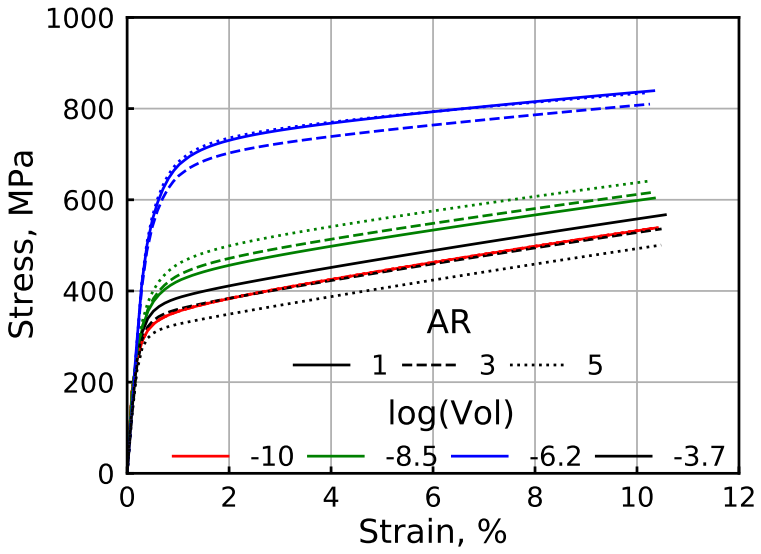


Figure 4.6: Stress-strain data from the fGP graphical network for the 200 grain “microstructures" generated via specifying a grain size and shape distribution. AR - average aspect ratio, log(Vol) - logarithm of the average grain volume.

The generation and mechanical property prediction of this data (all 12 microstructures) took approximately 1 hour on a standard desktop computer. The majority of this time was spent converting the input grain aspect ratio and volume into the necessary fGP inputs, which requires a numerical double integration. In contrast, if one were to attempt to simulate the same 12 RVEs with 200 grains using CPFE methods, each simulation would take upwards of a full day on an HPC system. The benefit of using the fGP network becomes even larger when considering that the time required has neglected the additional time needed to generate microstructural RVEs and mesh those RVEs before the CPFE model can be run. The drawback of the fGP is that there is a small amount of error introduced to be able to obtain these results so rapidly. However, this error will be small ($< 10\%$ as demonstrated on the 300 grain RVEs) so long as the fGP is being used in an interpolative manner (*i.e.*, the microstructural features being input are in the range of those used to train the model). In this case, this condition holds since the fGP was trained with data that had higher and lower volumes and aspect ratios. If this condition is not met, then the accuracy of the fGP network will quickly diminish.

With regard to the results of the mechanical behavior, the mechanical properties show trends that are consistent with the theory. A brief overview of this consistency is given here but the interested reader is referred to [209, 215] for full information on the constitutive theory. First, it can be noted that at a very small average volume ($log(Vol) = -10$) the aspect ratio has almost no influence on the mechanical behavior, since the grain is already "saturated". As average grain volume increase (regardless of aspect ratio), there is an initial increase in yield strength and a decrease in the hardening modulus, but at a high enough volume the yield strength decreases and the hardening modulus increases. This is indicative of the grain boundary effect being the dominant effect at intermediate volumes, but above a certain volume threshold, the grain boundary effect starts to diminish since the grain boundary volume is small relative to the overall volume. The effect of aspect ratio is confounded by the size effect, but generally shows that smaller grains with high aspect ratios produce a higher stress and this trend inverts with large grain sizes. The noted points are all consistent with the theory and the CPFE results presented in [209], which gives further credence to the accuracy of the fGP model and its ability to emulate the CPFE model well.

This has been a simple demonstration of the fGP network and its potential time-saving capabilities, but this is a relatively small problem with only 12 microstructures that could be solved using CPFE in a longer but doable time frame. However, even in this simple context, one can begin to see how the fGP network can be used in PSP linkages to determine a desired microstructural feature distribution that results in a specific mechanical behavior. For instance, if the goal was to maximize yield strength then from figure 4.6, a target should be to achieve a microstructure with an average volume of $2.178\text{e}{-3}\,\text{mm}^3$ ($log(Vol) = -6.2$) and either an equiaxial structure ($AR = 1$) or high aspect ratio structure ($AR = 5$). The true benefits of the fGP network are realized when considering an optimization problem or Bayesian sampling, where hundreds or thousands of microstructure feature distributions may be needed to find an optimal solution or the desired parameter distributions. With a CPFE model alone, this would be intractable, if not entirely impossible. With the fGP, this is not the case and the parameter space being explored can be thoroughly searched.

## 4.5 fGP Network Retraining - CAFE Data

As a point of demonstration, a smaller RVE (56.25 $\mu$m$^3$) is extracted from the microstructure shown in figure 3.1a to evaluate the performance of the fGP network that has been trained on CDIM microstructures. As discussed, the concept of an RVE in AM is a bit of a misnomer, as clearly there is no truly repeated, representative structure seen in figure 3.1. However, an RVE with a representative feature set can be extracted. While the fGP network could be used to analyze the full CAFE microstructure with many thousands of grains, that is not done here. The reason for this being that the fGP network needs a point of comparison. This means that whatever is chosen to evaluate the fGP network must be able to be simulated using the CPFE model, which is limited to simulating a few hundred grains. To remove bias, the subset selection is done randomly within the full microstructure. The chosen RVE and corresponding stress-strain behavior from the CPFE and fGP models are shown in figure 4.7.

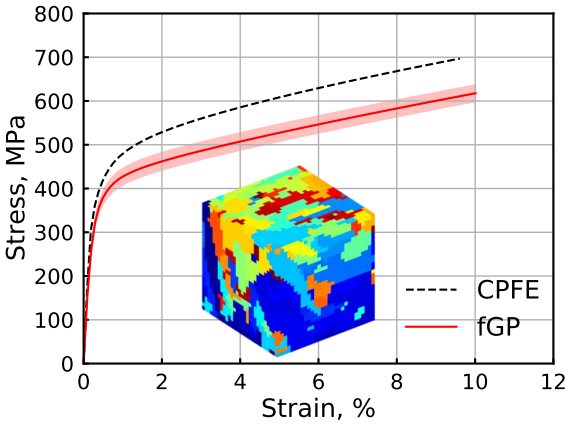


Figure 4.7: Stress-strain data from the CPFE model as well as the fGP graphical network for the shown RVE that was extracted randomly from the full microstructure of figure 3.1.

The results of the fGP network on the CAFE model microstructure are poor with much larger errors than those seen during training/testing of the model. However, this is not unexpected as the features seen in the CAFE RVE are significantly different than those seen in the original data

set. As discussed, the fGP network is a data driven ML model so it can **only** accurately make predictions on features with similarities to those it has seen before. As can be seen in the CAFE RVE, the microstructure includes grains which are oriented along many different directions, have many different aspect ratios, and many different sizes. However, during training of the fGP model, the CDIM was used to generate microstructures with grains grown along a single RVE axis with different aspect ratios and sizes.

Since the feasibility of the fGP network has been established by the previous section and in order to address the shortcomings of training with CDIM data, the fGP network is retrained with a subset of the microstructures generated in chapter 3. The results of retraining are shown in figure 4.8 and in table 4.3. The predictions are shown on a test set that consisted of 30% of the available data from the newly generated data set as was done before and the same CAFE model microstructure that was used in figure 4.7. Note that the errors shown in table 4.3 for the previous training are a different scale than shown in table 4.1 due to a change in the way error is calculated. The change was made so that two microstructures with differing numbers of grains could be compared (*i.e.*, so predicted outputs from the PS linkage could be propagated through the fGP network and compared to actual CPFE responses).

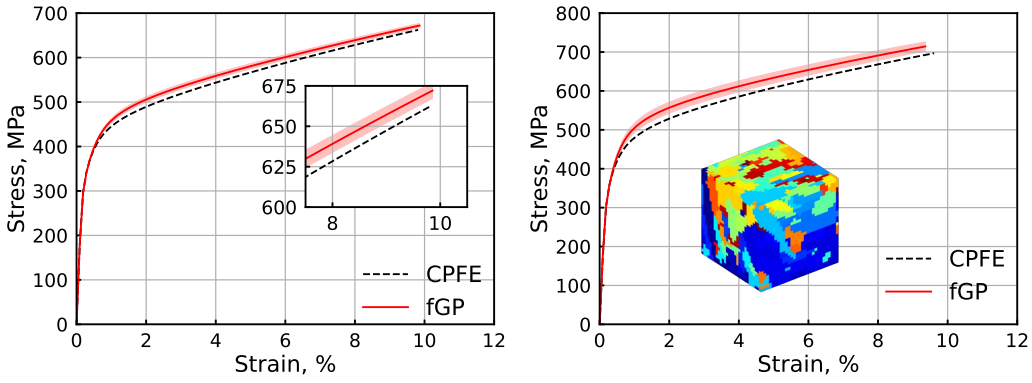


(a) Average response of withheld data after retraining.

(b) Predicted response of a CAFE RVE after retraining.

Figure 4.8: fGP network predictions for withheld test data and a withheld CAFE microstructure after retraining using CAFE model microstructures.

Table 4.3: Mean absolute percent error (MAPE) for the previous and current retrained fGP strain and stress models on the withheld grain data set and CAFE model microstructure.

| MAPE (%) | Test Data | | CAFE data | |
|---|---|---|---|---|
| | Previous | Current | Previous | Current |
| Strain | 0.595 | 0.698 | 3.92 | 3.91 |
| Stress | 0.980 | 2.41 | 15.01 | 3.41 |

The retrained fGP models show approximately the same MAPE in strain before and after retraining. However, the errors in stress increase for the test data but decrease drastically for the CAFE data. The increases in error for the test set can be attributed to the increased variability in the training data from the CAFE model microstructures. Likewise, the decrease in prediction error for the CAFE data are a result of the training data exhibiting more varied features similar to those found in the test CAFE microstructure thus resulting in a better prediction for a microstructure from the CAFE model. Note, the microstructure used in figure 4.8b was generated using process parameters that were not used in the training set and the microstructure implemented a different scan pattern than the training data.

## 4.6 Discussion and Summary

This chapter has demonstrated the development and application of a functional Gaussian process based graphical network. The fGP network emulates the simulation process for a CPFE model, where displacement and other input parameters are used to determine strain then stress in a grain. The fGP was initially trained using data from RVEs generated using a CDIM and then retrained using CAFE model microstructures. Both sets of data were simulated using a grain size and shape dependent CPFE constitutive model. Additionally, the amount of data was increased from the available RVEs by training the fGP network on a per grain basis rather than a per RVE basis. The fGP network was able to accurately predict new data from a test set and performed well

on new RVEs generated by the same means as the training data, with differing numbers of grains and, therefore, different boundary conditions. This result demonstrated the possible capabilities of the fGP network to predict unseen data and the performance suggests that large CPFE models, which are computationally too expensive to simulate, could be approximated well by the fGP network trained using very small, more manageable RVEs with similar features. This is consistent with the theory of using small statistical volume elements (SVEs, volume elements which individually do not capture the average response of the material) to approximate a much larger domain [216]. However, the more traditional approaches require extracting SVEs from the microstructure of interest, simulating those SVEs, and then homogenizing to approximate the behavior of the domain of interest. The novel approach taken here is much more general in that it learns feature sets applicable to all microstructures exhibiting similar feature sets and does not require the repeated simulation of SVEs.

Having shown the initial fGP network is capable of predicting unseen data, it was applied to a simple problem of simulating 12 “microstructures" and proved to be consistent with the crystal plasticity constitutive theory. The fGP network was able to make predictions on data three orders of magnitude faster than the corresponding CPFE model (minutes on a single CPU compared to hours/days on an HPC system). Additional time savings are realized when considering that the effort required to mesh and fully define a CPFE model is not required to run the fGP network. Of course, the fGP network also has some drawbacks and limitations, which primarily stem from training data and data being predicted. Since the fGP is network is data driven ML model, it can only accurately make predictions on features with similarities to those it has seen during training (*i.e.*, it is an interpolative model, not extrapolative). The less similar the unseen features are to the features seen during training, the worse the prediction will be. However, this is the case with all ML models.

The graphical network developed here provides a simple yet powerful data driven methodology to capture the structure-property relationship in AM PSP linkages. Due to its relative simplicity, it is extraordinarily flexible in that it is not limited to the CPFE constitutive model used in this work

or even limited to GP based methods. While a specific CPFE constitutive model was chosen for this work, the fGP network can be implemented on any crystal plasticity data, such as that generated by spectral methods [217] or any other crystal plasticity constitutive model [218]. Changes to constitutive model would require modifying the input features so that they are specific to the given model, which then necessitates retraining of the network, but the core concept and framework is still applicable. Since the graphical network directly emulates the crystal plasticity method and predicts stress as well as strain, constitutive models containing damage and failure as well as complex load histories can be used to train the fGP network. Damage and defects can also be incorporated into the fGP network via the RVE by the inclusion of voids and/or cracks inside the microstructure [219, 220]. The defects would be captured in the fGP network during the feature selection process. The drawback to this process is that the network training can no longer be done on a per grain basis and must be done on a whole RVE basis to capture defect distributions.

As mentioned, the framework developed here is not limited to GP based methods, but GP models have have the benefit of being well studied and easily modified. The extension of a standard GP to the fGP shown in section 4.2.2 was straightforward and other modifications such as extensions to multiple outputs, incorporating multiple fidelity data, and utilizing sparse methods for “big data" [221, 222] can be incorporated into the fGP. The extension of the fGP to incorporate multiple fidelity data could allow for both fast spectral methods and traditional slower non-spectral methods to be used simultaneously in the data generation and training processes. Sparse methods are the most immediately relevant extension to the problem at hand where training the fGP on thousands of grains using full rank methods becomes intractable, especially considering many of the grains from different microstructures have similar input-output pairs and contribute no new information to the fGPs.

Modifications to the input and outputs of the network could enhance the fGP network further. This work has focused on a simple loading procedure where a single component of displacement was specified, a monotonic linear loading parameter was used, and the equivalent stress and strain were output as scalar functions. The specification of the input to include multiple components

of displacement would be trivial and the fGP network does not need modification to account for this. Likewise, the specification of a generalized loading parameter is possible , as described above, as long as the loading parameter is a real valued, unique, continuous function. However, by specifying a non-linear, non-smooth, or non-monotonic parameter, difficulty in data generation (*i.e.*, CPFE simulation convergence) could be encountered. Incorporation of multiple displacement components and a complex loading parameter would allow the network to capture behavior such as loading-unloading scenarios and non-proportional loading. While this work has focused on the scalar functional equivalent stress and strain outputs, the fGP network can easily be extended to include multiple functional outputs corresponding to the six components of stress/strain, either by training multiple independent networks or by modifying the fGP to utilize a multivariate normality assumption. With proper specification of the training data using combined loads (*e.g.*, tension-torsion), the trained fGP network could directly emulate the anisotropic material stiffness tensor [223]. The implications of this are that Bayesian methods could be used to interrogate the trained fGP network to determine the approximate full stiffness tensor values (*i.e.* material properties).

# 5. AM PROCESS-STRUCTURE-PROPERTY SURROGATE LINKAGE

As has already been stated numerous times throughout this work, the establishment of relational PSP linkages for AM is crucial. The surrogate models established in this work have been setup in such as way that the outputs of one surrogate is the input to the next as shown by figure 1.2. This makes the linking of these surrogates a natural process and with each of the surrogates created, a demonstration of their linkage is shown. First, the test case from the MOGP model is propagated through the fGP and the predicted properties compared for a CAFE microstructure versus an MOGP predicted microstructure. Then, a demonstration of the full linkage where two sets of process parameters are propagated through the entire framework. These two sets of inputs, and the resulting microstructures, were not used in the training of any of the surrogates.

## 5.1 MOGP Test Case

As a first test of the developed surrogate models and their linkages, the test case of figure 3.4 is propagated through the PS and SP linkages. The output of this process along with the CAFE microstructure used to generate the data is shown in figure 5.1 with errors quantified in table 5.1. The first point that can be made is that the CAFE-CPFE (*i.e.*, the true value) requires approximately 36 hours on a high performance computing (HPC) system using 144 CPUs in parallel. In contrast, the CAFE-fGP solution requires approximately 8 hours, with the vast majority of the time and resources being used to run the CAFE model, and the MOGP-fGP solution takes only a couple minutes using a single CPU on a laptop. Next, it can be noted that the 2 predicted stress-strain curves are very similar to the physics-based model outputs.

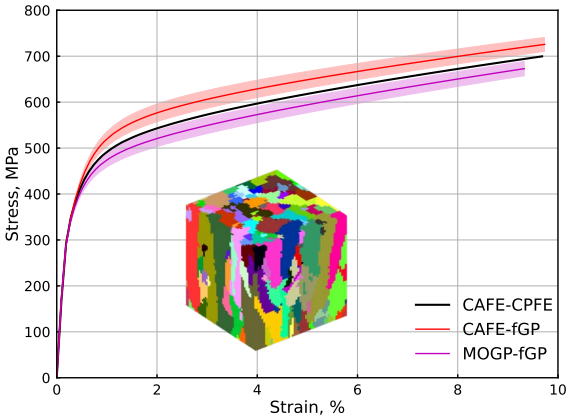


Figure 5.1: MOGP test case predicted properties compared to physics-based modeling properties with 95% GP predicted confidence interval.

Examining the error shows that, in fact, the predicted curves are all qualitatively and quantitatively similar. The error in predicted strain for the CAFE-fGP is approximately $1\%$ and approximately $5\%$ for the MOGP-fGP case. The predicted stress error for both is around $4-5\%$. Taken together, this indicates that an orders of magnitude reduction in computational time is possible with only a small penalty in error, which is to be expected with any predictive model. An additional point that can be made is that the fGP alone seems to over-predict the mechanical properties, while the MOGP predictions seem to bring that prediction back down and cause an under-prediction.

Table 5.1: MAPE for the predicted properties using the CAFE model microstructure and the MOGP output distributions of the same microstructure. The errors are quantified near the yield point, at the final increment, and over the whole curve.

| MAPE (%) | CAFE input | | MOGP input | |
|---|---|---|---|---|
| | Strain | Stress | Strain | Stress |
| $\approx 1\%$ Strain (Yield) | 2.25 | 6.02 | 6.05 | 4.47 |
| Final Increment | 0.514 | 3.73 | 3.68 | 3.83 |
| Overall | 1.12 | 4.91 | 4.72 | 4.38 |

## 5.2 New Inputs

To further examine the points made above and extend the predictions to include the MFGP melt pool dimension predictions, two new sets of process parameters are chosen from the withheld MFGP test cases and propagated through the full PSP linkage. These cases correspond to process parameters (P, V, S) of ($10\,W$, $100\,mm/s$, $300\,\mu m$) for test case 1 and ($600\,W$, $300\,mm/s$, $160\,\mu m$) for test case 2. These two cases represent a good demonstrative set of points as they are far from each other in terms of the process space. Case 1 is a low power, slow, wide beam whereas case 2 is a more focused, higher power, faster beam. For case 1, this set of parameters is close to a regime of where lack of fusion defects may occur, and for case 2, the parameters are close to the keyholing defect regime. In both cases, the experiment images shows that a melt pool was formed and did not exhibit keyholing or lack of fusion defects.

From these inputs, the process model surrogate is first queried. From this a classification of case 1 shows that the case is correctly classified as having no defect. Conversely, case 2 shows no defect in the experiment but is predicted as having a defect by both the classifier and regression-based classifier. As was discussed in chapter 2, LOF defects are easier to classify correct and case 1 was closer to this regime so a better classification is expected. Similarly, keyholing defects were more difficult to predict and case 2 is near the keyholing regime boundary hence higher probability of an incorrect classification. Nevertheless, both cases will be propagated through the PSP framework, even given the misclassfication, to assess the accuracy of the PSP linkage mechanical property predictions. The predictions for melt pool width and depth are shown in table 5.2. The prediction error rates of $5\%$ and $9.5\%$ for the width and depth, respectively, are similar to the validation set errors presented in chapter 2, as one would expect. The predicted and actual values can now be used as input to both the CAFE and MOGP models. Since experiment melt pool length is unavailable to evaluate the trained MOGP and propagate to the CAFE model, the length for both the predicted and actual values will be taken to be the melt pool length obtained by an FE model using the test case process parameters. This means that for case 1 predicted and actual, the melt pool length is assumed to be $375\,\mu m$. Likewise for case 2, the length will be $745\,\mu m$.

Table 5.2: Melt pool dimension predictions and error for two test cases.

| Test Case # | Actual ($\mu m$) | | Predicted ($\mu m$) | | Error ($\%$) | |
|---|---|---|---|---|---|---|
| | Width | Depth | Width | Depth | Width | Depth |
| 1 | 320 | 84 | 307 | 76 | 4.06 | 9.52 |
| 2 | 176 | 64 | 186 | 58 | 5.68 | 9.38 |

The CAFE model microstructure RVEs from the melt pool dimensions of table 5.2 are shown in figure 5.2. Qualitatively, the microstructures of both cases look similar between the actual and predicted input melt pool dimensions. Quantitatively, when the tests for differences in distributions of chapter 3 are applied to the predicted versus actual melt pool dimension microstructures, the tests reject the null hypothesis at the 0.05 level that the underlying distributions are different for all 10 parameters (*i.e.*, there is not sufficient evidence to conclude that the microstructures are not from the same larger volume). This is true for both cases. These tests are again applied on each of the 4 microstructures to compare the CAFE model distributions to the predicted MOGP model distributions. Unlike the test case of chapter 3, the hypothesis tests mostly indicate that the MOGP distributions are the same as the CAFE distributions. For instance,the KS test does not reject the null hypothesis for case 2 actual microstructure of figure 5.2c. However, the same data with the kAD test does reject the null hypothesis. Overall, the predicted microstructure distributions are substantially similar to the actual distributions so the data is next propagated through the SP linkage to determine how differences in melt pool dimensions and microstructure distributions manifest as changes in predicted properties.

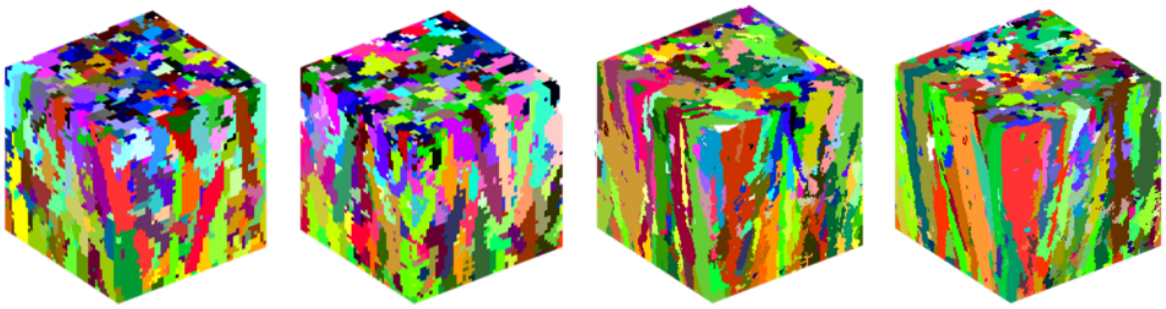

(a) Test case 1 actual melt pool.

(b) Test case 1 predicted melt pool.

(c) Test case 2 actual melt pool.

(d) Test case 2 predicted melt pool.

Figure 5.2: CAFE model microstructures for both test cases using both the actual and predicted melt pool dimensions.

The predicted properties for both test cases are shown in figure 5.3 with 5 combinations of predictions and actual PSP linkages shown. In both cases, the real property is the EXP-CAFE-CPFE. What can first be noticed is that, as stated before, the fGP alone tends to over predict the stress while the models with an MOGP estimate tend to underestimate the stress. Strain does not appear to follow this same behavior. The fGP demonstrating this consistent over-prediction behavior is unique to the sets of RVEs examined in this work and a result of the data that the model was trained on. On average, the fGP tends to over-predict mechanical properties as demonstrated in figure 4.8a, but in many cases will also under-predict the mechanical properties. The under-prediction from the MOGP has to do with learned features from the microstructure and how the constitutive model handles these features. The underlying constitutive model is affected by grain size and shape such that very small or very elongated grains have a strain hardened effect. Due to the way that the quantile and normal transformations are done in the MOGP, the predictions tend to be more concentrated at the central portion of the distribution. In the central portion of the distribution, the predicted grain parameters tend to be less elongated and of a more moderate size resulting in a lower prediction of mechanical properties. The effect of the MFGP predicted melt pool versus the actual melt pool appears to be small and shows no consistent over or under prediction affect on the mechanical properties.

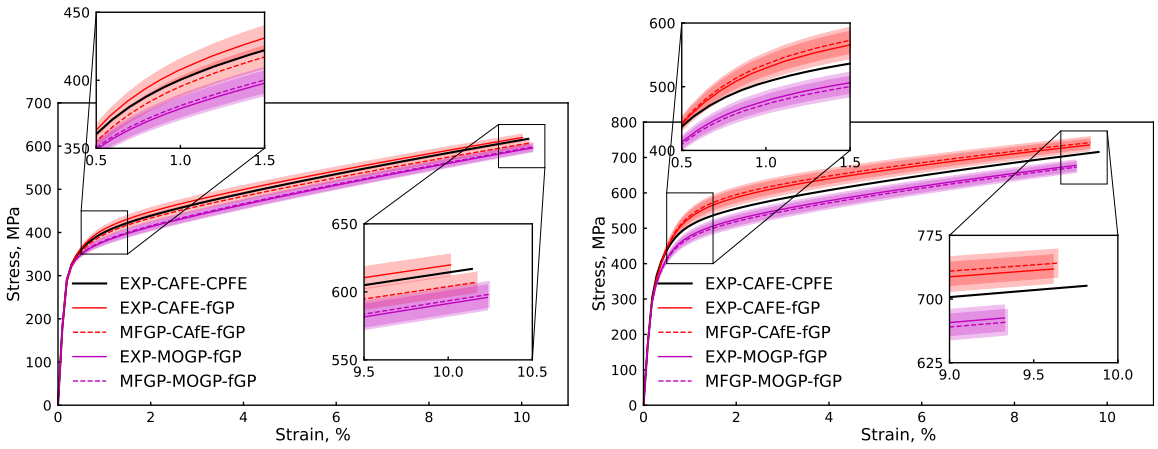


(a) Average response of withheld data after retraining.

(b) Predicted response of a CAFE RVE after retraining.

Figure 5.3: fGP network predictions with 95% confidence interval for withheld test data and a withheld CAFE microstructure after retraining using CAFE model microstructures.

The most important results of figure 5.3 are the comparisons between EXP-CAFE-CPFE and MFGP-MOGP-fGP, which represent the comparison between a physics-based PSP linkage and an ML-based PSP linkage. This comparison is shown in figure 5.4 and tables 5.3 for both case 1 and case 2. The primary comparison to be made here, again, is that the physics-based linkage requires multiple days of experimental and computational time whereas the ML model, once trained, requires only a few minutes of resources on laptop. The cost of this resource reduction is an error penalty of around $5\%$ and $< 10\%$ at the single worst point for an orders of magnitude speedup.

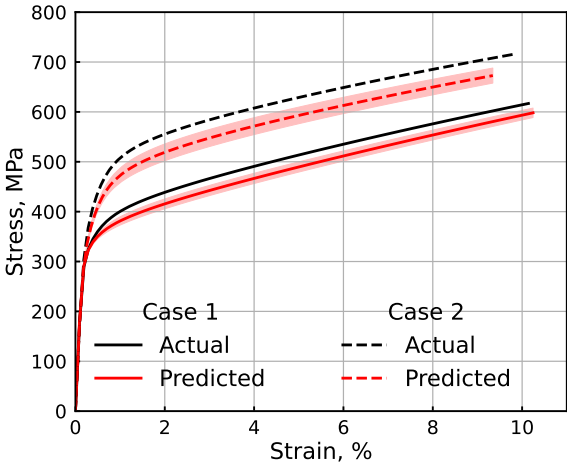


Figure 5.4: PSP linkage mechanical property predictions for the actual physics-based approach and the predicted ML approach with 95% confidence interval.

Table 5.3: MAPE for PSP linkage mechanical property predictions for the actual physics-based approach and the predicted ML approach. Error is quantified at approximately the yield point, the final increment, and as an average over the whole prediction.

| MAPE (%) | Test Case 1 | | Test Case 2 | |
|---|---|---|---|---|
| | Strain | Stress | Strain | Stress |
| $\approx 1\%$ Strain (Yield) | 1.57 | 4.60 | 9.26 | 8.35 |
| Final Increment | 1.02 | 3.03 | 4.78 | 5.98 |
| Overall | 1.54 | 3.97 | 6.65 | 6.90 |

The trade-off in resources and error is well understood for other problems and, depending on the specific application, is worthwhile. The ML-based PSP linkages would not be ideal for making the best possible prediction of mechanical properties resulting from a set of process parameters, but make it possible to sample an entire space of process parameters in a reasonable amount of time for Bayesian analysis or optimization problems. This could result in a first approximation

of the best solution to a given problem or a small range of process parameters that result in the desired mechanical properties. This could then be augment with a few simulations to further refine the solution and finally a single experiment to verify what was found. Without the ML-based PSP linkage, this process could require 100s of experiments to obtain the same solution and resource constraint would likely limit this to 10s of experiments, almost guaranteeing that an optimal solution would not be found.

One issue of note with the predictions in figure 5.4 are that the actual solutions do not fall within the confidence interval (CI) from the fGP. This is a result of the CI only being the predicted standard deviation from the fGP model. In order to get a complete CI, uncertainty propagation from the beginning process parameters is necessary. While doing this is beyond the scope of this work, other works have already demonstrated the feasibility of linking multiple GPs in AM then quantifying and propagating uncertainty using Bayesian approaches.[78] Doing so would increase the CIs of the predicted values and, given the small difference between the actual and predicted values, would result in the actual value being encompassed by the CI of the predicted value.

# 6. SUMMARY AND FUTURE WORK

## 6.1 Summary

A GP-based PSP relation linkage for L-PBF 316L stainless steel has been developed and demonstrated. This linkage, first, classifies a set of process parameters to determine if a porosity defect may occur. The linkage, next, relates the process parameters to melt pool dimensions, then links these to microstructure statistics, and ultimately to mechanical properties through a series of 3 GP surrogates. Each of the surrogates is trained on a limited set of data and demonstrated good predictive accuracy through validation either using a test set method or cross-validation method.

For the process modeling surrogate of chapter 2, four fidelities AM thermal data were sampled using a nested Latin-hypercube sampling scheme. A multi-fidelity non-linear auto-regressive GP was implemented, including the development and demonstration of a novel GP-based classification method. The classification results demonstrated mixed results but overall showed adequate performance with roughly 80% accuracy. The multi-fidelity regression results were able to predict melt pool width with 95% accuracy and melt pool depth with 90% accuracy. The regression results demonstrated significantly better performance over standard single fidelity GPs.

The process-structure surrogate linked melt pool dimensions from the process modeling to microstructure statistics using an MOGP. The MOGP extracted information from CAFE model microstructures, transformed the data, and then related melt pool dimensions to 4 PCs. Cross validation results showed good agreement between predictions and actual values. A test case, once reconstructed was qualitatively good but quantitatively not in agreement with underlying data. Further test cases, when propagating information through the entire PSP linkage, showed both qualitative and quantitative agreement.

In the structure-property surrogate, microstructure statistics from both CDIM and CAFE microstructures were used to drive a CPFE model which generated the data necessary train an fGP. This fGP linked microstructure features, such as grain size and aspect ratio, to uniaxial stress-strain

behavior. A surrogate modeling framework consisting of two networked functional GPs was established and its efficacy was demonstrated on a test data set. Furthermore, the fGP network was demonstrated to be accurate on a test data set that was previously unseen and a sample application of the network was shown. Limitation of the fGP network were addressed by retraining the fGP using data from only CAFE model microstructures. The retrained model demonstrated comparable accuracy on a test data set to the CDIM trained model but with a much richer feature set used during retraining. Predictions with the retrained model showed an order of magnitude improvement in accuracy on an unseen CAFE microstructure.

The developed process model, PS, and SP surrogates were finally linked and shown to be accurate on two previously unseen sets of process parameters. Yielding around 95% accuracy in the mechanical property predictions with an orders of magnitude reduction in prediction time. This process also demonstrated predictions of melt pool dimensions and microstructure statistics that were similar to the expected error rates based on the validation data.

## 6.2 Future Work

One advancement that could be applied to all of the surrogate models in this work is the incorporation of physics-informed neural networks (PINNs) instead of GPs.[224, 225, 226, 227, 228, 229] While GPs exhibit a favorable number of attributes, they suffer from a number of drawbacks in scaling to large datasets and, in particular, capturing and considering physical constraints. The lack of physical constraints is well documented in many ML models and is a growing concern as ML becomes more and more prominent in science and engineering. PINNs are a new class of neural network that can be trained to learn the underlying physics of the problem. While PINNs are still in their infancy, their application in this framework would increase its flexibility and ensure that the physics of AM are being properly accounted for.

### 6.2.1 Process Modeling Surrogate

First, more process parameters (*e.g.*, hatch spacing, raster pattern, *etc.*) and powder properties can be consider to improve the flexibility of the model. With more multi-track AM thermal

models being developed, the consideration of a process surrogate that accounts for full scan pattern/histories can be constructed. The full scan surrogate could be accomplished by modeling the spatial fields using one latent subspace [230] and the temporal fields by the fGP surrogate shown in chapter 4. By capturing the full spatial-temporal thermal history, quantities such as the melt pool dimensions and the solidification gradient could be directly obtained from the surrogate output for the full mesoscale part build. Since these methods are still based on GPs, then the developed processes of this work would still be applicable. In particular, an MFGP could be constructed that combined NEASM and experimental scan histories. This, however, still would not address a lack of melt pool length prediction for the experiments. As mentioned, one method to obtain information about melt pool length measurements (beyond measuring them *in-situ*) is to have a multi-output variation of the MFGP where there is coupling between the melt pool dimensions. Combined with Bayesian analysis, the missing experimental melt pool length data could be imputed. Due to the hierarchical nature of the MFGP implemented in this work, a multi-output extension is possible without significant alterations to the model. In the classification setting, extensions of the nonlinear multi-fidelity GP to multi-class classification could improve the classification algorithm. However, multi-class GP classification is a much more difficult problem than the binary case implemented in this work and would almost certainly require training via Markov-chain Monte Carlo or similar approximation methods.

### 6.2.2 Process-Structure Surrogate

As with the process modeling surrogate, the PS surrogate could be modified to account for more scan patterns and be extended to account for more features from the process model, such as solidification gradient, or additional features from the microstructure like spatial or two point statistics. The advancement to PINNs, as discussed, is a possible avenue for improvement of this model. However, an additional avenue that can be explored is the construction of true microstructure emulator using a generative adversarial network (GAN) or a similar deep learning-based auto-encoder. GANs like PINNs are a relatively new and advanced technique but are rapidly being deployed to model physical phenomena.[231, 232, 233, 234, 235, 236, 237, 238, 239] A number of these works

have even begun to consider the task of microstructure generation either from scalar parameters or from 2D exemplars.[160, 240, 159, 241, 158, 242] Again however, there is considerable research still to be done in order to represent microstructures as complex as those produced in AM in 3D. Since GANs are based on deep learning techniques, transfer learning could be of considerable importance where a GAN could be trained initially using kMC or CAFE microstructures, then later retrained on a much smaller dataset of experimental microstructures.

### 6.2.3 Structure-Property Surrogate

There are a number of possible improvements in the SP surrogate, some of which have already been discussed in chapter 4. One immediate modification that can be considered is to account for complex load paths such as non-proportional loading. One of the larger tasks that could be undertaken with this surrogate is to utilize combine load paths to generate sufficient data that a full representative material stiffness tensor could be extracted. By doing this, microstructure features could be linked to the micro/meso-scale properties and then those properties used in a macroscale analysis of a full part. The scaling to a full part is enable by the fact that the fGP network can be scaled to predict mechanical properties of large microstructures, far beyond those able to be simulated with CPFE approaches. As such, the fGP network has the potential be implemented in a multi-scale material modeling framework.[243] In this framework, the fGP network could act as the solution to a localized, micro/mesoscale problem and inform the larger macroscale problem. In doing so, the computational cost of a multi-scale problem would essentially reduce to the cost of solving only the macroscale problem.

Another application of the fGP is for Bayesian calibration and optimization. While Bayesian analysis of the PSP linkages will be discussed more in the subsequent section, it is worth discussing here the possible use of the fGP to aid in calibration efforts. A major barrier to using many of the developed CPFE models is obtaining appropriate and sufficient constitutive model parameters. Traditional methods involve either trail-and-error approaches or a extracting properties from data in literature or previously used value in literature. This is obviously not an ideal approach as it can be time consuming and result in an inaccurate model or possibly an inability to even identify the

necessary parameters. Since the fGP can be trained to account for constitutive model parameters, it can essentially emulate the whole crystal plasticity constitutive model and be trained on synthetic data. Since it has such a low cost to sample, the fGP could be used in an optimization workflow to efficiently and more accurately identify constitutive model parameters for new materials that have been tested. Furthermore, a Bayesian approach could be taken to identify probability distribution associated with these parameters and which are most likely or which have little to no influence on the resulting model.

### 6.2.4 Process-Structure-Property Linkage

While individual improvements to each underlying surrogate of the PSP linkage are possible, one of the most necessary tasks for the framework on the whole is uncertainty propagation (UP) and uncertainty quantification (UQ). As established and demonstrated the current framework has a clear linkage where one output is the input to the next model. However, since each of the models are based on GPs, each model actually has normally distributed outputs with an estimated mean and variance rather than a scalar value. The propagation of these distributions through the framework will have a substantial impact on the predicted values of each model and the corresponding uncertainty. Ye *et al.* [78] has already established and demonstrated a methodology that could be applied to the models of this work as well.

Performing a Bayesian analysis of the framework will have a number of benefits. First, it will aid in the determination of which surrogate model(s) results in the largest sources of error. This will demonstrate where improvements discussed above should be focused and where the best return on time spent will be obtained. Doing this Bayesian analysis will also demonstrate the feasibility of sampling the linkage 100s or 1000s of times. Once it is determined to be feasible, a number of other problems can be undertaken. First, sensitivity analysis to assess how changes in process parameters manifest as changes in microstructure features and mechanical properties, and which process parameters and microstructure features have the most impact on mechanical properties (as was demonstrated in section 4.4.1), which are most likely to result in high stresses or strain energy densities, potentially leading to material failure. Next, inverse PSP linkages will be possible with

the developed framework once setup in a way that it can be sampled thoroughly. Inverse PSP linkages will allow a given/desired mechanical property to be input and the framework can be sampled until a set of process parameters is obtained that results in those properties. Finally, it is also possible, and potentially desirable, to generate a final surrogate ML model that encompasses the 3 surrogate models of this work, creating a direct linkage between process and properties. In doing so, the speed at which data could be generated would further increase to real time. This would make an online system feasible and could be used as part of the controller in an AM machine.

### 6.2.5 Experimental Validation

While validation, in the ML sense, has been done for each model, there has been no experimental validation effort beyond the process model surrogate. For the process-structure and structure-property surrogates, experimental validation can be done for the underlying physics-based model and the surrogate can be considered validated if the validation set data used to evaluate the surrogate shows sufficient accuracy. This assumption is based on a transitive property of the validation in that if the physics-based model is validated by showing a high enough accuracy on an experimental data set, and the surrogate is validated by showing a high accuracy in emulating the physics-based model, then this implies that the surrogate would also demonstrate a high accuracy on the experimental data set. For the PS model, a full validation effort would involve the collection of multiple 3D microstructures produced by a known set of process parameters and with known melt pool dimensions. While this task is technically possible, it would be prohibitively expensive. In lieu of this, 2D sections can be collected and compared to the CAFE model outputs as was done in [157]. Thus, the PS model can be consider validated by the means described above.

For the SP model, however, there is no such validation of the underlying CPFE model. However, once it is validated, the fGP could be considered validated as discussed. One method to achieve a validated CPFE model would simple be to change to a different already validated model and retrain the fGP. This is a rather trivial solution but one that would work. An alternative would be to perform both calibration and validation of the current CPFE model by leveraging the already developed fGP network. Experiments using ASTM dog bone tension specimens built using L-PBF

and 316L powder would be required to validate the model. These specimens would be printed as solid rectangular blocks and then cut to ATSM standard sizes to avoid surface defects that could influence the mechanical behavior. Simple tension tests would be performed using the samples. Some of the tests will be randomly selected for calibration, while the remaining tests will be used for validation. An additional challenge here, is that the process parameters would be known but not the microstructure. To obtain the microstructure would necessitate the collection of 3D EBSD data for multiple specimens or the reconstruction of 3D AM microstructures from multiple perpendicular 2D exemplars. EBSD in 3D is not trivial and obtaining even a single sectioned 3D sample can take weeks. Additionally, as was mentioned in chapter 3, the reconstruction of AM microstructures from 2D exemplars is not well established. An alternative solution to the calibration and validation of the SP surrogate without obtaining microstructure information is to leverage the full PSP surrogate linkage and jointly validate the SP surrogate and the PSP surrogate.

Recall that the fGP network can be used to calibrate parameters of a constitutive model by retraining the fGPs to account for those parameters. In order to perform a joint calibration and validation, it will be necessary to perform this retraining of the fGP surrogate. By adding the CPFE constitutive model parameters to the fGP and the whole PSP linkage, Bayesian calibration of the parameters can be accomplished by sampling the PSP linkage with a known set of process parameters until a minimum error is achieved between the calibration experiments and the surrogate model prediction. In order to properly do the model calibration, knowledge of the microstructure along with the corresponding mechanical properties is needed. But as stated, gathering information about the microstructure can be difficult/infeasible. In lieu of this, the microstructure can be assumed to be unobservable. The approach to calibration with unobservable variables is similar to the work of Mahmoudi *et al.* [70], except all components of the PSP linkage will be used. Once the calibration is complete, the obtained constitutive model parameters can be input to the CPFE model to compare the physics-based predictions to the experiments. If the CFPE and experiments agree reasonably well, the constitutive model parameters in the fGP network can be fixed and the process parameters unfixed. This process would result in a validated CPFE model and, by the

method discussed above, a validated fGP network. Finally, the process parameters for the validation experiments can be input to the PSP linkage and predicted mechanical properties obtained then compared to experiments. If the results agree then the whole PSP framework can be considered validated.

### 6.2.6 Materials Design

A final application and modification that can be made to the developed framework is to extend it beyond a single material and AM process. While the framework has been developed and trained using a L-PBF and 316L stainless steel, there is nothing in the framework that limits it to a single material or process. In fact, each of the GP models is quite flexible and could be modified to account for additional materials or constitutive parameters as part of the input parameter space. By expanding the set of material parameters that each surrogate model is trained on, specific material attributes can be linked to resulting properties. This would enable materials design to further enhance the attainable properties from AM.

An interesting concept for materials design, that goes beyond simply having multiple materials in the trained models, could be to train the GPs in such a way that material composition is considered. There is ongoing work where chemistry of arbitrary alloys can be obtained from CALPHAD and be combined with the Eager-Tsai solution to create printability maps without having a defined material composition *a priori*. A similar approach could be applied to the physics-based models in this work where, from these compositions, material parameters for the thermal, microstructure, and mechanical models could be obtained. This process to obtain the necessary material parameters from a given composition would be daunting but, ultimately, doing so would allow materials scientists to study desired compositions that result in properties of interest. Furthermore, by applying the workflow developed here to the composition-agnostic models would drastically reduce the time to explore the search space for possible new AM material candidates.

# REFERENCES


[1] D. L. Bourell, "Perspectives on Additive Manufacturing," *Annual Review of Materials Research*, vol. 46, pp. 1–18, jul 2016.

[2] J.-P. P. Kruth, M. C. Leu, and T. Nakagawa, "Progress in additive manufacturing and rapid prototyping," *CIRP Annals - Manufacturing Technology*, vol. 47, pp. 525–540, jan 1998.

[3] G. N. Levy, R. Schindel, and J. Kruth, "Rapid Manufacturing and Rapid Tooling With Layer Manufacturing (LM) Technologies, State of the Art and Future Perspectives," *CIRP Annals*, vol. 52, pp. 589–609, jan 2003.

[4] C. Buchanan and L. Gardner, "Metal 3D printing in construction: A review of methods, research, applications, opportunities and challenges," *Engineering Structures*, vol. 180, pp. 332–348, 2019.

[5] S. H. Huang, P. Liu, A. Mokasdar, and L. Hou, "Additive manufacturing and its societal impact: a literature review," *The International Journal of Advanced Manufacturing Technology*, vol. 67, pp. 1191–1203, jul 2013.

[6] D. Herzog, V. Seyda, E. Wycisk, and C. Emmelmann, "Additive manufacturing of metals," *Acta Materialia*, vol. 117, pp. 371–392, sep 2016.

[7] D. D. Gu, W. Meiners, K. Wissenbach, and R. Poprawe, "Laser additive manufacturing of metallic components: materials, processes and mechanisms," *International Materials Reviews*, vol. 57, pp. 133–164, may 2012.

[8] T. DebRoy, H. Wei, J. Zuback, T. Mukherjee, J. Elmer, J. Milewski, A. Beese, A. Wilson-Heid, A. De, and W. Zhang, "Additive manufacturing of metallic components – Process, structure and properties," *Progress in Materials Science*, vol. 92, pp. 112–224, mar 2018.

[9] F. P. Melchels, M. A. Domingos, T. J. Klein, J. Malda, P. J. Bartolo, and D. W. Hutmacher, "Additive manufacturing of tissues and organs," *Progress in Polymer Science*, vol. 37, no. 8,

pp. 1079–1104, 2012.

[10] S. V. Murphy and A. Atala, "3D bioprinting of tissues and organs," *Nature Biotechnology*, vol. 32, no. 8, pp. 773–785, 2014.

[11] D. Bourell, J. P. Kruth, M. Leu, G. Levy, D. Rosen, A. M. Beese, and A. Clare, "Materials for additive manufacturing," *CIRP Annals*, vol. 66, no. 2, pp. 659–681, 2017.

[12] W. Du, X. Ren, C. Ma, and Z. Pei, "Ceramic binder jetting additive manufacturing : Particle coating for increasing powder sinterability and part strength," *Materials Letters*, vol. 234, pp. 327–330, 2019.

[13] M. K. Thompson, G. Moroni, T. Vaneker, G. Fadel, R. I. Campbell, I. Gibson, A. Bernard, J. Schulz, P. Graf, B. Ahuja, and F. Martina, "Design for Additive Manufacturing: Trends, opportunities, considerations, and constraints," *CIRP Annals - Manufacturing Technology*, vol. 65, no. 2, pp. 737–760, 2016.

[14] W. Gao, Y. Zhang, D. Ramanujan, K. Ramani, Y. Chen, C. B. Williams, C. C. Wang, Y. C. Shin, S. Zhang, and P. D. Zavattieri, "The status, challenges, and future of additive manufacturing in engineering," *Computer-Aided Design*, vol. 69, pp. 65–89, dec 2015.

[15] Fast Track Action Subcommittee on Critical and Emerging Technologies, "Critical and Emerging Technologies List Update," tech. rep., National Science and Technology Council, February 2022.

[16] "Fact sheet: Biden administration celebrates launch of am forward and calls on congress to pass bipartisan innovation act," May 2022.

[17] "Exec. order no. 14,017, 86 c.f.r. 11849. (2021)."

[18] U.S. Department of Defense, "Securing defense-critical supply chains," tech. rep., 2022.

[19] U.S. Department of Energy, "America's strategy to secure the supply chain for a robust clean energy transition," tech. rep., 2022.

[20] Under Sectrary of Defense for Research and Engineering, "USD(R&E) Technology Vision for an Era of Competition," tech. rep., US Department of Defese, 2022.

[21] M. Francois, A. Sun, W. King, N. Henson, D. Tourret, C. Bronkhorst, N. Carlson, C. Newman, T. Haut, J. Bakosi, J. Gibbs, V. Livescu, S. Vander Wiel, A. Clarke, M. Schraad, T. Blacker, H. Lim, T. Rodgers, S. Owen, F. Abdeljawad, J. Madison, A. Anderson, J.-L. Fattebert, R. Ferencz, N. Hodge, S. Khairallah, and O. Walton, "Modeling of additive manufacturing processes for metals: Challenges and opportunities," *Current Opinion in Solid State and Materials Science*, vol. 21, pp. 198–206, aug 2017.

[22] T. Tancogne-Dejean, A. B. Spierings, and D. Mohr, "Additively-manufactured metallic micro-lattice materials for high specific energy absorption under static and dynamic loading," *Acta Materialia*, vol. 116, pp. 14–28, sep 2016.

[23] L. Hirt, A. Reiser, R. Spolenak, and T. Zambelli, "Additive Manufacturing of Metal Structures at the Micrometer Scale," *Advanced Materials*, vol. 29, p. 1604211, may 2017.

[24] Q. Geng, D. Wang, P. Chen, and S.-c. Chen, "Ultrafast multi-focus 3-D nano-fabrication based on two-photon polymerization," *Nature Communications*, vol. 10, p. 2179, dec 2019.

[25] A. Roschli, K. T. Gaul, A. M. Boulger, B. K. Post, P. C. Chesser, L. J. Love, F. Blue, and M. Borish, "Designing for Big Area Additive Manufacturing," *Additive Manufacturing*, vol. 25, pp. 275–285, jan 2019.

[26] C. Greer, A. Nycz, M. Noakes, B. Richardson, B. Post, T. Kurfess, and L. Love, "Introduction to the design rules for Metal Big Area Additive Manufacturing," *Additive Manufacturing*, vol. 27, pp. 159–166, may 2019.

[27] Y. M. Wang, T. Voisin, J. T. McKeown, J. Ye, N. P. Calta, Z. Li, Z. Zeng, Y. Zhang, W. Chen, T. T. Roehling, R. T. Ott, M. K. Santala, P. J. Depond, M. J. Matthews, A. V. Hamza, and T. Zhu, "Additively manufactured hierarchical stainless steels with high strength and ductility," *Nature Materials*, vol. 17, pp. 63–71, jan 2018.

[28] J. A. Turner, J. Belak, N. Barton, M. Bement, N. Carlson, R. Carson, S. DeWitt, J. L. Fattebert, N. Hodge, Z. Jibben, W. King, L. Levine, C. Newman, A. Plotkowski, B. Radhakrishnan, S. T. Reeve, M. Rolchigo, A. Sabau, S. Slattery, and B. Stump, "ExaAM: Metal additive manufacturing simulation at the fidelity of the microstructure," *International Journal of High Performance Computing Applications*, vol. 36, no. 1, pp. 13–39, 2022.

[29] M. Matthews, T. Roehling, S. Khairallah, T. Tumkur, G. Guss, R. Shi, J. Roehling, W. Smith, B. Vrancken, R. Ganeriwala, and J. McKeown, "Controlling melt pool shape, microstructure and residual stress in additively manufactured metals using modified laser beam profiles," *Procedia CIRP*, vol. 94, pp. 200–204, 2020.

[30] A. Molkeri, D. Khatamsaz, R. Couperthwaite, J. James, R. Arróyave, D. Allaire, and A. Srivastava, "On the importance of microstructure information in materials design: PSP vs PP," *Acta Materialia*, vol. 223, p. 117471, 2022.

[31] D. Gunasegaram, A. Murphy, A. Barnard, T. DebRoy, M. Matthews, L. Ladani, and D. Gu, "Towards developing multiscale-multiphysics models and their surrogates for digital twins of metal additive manufacturing," *Additive Manufacturing*, vol. 46, p. 102089, oct 2021.

[32] J. H. Panchal, S. R. Kalidindi, and D. L. McDowell, "Key computational modeling issues in Integrated Computational Materials Engineering," *Computer-Aided Design*, vol. 45, pp. 4–25, jan 2013.

[33] H. Lim, F. Abdeljawad, S. J. Owen, B. W. Hanks, J. W. Foulk, and C. C. Battaile, "Incorporating physically-based microstructures in materials modeling: Bridging phase field and crystal plasticity frameworks," *Modelling and Simulation in Materials Science and Engineering*, vol. 24, p. 045016, may 2016.

[34] J. Smith, W. Xiong, W. Yan, S. Lin, P. Cheng, O. L. Kafka, G. J. Wagner, J. Cao, and W. K. Liu, "Linking process, structure, property, and performance for metal-based additive manufacturing: computational approaches with experimental support," *Computational Mechanics*, vol. 57, pp. 583–610, apr 2016.

[35] M. Markl and C. Körner, "Multiscale Modeling of Powder Bed–Based Additive Manufacturing," *Annual Review of Materials Research*, vol. 46, pp. 93–123, jul 2016.

[36] M. Diehl, M. Groeber, C. Haase, D. A. Molodov, F. Roters, and D. Raabe, "Identifying Structure–Property Relationships Through DREAM.3D Representative Volume Elements and DAMASK Crystal Plasticity Simulations: An Integrated Computational Materials Engineering Approach," *JOM*, vol. 69, pp. 848–855, may 2017.

[37] W. Yan, Y. Lian, C. Yu, O. L. Kafka, Z. Liu, W. K. Liu, and G. J. Wagner, "An integrated process–structure–property modeling framework for additive manufacturing," *Computer Methods in Applied Mechanics and Engineering*, vol. 339, pp. 184–204, sep 2018.

[38] W. Yan, S. Lin, O. L. Kafka, Y. Lian, C. Yu, Z. Liu, J. Yan, S. Wolff, H. Wu, E. Ndip-Agbor, M. Mozaffar, K. Ehmann, J. Cao, G. J. Wagner, and W. K. Liu, "Data-driven multiscale multi-physics models to derive process–structure–property relationships for additive manufacturing," *Computational Mechanics*, vol. 61, pp. 521–541, may 2018.

[39] P. Liu, Z. Wang, Y. Xiao, R. Lebensohn, Y. Liu, M. Horstemeyer, X. Cui, and L. Chen, "Integration of phase-field model and crystal plasticity for the prediction of process-structure-property relation of additively manufactured metallic materials," *International Journal of Plasticity*, vol. 128, p. 102670, may 2020.

[40] H. Fayazfar, M. Salarian, A. Rogalsky, D. Sarker, P. Russo, V. Paserin, and E. Toyserkani, "A critical review of powder-based additive manufacturing of ferrous alloys: Process parameters, microstructure and mechanical properties," *Materials and Design*, vol. 144, pp. 98–128, 2018.

[41] S. Mahadevan, P. Nath, and Z. Hu, "Uncertainty Quantification for Additive Manufacturing Process Improvement: Recent Advances," *ASCE-ASME J Risk and Uncert in Engrg Sys Part B Mech Engrg*, vol. 8, mar 2022.

[42] T. Mukherjee and T. DebRoy, "A digital twin for rapid qualification of 3D printed metallic components," *Applied Materials Today*, vol. 14, pp. 59–65, mar 2019.

[43] N. Kouraytem, X. Li, W. Tan, B. Kappes, and A. Spear, "Modeling process-structure-property relationships in metal additive manufacturing: a review on physics-driven versus data-driven approaches," *Journal of Physics: Materials*, nov 2020.

[44] S. R. Kalidindi and M. De Graef, "Materials Data Science: Current Status and Future Outlook," *Annual Review of Materials Research*, vol. 45, pp. 171–193, jul 2015.

[45] A. Agrawal and A. Choudhary, "Perspective: Materials informatics and big data: Realization of the "fourth paradigm" of science in materials science," *APL Materials*, vol. 4, p. 053208, may 2016.

[46] D. M. Dimiduk, E. A. Holm, and S. R. Niezgoda, "Perspectives on the Impact of Machine Learning, Deep Learning, and Artificial Intelligence on Materials, Processes, and Structures Engineering," *Integrating Materials and Manufacturing Innovation*, vol. 7, pp. 157–172, sep 2018.

[47] F. E. Bock, R. C. Aydin, C. J. Cyron, N. Huber, S. R. Kalidindi, and B. Klusemann, "A Review of the Application of Machine Learning and Data Mining Approaches in Continuum Materials Mechanics," *Frontiers in Materials*, vol. 6, may 2019.

[48] T. Lookman, P. V. Balachandran, D. Xue, and R. Yuan, "Active learning in materials science with emphasis on adaptive sampling using uncertainties for targeted design," *npj Computational Materials*, vol. 5, p. 21, dec 2019.

[49] D. L. McDowell and R. A. LeSar, "The need for microstructure informatics in process–structure–property relations," *MRS Bulletin*, vol. 41, pp. 587–593, aug 2016.

[50] S. R. Kalidindi, A. J. Medford, and D. L. McDowell, "Vision for Data and Informatics in the Future Materials Innovation Ecosystem," *JOM*, vol. 68, pp. 2126–2137, aug 2016.

[51] R. Ramprasad, R. Batra, G. Pilania, A. Mannodi-Kanakkithodi, and C. Kim, "Machine learning in materials informatics: recent applications and prospects," *npj Computational Materials*, vol. 3, p. 54, dec 2017.

[52] S. Ramakrishna, T.-Y. Zhang, W.-C. Lu, Q. Qian, J. S. C. Low, J. H. R. Yune, D. Z. L. Tan, S. Bressan, S. Sanvito, and S. R. Kalidindi, "Materials informatics," *Journal of Intelligent Manufacturing*, vol. 30, pp. 2307–2326, aug 2019.

[53] D. B. Brough, D. Wheeler, J. A. Warren, and S. R. Kalidindi, "Microstructure-based knowledge systems for capturing process-structure evolution linkages," *Current Opinion in Solid State and Materials Science*, vol. 21, pp. 129–140, jun 2017.

[54] R. Liu, A. Kumar, Z. Chen, A. Agrawal, V. Sundararaghavan, and A. Choudhary, "A predictive machine learning approach for microstructure optimization and materials design," *Scientific Reports*, vol. 5, p. 11551, sep 2015.

[55] N. H. Paulson, M. W. Priddy, D. L. McDowell, and S. R. Kalidindi, "Reduced-order structure-property linkages for polycrystalline microstructures based on 2-point statistics," *Acta Materialia*, vol. 129, pp. 428–438, may 2017.

[56] Z. Yang, Y. C. Yabansu, R. Al-Bahrani, W.-k. Liao, A. N. Choudhary, S. R. Kalidindi, and A. Agrawal, "Deep learning approaches for mining structure-property linkages in high contrast composites from simulation datasets," *Computational Materials Science*, vol. 151, pp. 278–287, aug 2018.

[57] A. Khosravani, A. Cecen, and S. R. Kalidindi, "Development of high throughput assays for establishing process-structure-property linkages in multiphase polycrystalline metals: Application to dual-phase steels," *Acta Materialia*, vol. 123, pp. 55–69, jan 2017.

[58] X. Qi, G. Chen, Y. Li, X. Cheng, and C. Li, "Applying Neural-Network-Based Machine Learning to Additive Manufacturing: Current Applications, Challenges, and Future Perspectives," *Engineering*, vol. 5, no. 4, pp. 721–729, 2019.

[59] C. Wang, X. P. Tan, S. B. Tor, and C. S. Lim, "Machine learning in additive manufacturing: State-of-the-art and perspectives," *Additive Manufacturing*, vol. 36, p. 101538, jan 2020.

[60] N. S. Johnson, P. S. Vulimiri, A. C. To, X. Zhang, C. A. Brice, B. B. Kappes, and A. P. Stebner, "Invited review: Machine learning for materials developments in metals additive manufacturing," *Additive Manufacturing*, vol. 36, 2020.

[61] L. Jannesari Ladani, "Applications of artificial intelligence and machine learning in metal additive manufacturing," *Journal of Physics: Materials*, vol. 4, p. 042009, oct 2021.

[62] J. Qin, F. Hu, Y. Liu, P. Witherell, C. C. Wang, D. W. Rosen, T. W. Simpson, Y. Lu, and Q. Tang, "Research and application of machine learning for additive manufacturing," *Additive Manufacturing*, vol. 52, feb 2022.

[63] G. Tapia and A. Elwany, "A Review on Process Monitoring and Control in Metal-Based Additive Manufacturing," *Journal of Manufacturing Science and Engineering*, vol. 136, p. 060801, dec 2014.

[64] M. Khanzadeh, S. Chowdhury, M. Marufuzzaman, M. A. Tschopp, and L. Bian, "Porosity prediction: Supervised-learning of thermal history for direct laser deposition," *Journal of Manufacturing Systems*, vol. 47, pp. 69–82, apr 2018.

[65] L. Scime and J. Beuth, "Using machine learning to identify in-situ melt pool signatures indicative of flaw formation in a laser powder bed fusion additive manufacturing process," *Additive Manufacturing*, vol. 25, pp. 151–165, jan 2019.

[66] Y. Chen, H. Wang, Y. Wu, and H. Wang, "Predicting the printability in selective laser melting with a supervised machine learning method," *Materials*, vol. 13, no. 22, pp. 1–12, 2020.

[67] T. Moges, G. Ameta, and P. Witherell, "A Review of Model Inaccuracy and Parameter Uncertainty in Laser Powder Bed Fusion Models and Simulations," *Journal of Manufacturing Science and Engineering*, vol. 141, p. 1, apr 2019.

[68] G. Tapia, A. H. Elwany, and H. Sang, "Prediction of porosity in metal-based additive manufacturing using spatial Gaussian process models," *Additive Manufacturing*, vol. 12, pp. 282–290, 2016.

[69] G. Tapia, L. Johnson, B. Franco, K. Karayagiz, J. Ma, R. Arroyave, I. Karaman, and A. Elwany, "Bayesian Calibration and Uncertainty Quantification for a Physics-Based Precipitation Model of Nickel–Titanium Shape-Memory Alloys," *Journal of Manufacturing Science and Engineering*, vol. 139, no. 7, p. 071002, 2017.

[70] M. Mahmoudi, G. Tapia, K. Karayagiz, B. Franco, J. Ma, R. Arroyave, I. Karaman, and A. Elwany, "Multivariate Calibration and Experimental Validation of a 3D Finite Element Thermal Model for Laser Powder Bed Fusion Metal Additive Manufacturing," *Integrating Materials and Manufacturing Innovation*, vol. 7, pp. 116–135, sep 2018.

[71] G. Tapia, S. Khairallah, M. Matthews, W. E. King, and A. Elwany, "Gaussian process-based surrogate modeling framework for process planning in laser powder-bed fusion additive manufacturing of 316L stainless steel," *International Journal of Advanced Manufacturing Technology*, vol. 94, no. 9-12, pp. 3591–3603, 2018.

[72] G. Tapia, W. King, L. Johnson, R. Arroyave, I. Karaman, and A. Elwany, "Uncertainty Propagation Analysis of Computational Models in Laser Powder Bed Fusion Additive Manufacturing Using Polynomial Chaos Expansions," *Journal of Manufacturing Science and Engineering*, vol. 140, dec 2018.

[73] L. Johnson, M. Mahmoudi, B. Zhang, R. Seede, X. Huang, J. T. Maier, H. J. Maier, I. Karaman, A. Elwany, and R. Arróyave, "Assessing printability maps in additive manufacturing of metal alloys," *Acta Materialia*, vol. 176, pp. 199–210, 2019.

[74] P. Nath, Z. Hu, and S. Mahadevan, "Uncertainty quantification of grain morphology in laser direct metal deposition," *Modelling and Simulation in Materials Science and Engineering*, vol. 27, no. 4, 2019.

[75] Z. Wang, P. Liu, Y. Ji, S. Mahadevan, M. F. Horstemeyer, Z. Hu, L. Chen, and L.-Q. Chen, "Uncertainty Quantification in Metallic Additive Manufacturing Through Physics-Informed Data-Driven Modeling," *JOM*, vol. 71, pp. 2625–2634, aug 2019.

[76] P. Honarmandi and R. Arróyave, "Uncertainty Quantification and Propagation in Computational Materials Science and Simulation-Assisted Materials Design," *Integrating Materials and Manufacturing Innovation*, vol. 9, pp. 103–143, mar 2020.

[77] Z. Wang, C. Jiang, P. Liu, W. Yang, Y. Zhao, M. F. Horstemeyer, L.-Q. Chen, Z. Hu, and L. Chen, "Uncertainty quantification and reduction in metal additive manufacturing," *npj Computational Materials*, vol. 6, p. 175, dec 2020.

[78] J. Ye, M. Mahmoudi, K. Karayagiz, L. Johnson, R. Seede, I. Karaman, R. Arroyave, and A. Elwany, "Bayesian Calibration of Multiple Coupled Simulation Models for Metal Additive Manufacturing: A Bayesian Network Approach," *ASCE-ASME J Risk and Uncert in Engrg Sys Part B Mech Engrg*, vol. 8, pp. 1–12, mar 2022.

[79] N. Kouraytem, X. Li, W. Tan, B. Kappes, and A. D. Spear, "Modeling process–structure–property relationships in metal additive manufacturing: a review on physics-driven versus data-driven approaches," *Journal of Physics: Materials*, vol. 4, p. 032002, jul 2021.

[80] Z. Wang, W. Yang, Q. Liu, Y. Zhao, P. Liu, D. Wu, M. Banu, and L. Chen, "Data-driven modeling of process, structure and property in additive manufacturing: A review and future directions," *Journal of Manufacturing Processes*, vol. 77, pp. 13–31, mar 2022.

[81] T. DebRoy, T. Mukherjee, H. L. Wei, J. W. Elmer, and J. O. Milewski, "Metallurgy, mechanistic models and machine learning in metal printing," *Nature Reviews Materials*, vol. 6, no. 1, pp. 48–68, 2021.

[82] C. Kamath and Y. J. Fan, "Regression with small data sets: a case study using code surrogates in additive manufacturing," *Knowledge and Information Systems*, vol. 57, no. 2, pp. 475–493, 2018.

[83] S. Mondal, D. Gwynn, A. Ray, and A. Basak, "Investigation of melt pool geometry control in additive manufacturing using hybrid modeling," *Metals*, vol. 10, no. 5, pp. 1–23, 2020.

[84] J. Gockel and J. Beuth, "Understanding Ti-6Al-4V microstructure control in additive manufacturing via process maps," *24th International SFF Symposium - An Additive Manufacturing Conference, SFF 2013*, pp. 666–674, 2013.

[85] B. Zhang, R. Seede, L. Xue, K. C. Atli, C. Zhang, A. Whitt, I. Karaman, R. Arroyave, and A. Elwany, "An efficient framework for printability assessment in Laser Powder Bed Fusion metal additive manufacturing," *Additive Manufacturing*, vol. 46, p. 102018, oct 2021.

[86] Z. Yan, W. Liu, Z. Tang, X. Liu, N. Zhang, M. Li, and H. Zhang, "Review on thermal analysis in laser-based additive manufacturing," *Optics and Laser Technology*, vol. 106, pp. 427–441, 2018.

[87] T. Eagar and N.-S. TSAI, "Temperature Fields Produced by Traveling Distributed Heat Sources Use of a Gaussian heat distribution in dimensionless form indicates final weld pool shape can be predicted accurately for many welds and materials," *Welding Journal (Miami, Fla)*, vol. 62, no. December, 1983.

[88] J. C. Steuben, A. J. Birnbaum, A. P. Iliopoulos, and J. G. Michopoulos, "Toward Feedback Control for Additive Manufacturing Processes Via Enriched Analytical Solutions," *Journal of Computing and Information Science in Engineering*, vol. 19, no. 3, 2019.

[89] J. C. Steuben, A. J. Birnbaum, J. G. Michopoulos, and A. P. Iliopoulos, "Enriched analytical solutions for additive manufacturing modeling and simulation," *Additive Manufacturing*, vol. 25, pp. 437–447, oct 2019.

[90] A. J. Wolfer, J. Aires, K. Wheeler, J. P. Delplanque, A. Rubenchik, A. Anderson, and S. Khairallah, "Fast solution strategy for transient heat conduction for arbitrary scan paths in additive manufacturing," *Additive Manufacturing*, vol. 30, p. 100898, oct 2019.

[91] Y. Yang, F. van Keulen, and C. Ayas, "A computationally efficient thermal model for selective laser melting," *Additive Manufacturing*, vol. 31, p. 100955, oct 2020.

[92] D. Weisz-Patrault, "Fast simulation of temperature and phase transitions in directed energy deposition additive manufacturing," *Additive Manufacturing*, vol. 31, p. 100990, jul 2020.

[93] I. A. Roberts, C. J. Wang, R. Esterlein, M. Stanford, and D. J. Mynors, "A three-dimensional finite element analysis of the temperature field during laser melting of metal powders in additive layer manufacturing," *International Journal of Machine Tools and Manufacture*, vol. 49, no. 12–13, pp. 916–923, 2009.

[94] A. Hussein, L. Hao, C. Yan, and R. Everson, "Finite element simulation of the temperature and stress fields in single layers built without-support in selective laser melting," *Materials and Design*, vol. 52, no. 0, pp. 638–647, 2013.

[95] L.-E. E. Loh, C.-K. K. Chua, W.-Y. Y. Yeong, J. Song, M. Mapar, S.-L. L. Sing, Z.-H. H. Liu, and D.-Q. Q. Zhang, "Numerical investigation and an effective modelling on the Selective Laser Melting (SLM) process with aluminium alloy 6061," *International Journal of Heat and Mass Transfer*, vol. 80, pp. 288–300, 2015.

[96] Y. Huang, L. J. Yang, X. Z. Du, and Y. P. Yang, "Finite element analysis of thermal behavior of metal powder during selective laser melting," *International Journal of Thermal Sciences*, vol. 104, pp. 146–157, 2016.

[97] E. R. Denlinger, M. Gouge, J. Irwin, and P. Michaleris, "Thermomechanical model development and in situ experimental validation of the Laser Powder-Bed Fusion process," *Additive Manufacturing*, vol. 16, pp. 73–80, 2017.

[98] T. Heeling, M. Cloots, and K. Wegener, "Melt pool simulation for the evaluation of process parameters in selective laser melting," *Additive Manufacturing*, vol. 14, pp. 116–125, 2017.

[99] J. Liu, B. Jalalahmadi, Y. B. Guo, M. P. Sealy, and N. Bolander, "A review of computational modeling in powder-based additive manufacturing for metallic part qualification," *Rapid Prototyping Journal*, vol. 24, no. 8, pp. 1245–1264, 2018.

[100] S. A. Khairallah and A. Anderson, "Mesoscopic simulation model of selective laser melting of stainless steel powder," *Journal of Materials Processing Technology*, vol. 214, no. 11, pp. 2627–2636, 2014.

[101] R. Ganeriwala and T. I. Zohdi, "A coupled discrete element-finite difference model of selective laser sintering," *Granular Matter*, vol. 18, no. 2, pp. 1–15, 2016.

[102] S. A. Khairallah, A. T. Anderson, A. M. Rubenchik, and W. E. King, "Laser powder-bed fusion additive manufacturing: Physics of complex melt flow and formation mechanisms of pores, spatter, and denudation zones," *Acta Materialia*, vol. 108, pp. 36–45, apr 2016.

[103] J. C. Steuben, A. P. Iliopoulos, and J. G. Michopoulos, "Discrete element modeling of particle-based additive manufacturing processes," *Computer Methods in Applied Mechanics and Engineering*, vol. 305, pp. 537–561, 2016.

[104] C. Panwisawas, C. Qiu, M. J. Anderson, Y. Sovani, R. P. Turner, M. M. Attallah, J. W. Brooks, and H. C. Basoalto, "Mesoscale modelling of selective laser melting: Thermal fluid dynamics and microstructural evolution," *Computational Materials Science*, vol. 126, pp. 479–490, 2017.

[105] W. Pei, W. Zhengying, C. Zhen, L. Junfeng, Z. Shuzhe, and D. Jun, "Numerical simulation and parametric analysis of selective laser melting process of AlSi10Mg powder," *Applied Physics A: Materials Science and Processing*, vol. 123, no. 8, pp. 1–15, 2017.

[106] M. Xia, D. Gu, G. Yu, D. Dai, H. Chen, and Q. Shi, "Porosity evolution and its thermodynamic mechanism of randomly packed powder-bed during selective laser melting of Inconel 718 alloy," *International Journal of Machine Tools and Manufacture*, vol. 116, pp. 96–106, jan 2017.

[107] M. Kennedy, "Predicting the output from a complex computer code when fast approximations are available," *Biometrika*, vol. 87, pp. 1–13, mar 2000.

[108] D. Higdon, M. Kennedy, J. C. Cavendish, J. A. Cafeo, and R. D. Ryne, "Combining Field Data and Computer Simulations for Calibration and Prediction," *SIAM Journal on Scientific Computing*, vol. 26, pp. 448–466, jan 2004.

[109] D. Higdon, J. Gattiker, B. Williams, and M. Rightley, "Computer Model Calibration Using High-Dimensional Output," *Journal of the American Statistical Association*, vol. 103, pp. 570–583, jun 2008.

[110] R. Seede, D. Shoukr, B. Zhang, A. Whitt, S. Gibbons, P. Flater, A. Elwany, R. Arroyave, and I. Karaman, "An ultra-high strength martensitic steel fabricated using selective laser melting additive manufacturing: Densification, microstructure, and mechanical properties," *Acta Materialia*, vol. 186, pp. 199–214, mar 2020.

[111] G. Tapia, W. E. King, R. Arroyave, L. Johnson, I. Karaman, and A. Elwany, "Validation of a Laser-Based Powder Bed Fusion thermal model via Uncertainty Propagation and generalized Polynomial Chaos Expansions," *Journal of Manufacturing Science and Engineering*, vol. 140, dec 2018.

[112] P. Honarmandi, R. Seede, L. Xue, D. Shoukr, P. Morcos, B. Zhang, C. Zhang, A. Elwany, I. Karaman, and R. Arroyave, "A rigorous test and improvement of the Eagar-Tsai model for melt pool characteristics in laser powder bed fusion additive manufacturing," *Additive Manufacturing*, vol. 47, no. August, p. 102300, 2021.

[113] J. G. Michopoulos, J. C. Steuben, A. J. Birnbaum, A. P. Iliopoulos, J. Aroh, A. D. Rollett, and B. Gould, "Morphological Analysis of 316L Laser Powder Bed Fusion Melt-Pool via the Enriched Analytical Solution Method," in *Volume 9: 40th Computers and Information in Engineering Conference (CIE)*, pp. 1–14, American Society of Mechanical Engineers, aug 2020.

[114] COMSOL AB, "Comsol multiphysics® v5.6." `www.comsol.com`. Stockholm, Sweden.

[115] The Mathworks Inc., "Matlab® v2021b." `www.mathworks.com`. Natick, Massachusetts , USA.

[116] A. L. K. Rawlings, A. J. Birnbaum, J. G. Michopoulos, J. C. Steuben, A. P. Iliopoulos, and H. Ryou, "Simulation Informed Effects of Solidification Rate on 316L Single Tracks

Produced by Selective Laser Melting," in *Volume 9: 40th Computers and Information in Engineering Conference (CIE)*, American Society of Mechanical Engineers, aug 2020.

[117] L. Le Gratiet and J. Garnier, "RECURSIVE CO-KRIGING MODEL FOR DESIGN OF COMPUTER EXPERIMENTS WITH MULTIPLE LEVELS OF FIDELITY," *International Journal for Uncertainty Quantification*, vol. 4, no. 5, pp. 365–386, 2014.

[118] L. Le Gratiet and C. Cannamela, "Cokriging-Based Sequential Design Strategies Using Fast Cross-Validation Techniques for Multi-Fidelity Computer Codes," *Technometrics*, vol. 57, pp. 418–427, jul 2015.

[119] P. Perdikaris, M. Raissi, A. Damianou, N. D. Lawrence, and G. E. Karniadakis, "Nonlinear information fusion algorithms for data-efficient multi-fidelity modelling," *Proceedings of the Royal Society A: Mathematical, Physical and Engineering Sciences*, vol. 473, no. 2198, 2017.

[120] C. E. Rasmussen and C. K. I. Williams, *Gaussian Processes for Machine Learning*. The MIT Press, 2006.

[121] C. Williams and D. Barber, "Bayesian classification with Gaussian processes," *IEEE Transactions on Pattern Analysis and Machine Intelligence*, vol. 20, no. 12, pp. 1342–1351, 1998.

[122] F. Sahli Costabal, P. Perdikaris, E. Kuhl, and D. E. Hurtado, "Multi-fidelity classification using Gaussian processes: Accelerating the prediction of large-scale computational models," *Computer Methods in Applied Mechanics and Engineering*, vol. 357, p. 112602, 2019.

[123] N. Klyuchnikov and E. Burnaev, "Gaussian process classification for variable fidelity data," *Neurocomputing*, vol. 397, pp. 345–355, 2020.

[124] P. Z. Qian, "Nested Latin hypercube designs," *Biometrika*, vol. 96, no. 4, pp. 957–970, 2009.

[125] X. He and P. Z. Qian, "Nested orthogonal array-based Latin hypercube designs," *Biometrika*, vol. 98, no. 3, pp. 721–731, 2011.

[126] J. Xu, X. Duan, Z. Wang, and L. Yan, "A general construction for nested Latin hypercube designs," *Statistics and Probability Letters*, vol. 134, no. 11771450, pp. 134–140, 2018.

[127] S. Dash, B. N. Mandal, and R. Parsad, "On the construction of nested orthogonal Latin hypercube designs," *Metrika*, vol. 83, no. 3, pp. 347–353, 2020.

[128] A. Paleyes, M. Pullin, M. Mahsereci, N. Lawrence, and J. González, "Emulation of physical processes with Emukit," in *Second Workshop on Machine Learning and the Physical Sciences, NeurIPS*, 2019.

[129] J. A. Cherry, H. M. Davies, S. Mehmood, N. P. Lavery, S. G. R. Brown, and J. Sienz, "Investigation into the effect of process parameters on microstructural and physical properties of 316L stainless steel parts by selective laser melting," *International Journal of Advanced Manufacturing Technology*, vol. 76, no. 5-8, pp. 869–879, 2014.

[130] E. Popova, T. M. Rodgers, X. Gong, A. Cecen, J. D. Madison, and S. R. Kalidindi, "Process-Structure Linkages Using a Data Science Approach: Application to Simulated Additive Manufacturing Data," *Integrating Materials and Manufacturing Innovation*, vol. 6, pp. 54–68, mar 2017.

[131] A. Batabyal, S. Sagar, J. Zhang, T. Dube, X. Yang, and J. Zhang, "Gaussian Process-Based Model to Optimize Additively Manufactured Powder Microstructures From Phase Field Modeling," *ASCE-ASME Journal of Risk and Uncertainty in Engineering Systems Part B Mechanical Engineering*, vol. 8, mar 2022.

[132] M. A. Groeber, M. D. Uchic, D. M. Dimiduk, Y. Bhandari, and S. Ghosh, "A framework for automated 3D microstructure analysis & representation," *Journal of Computer-Aided Materials Design*, vol. 14, no. SUPPL. 1, pp. 63–74, 2007.

[133] M. Groeber, S. Ghosh, M. D. Uchic, and D. M. Dimiduk, "A framework for automated analysis and simulation of 3D polycrystalline microstructures. Part 1: Statistical characterization," *Acta Materialia*, vol. 56, no. 6, pp. 1257–1273, 2008.

[134] M. Groeber, S. Ghosh, M. D. Uchic, and D. M. Dimiduk, "A framework for automated analysis and simulation of 3D polycrystalline microstructures. Part 2: Synthetic structure generation," *Acta Materialia*, vol. 56, no. 6, pp. 1274–1287, 2008.

[135] M. A. Groeber and M. A. Jackson, "DREAM.3D: A Digital Representation Environment for the Analysis of Microstructure in 3D," *Integrating Materials and Manufacturing Innovation*, vol. 3, no. 1, p. 5, 2014.

[136] D. M. Turner and S. R. Kalidindi, "Statistical construction of 3-D microstructures from 2-D exemplars collected on oblique sections," *Acta Materialia*, vol. 102, pp. 136–148, 2016.

[137] D. T. Fullwood, S. R. Kalidindi, S. R. Niezgoda, A. Fast, and N. Hampson, "Gradient-based microstructure reconstructions from distributions using fast Fourier transforms," *Materials Science and Engineering A*, vol. 494, no. 1-2, pp. 68–72, 2008.

[138] D. T. Fullwood, S. R. Niezgoda, and S. R. Kalidindi, "Microstructure reconstructions from 2-point statistics using phase-recovery algorithms," *Acta Materialia*, vol. 56, pp. 942–948, mar 2008.

[139] S. R. Niezgoda, D. M. Turner, D. T. Fullwood, and S. R. Kalidindi, "Optimized structure based representative volume element sets reflecting the ensemble-averaged 2-point statistics," *Acta Materialia*, vol. 58, no. 13, pp. 4432–4445, 2010.

[140] S. R. Niezgoda, Y. C. Yabansu, and S. R. Kalidindi, "Understanding and visualizing microstructure and microstructure variance as a stochastic process," *Acta Materialia*, vol. 59, no. 16, pp. 6387–6400, 2011.

[141] S. R. Kalidindi, S. R. Niezgoda, and A. A. Salem, "Microstructure informatics using higher-order statistics and efficient data-mining protocols," *Jom*, vol. 63, no. 4, pp. 34–41, 2011.

[142] T. Fast, O. Wodo, B. Ganapathysubramanian, and S. R. Kalidindi, "Microstructure taxonomy based on spatial correlations: Application to microstructure coarsening," *Acta Materialia*, vol. 108, pp. 176–185, 2016.

[143] A. Choudhury, Y. C. Yabansu, S. R. Kalidindi, and A. Dennstedt, "Quantification and classification of microstructures in ternary eutectic alloys using 2-point spatial correlations and principal component analyses," *Acta Materialia*, vol. 110, pp. 131–141, 2016.

[144] S. Bargmann, B. Klusemann, J. Markmann, J. E. Schnabel, K. Schneider, C. Soyarslan, and J. Wilmers, "Generation of 3D representative volume elements for heterogeneous materials: A review," *Progress in Materials Science*, vol. 96, pp. 322–384, jul 2018.

[145] D. R. Gunasegaram and I. Steinbach, "Modelling of Microstructure Formation in Metal Additive Manufacturing: Recent Progress, Research Gaps and Perspectives," *Metals*, vol. 11, p. 1425, sep 2021.

[146] R. Quey, P. Dawson, and F. Barbe, "Large-scale 3D random polycrystals for the finite element method: Generation, meshing and remeshing," *Computer Methods in Applied Mechanics and Engineering*, vol. 200, pp. 1729–1745, apr 2011.

[147] R. Quey and L. Renversade, "Optimal polyhedral description of 3D polycrystals: Method and application to statistical and synchrotron X-ray diffraction data," *Computer Methods in Applied Mechanics and Engineering*, vol. 330, pp. 308–333, mar 2018.

[148] T. M. Rodgers, J. D. Madison, and V. Tikare, "Simulation of metal additive manufacturing microstructures using kinetic Monte Carlo," *Computational Materials Science*, vol. 135, pp. 78–89, jul 2017.

[149] W. Li and M. Soshi, "Modeling analysis of the effect of laser transverse speed on grain morphology during directed energy deposition process," *The International Journal of Advanced Manufacturing Technology*, vol. 103, pp. 3279–3291, aug 2019.

[150] Z. Zhang, X. X. Yao, and P. Ge, "Phase-field-model-based analysis of the effects of powder particle on porosities and densities in selective laser sintering additive manufacturing," *International Journal of Mechanical Sciences*, vol. 166, jul 2020.

[151] T. Keller, G. Lindwall, S. Ghosh, L. Ma, B. M. Lane, F. Zhang, U. R. Kattner, E. A. Lass, J. C. Heigel, Y. Idell, M. E. Williams, A. J. Allen, J. E. Guyer, and L. E. Levine, "Application

of finite element, phase-field, and CALPHAD-based methods to additive manufacturing of Ni-based superalloys," *Acta Materialia*, vol. 139, pp. 244–253, 2017.

[152] L. X. Lu, N. Sridhar, and Y. W. Zhang, "Phase field simulation of powder bed-based additive manufacturing," *Acta Materialia*, vol. 144, pp. 801–809, 2018.

[153] K. Karayagiz, L. Johnson, R. Seede, V. Attari, B. Zhang, X. Huang, S. Ghosh, T. Duong, I. Karaman, A. Elwany, and R. Arróyave, "Finite interface dissipation phase field modeling of Ni–Nb under additive manufacturing conditions," *Acta Materialia*, vol. 185, pp. 320–339, feb 2020.

[154] V. Attari, P. Honarmandi, T. Duong, D. J. Sauceda, D. Allaire, and R. Arroyave, "Uncertainty propagation in a multiscale CALPHAD-reinforced elastochemical phase-field model," *Acta Materialia*, vol. 183, pp. 452–470, 2020.

[155] O. Zinovieva, A. Zinoviev, V. Ploshikhin, V. Romanova, and R. Balokhonov, "Strategy of computational predictions for mechanical behaviour of additively manufactured materials," *Materials Science and Technology*, vol. 34, pp. 1591–1605, sep 2018.

[156] Y. Lian, S. Lin, W. Yan, W. K. Liu, and G. J. Wagner, "A parallelized three-dimensional cellular automaton model for grain growth during additive manufacturing," *Computational Mechanics*, vol. 61, pp. 543–558, may 2018.

[157] K. Teferra and D. J. Rowenhorst, "Optimizing the cellular automata finite element model for additive manufacturing to simulate large microstructures," *Acta Materialia*, p. 116930, apr 2021.

[158] J. Lee, N. H. Goo, W. B. Park, M. Pyo, and K. Sohn, "Virtual microstructure design for steels using generative adversarial networks," *Engineering Reports*, vol. 3, pp. 1–14, jan 2021.

[159] A. Sciazko, Y. Komatsu, and N. Shikazono, "Unsupervised Generative Adversarial Network for 3-D Microstructure Synthesis from 2-D Image," *ECS Meeting Abstracts*, vol. MA2021-03, pp. 55–55, jul 2021.

[160] T. Hsu, W. K. Epting, H. Kim, H. W. Abernathy, G. A. Hackett, A. D. Rollett, P. A. Salvador, and E. A. Holm, "Microstructure Generation via Generative Adversarial Network for Heterogeneous, Topologically Complex 3D Materials," *JOM*, vol. 73, pp. 90–102, jan 2021.

[161] M. A. Álvarez, L. Rosasco, and N. D. Lawrence, "Kernels for Vector-Valued Functions: A Review," *Foundations and Trends® in Machine Learning*, vol. 4, no. 3, pp. 195–266, 2012.

[162] F. Roters, P. Eisenlohr, L. Hantcherli, D. Tjahjanto, T. Bieler, and D. Raabe, "Overview of constitutive laws, kinematics, homogenization and multiscale methods in crystal plasticity finite-element modeling: Theory, experiments, applications," *Acta Materialia*, vol. 58, pp. 1152–1211, feb 2010.

[163] J. Segurado, R. A. Lebensohn, and J. LLorca, "Computational Homogenization of Polycrystals," in *Advances in Applied Mechanics*, pp. 1–114, 2018.

[164] L. Thijs, K. Kempen, J.-P. P. Kruth, and J. Van Humbeeck, "Fine-structured aluminium products with controllable texture by selective laser melting of pre-alloyed AlSi10Mg powder," *Acta Materialia*, vol. 61, no. 5, pp. 1809–1819, 2013.

[165] T. Niendorf, S. Leuders, A. Riemer, H. A. Richard, T. Tröster, and D. Schwarze, "Highly anisotropic steel processed by selective laser melting," *Metallurgical and Materials Transactions B*, vol. 44, no. 4, pp. 794–796, 2013.

[166] A. Riemer, S. Leuders, M. Thöne, H. A. Richard, T. Tröster, and T. Niendorf, "On the fatigue crack growth behavior in 316L stainless steel manufactured by selective laser melting," *Engineering Fracture Mechanics*, vol. 120, pp. 15–25, 2014.

[167] T. Niendorf, F. Brenne, and M. Schaper, "Lattice structures manufactured by SLM: on the effect of geometrical dimensions on microstructure evolution during processing," *Metallurgical and materials transactions B*, vol. 45, no. 4, pp. 1181–1185, 2014.

[168] H. L. Wei, J. Mazumder, and T. DebRoy, "Evolution of solidification texture during additive manufacturing," *Scientific Reports*, vol. 5, p. 16446, 2015.

[169] G. P. Dinda, A. K. Dasgupta, and J. Mazumder, "Texture control during laser deposition of nickel-based superalloy," *Scripta Materialia*, vol. 67, no. 5, pp. 503–506, 2012.

[170] I. Yadroitsev, P. Krakhmalev, I. Yadroitsava, S. Johansson, and I. Smurov, "Energy input effect on morphology and microstructure of selective laser melting single track from metallic powder," *Journal of Materials Processing Technology*, vol. 213, no. 4, pp. 606–613, 2013.

[171] K. Saeidi, X. Gao, Y. Zhong, and Z. J. Shen, "Hardened austenite steel with columnar subgrain structure formed by laser melting," *Mater. Sci. Eng. A*, vol. 625, pp. 221–229, 2015.

[172] P. A. Kobryn and S. L. Semiatin, "The laser additive manufacture of Ti-6Al-4V," *JOM*, vol. 53, no. 9, pp. 40–42, 2001.

[173] A. J. Birnbaum, J. C. Steuben, E. J. Barrick, A. P. Iliopoulos, and J. G. Michopoulos, "Intrinsic strain aging, $\Sigma 3$ boundaries, and origins of cellular substructure in additively manufactured 316L," *Additive Manufacturing*, vol. 29, p. 100784, oct 2019.

[174] S. Kou, *Welding Metallurgy*. Hoboken, New Jersey: John Wiley & Sons, 2nd ed., 2002.

[175] L. Hitzler, J. Hirsch, B. Heine, M. Merkel, W. Hall, and A. Öchsner, "On the anisotropic mechanical properties of selective laser-melted stainless steel," *Materials*, vol. 10, no. 10, p. 1136, 2017.

[176] J. J. Lewandowski and M. Seifi, "Metal additive manufacturing: a review of mechanical properties," *Annual Review of Materials Research*, vol. 46, no. 1, pp. 151–186, 2016.

[177] M. Seifi, M. Gorelik, J. Waller, N. Hrabe, N. Shamsaei, S. Daniewicz, and J. J. Lewandowski, "Progress Towards Metal Additive Manufacturing Standardization to Support Qualification and Certification," *Jom*, vol. 69, no. 3, pp. 439–455, 2017.

[178] T. R. Smith, J. D. Sugar, C. San Marchi, and J. M. Schoenung, "Strengthening mechanisms in directed energy deposited austenitic stainless steel," *Acta Materialia*, vol. 164, pp. 728–740, 2019.

[179] K. L. Johnson, T. M. Rodgers, O. D. Underwood, J. D. Madison, K. R. Ford, S. R. Whetten, D. J. Dagel, and J. E. Bishop, "Simulation and experimental comparison of the thermomechanical history and 3D microstructure evolution of 304L stainless steel tubes manufactured using LENS," *Computational Mechanics*, vol. 61, no. 5, pp. 559–574, 2018.

[180] W. Yan, S. Lin, O. L. Kafka, C. Yu, Z. Liu, Y. Lian, S. Wolff, J. Cao, G. J. Wagner, and W. K. Liu, "Modeling process-structure-property relationships for additive manufacturing," *Frontiers of Mechanical Engineering*, vol. 13, no. 4, pp. 482–492, 2018.

[181] A. Ahmadi, R. Mirzaeifar, N. S. Moghaddam, A. S. Turabi, H. E. Karaca, and M. Elahinia, "Effect of manufacturing parameters on mechanical properties of 316L stainless steel parts fabricated by selective laser melting: A computational framework," *Materials & Design*, vol. 112, pp. 328–338, 2016.

[182] R. Saunders, A. Achuthan, A. Iliopoulos, J. Michopoulos, and A. Bagchi, "Influence of grain size and shape on mechanical properties of metal Am materials," in *Proc. 29th Annual Int. Solid Freeform Fabrication Symp.—An Additive Manufacturing Conf*, 2018.

[183] C. Herriott, X. Li, N. Kouraytem, V. Tari, W. Tan, B. Anglin, A. D. Rollett, and A. D. Spear, "A multi-scale, multi-physics modeling framework to predict spatial variation of properties in additive-manufactured metals," *Modelling and Simulation in Materials Science and Engineering*, vol. 27, no. 2, p. 25009, 2019.

[184] T. M. Rodgers, H. Lim, and J. A. Brown, "Three-Dimensional Additively Manufactured Microstructures and Their Mechanical Properties," *JOM*, vol. 72, pp. 75–82, jan 2020.

[185] R. E. Jones, J. A. Templeton, C. M. Sanders, and J. T. Ostien, "Machine Learning Models of Plastic Flow Based on Representation Theory," *Computer Modeling in Engineering & Sciences*, vol. 117, pp. 309–342, dec 2018.

[186] K. Wang, W. Sun, and Q. Du, "A cooperative game for automated learning of elasto-plasticity knowledge graphs and models with AI-guided experimentation," *Computational Mechanics*, vol. 64, pp. 467–499, aug 2019.

[187] K. Wang and W. Sun, "Meta-modeling game for deriving theory-consistent, microstructure-based traction–separation laws via deep reinforcement learning," *Computer Methods in Applied Mechanics and Engineering*, vol. 346, pp. 216–241, apr 2019.

[188] J. Jung, J. I. Yoon, H. K. Park, J. Y. Kim, and H. S. Kim, "An efficient machine learning approach to establish structure-property linkages," *Computational Materials Science*, vol. 156, pp. 17–25, jan 2019.

[189] J. Jung, J. I. Yoon, H. K. Park, J. Y. Kim, and H. S. Kim, "Bayesian approach in predicting mechanical properties of materials: Application to dual phase steels," *Materials Science and Engineering: A*, vol. 743, pp. 382–390, jan 2019.

[190] D. Reimann, K. Nidadavolu, H. ul Hassan, N. Vajragupta, T. Glasmachers, P. Junker, and A. Hartmaier, "Modeling Macroscopic Material Behavior With Machine Learning Algorithms Trained by Micromechanical Simulations," *Frontiers in Materials*, vol. 6, pp. 3513–3520, aug 2019.

[191] G. Whelan and D. L. McDowell, "Machine Learning-Enabled Uncertainty Quantification for Modeling Structure–Property Linkages for Fatigue Critical Engineering Alloys Using an ICME Workflow," *Integrating Materials and Manufacturing Innovation*, vol. 9, pp. 376–393, dec 2020.

[192] Z. Liu and C. Wu, "Exploring the 3D architectures of deep material network in data-driven multiscale mechanics," *Journal of the Mechanics and Physics of Solids*, vol. 127, pp. 20–46, jun 2019.

[193] A. Frankel, K. Tachida, and R. Jones, "Prediction of the evolution of the stress field of polycrystals undergoing elastic-plastic deformation with a hybrid neural network model," *Machine Learning: Science and Technology*, vol. 1, p. 035005, jul 2020.

[194] A. Frankel, R. Jones, C. Alleman, and J. Templeton, "Predicting the mechanical response of oligocrystals with deep learning," *Computational Materials Science*, vol. 169, p. 109099, nov 2019.

[195] J. S. Morris, "Functional Regression," *Annual Review of Statistics and Its Application*, vol. 2, pp. 321–359, apr 2015.

[196] J. O. Ramsay and B. W. Silverman, *Functional Data Analysis*. Springer Series in Statistics, New York, NY: Springer New York, second edition ed., 2005.

[197] F. Ferraty and P. Vieu, *Nonparametric Functional Data Analysis*. Springer Series in Statistics, Springer New York, 2006.

[198] N. Ling and P. Vieu, "Nonparametric modelling for functional data: selected survey and tracks for future," *Statistics*, vol. 52, pp. 934–949, jul 2018.

[199] M. D. Morris, "Gaussian Surrogates for Computer Models With Time-Varying Inputs and Outputs," *Technometrics*, vol. 54, pp. 42–50, feb 2012.

[200] X. Tang, Z. Hong, Y. Hu, and H. Lian, "Gaussian Process Models for Non Parametric Functional Regression with Functional Responses," *Communications in Statistics - Theory and Methods*, vol. 44, pp. 3428–3445, aug 2015.

[201] V. Poynor and S. Munch, "Combining functional data with hierarchical Gaussian process models," *Environmental and Ecological Statistics*, vol. 24, pp. 175–199, jun 2017.

[202] J. Yang, D. D. Cox, J. S. Lee, P. Ren, and T. Choi, "Efficient Bayesian hierarchical functional data analysis with basis function approximations using Gaussian–Wishart processes," *Biometrics*, vol. 73, pp. 1082–1091, dec 2017.

[203] L. Luo, Y. Yao, F. Gao, and C. Zhao, "Mixed-effects Gaussian process modeling approach with application in injection molding processes," *Journal of Process Control*, vol. 62, pp. 37–43, feb 2018.

[204] J. Betancourt, F. Bachoc, T. Klein, D. Idier, R. Pedreros, and J. Rohmer, "Gaussian process metamodeling of functional-input code for coastal flood hazard assessment," *Reliability Engineering & System Safety*, vol. 198, p. 106870, jun 2020.

[205] J. Li, R. Jin, and H. Z. Yu, "Integration of physically-based and data-driven approaches for thermal field prediction in additive manufacturing," *Materials & Design*, vol. 139, pp. 473–485, feb 2018.

[206] B. Wang and A. Xu, "Gaussian process methods for nonparametric functional regression with mixed predictors," *Computational Statistics & Data Analysis*, vol. 131, pp. 80–90, mar 2019.

[207] S. Conti and A. O'Hagan, "Bayesian emulation of complex multi-output and dynamic computer models," *Journal of Statistical Planning and Inference*, vol. 140, pp. 640–651, mar 2010.

[208] A. I. Forrester, A. Sóbester, and A. J. Keane, "Multi-fidelity optimization via surrogate modelling," *Proceedings of the Royal Society A: Mathematical, Physical and Engineering Sciences*, vol. 463, pp. 3251–3269, dec 2007.

[209] R. N. Saunders, A. Achuthan, A. P. Iliopoulos, J. G. Michopoulos, and A. Bagchi, "Effects of the Microstructural Grain Size and Aspect Ratio on the Mechanical Properties of Additively Manufactured Parts via Computational Analysis," *Defense Technical Information Center*, no. NRL/FR/6353–20-10,411, 2020.

[210] D. Fan and L.-Q. Chen, "Computer simulation of grain growth using a continuum field model," *Acta Materialia*, vol. 45, no. 2, pp. 611–622, 1997.

[211] J. G. Michopoulos, A. P. Iliopoulos, J. C. Steuben, A. J. Birnbaum, Y. Fu, and J.-H. Song, "Towards Computational Synthesis of Microstructural Crystalline Morphologies for Additive Manufacturing Applications," in *Volume 1: 37th Computers and Information in Engineering Conference*, pp. V001T02A030–V001T02A030, American Society of Mechanical Engineers, American Society of Mechanical Engineers, aug 2017.

[212] C. E. Rasmussen and C. K. I. Williams, "Regression," in *Gaussian Processes for Machine Learning*, The MIT Press, 2005.

[213] A. Mangal and E. A. Holm, "Applied machine learning to predict stress hotspots I: Face centered cubic materials," *International Journal of Plasticity*, vol. 111, pp. 122–134, dec 2018.

[214] R. Bostanabad, Y. Zhang, X. Li, T. Kearney, L. C. Brinson, D. W. Apley, W. K. Liu, and W. Chen, "Computational microstructure characterization and reconstruction: Review of the state-of-the-art techniques," *Progress in Materials Science*, vol. 95, pp. 1–41, jun 2018.

[215] A. Achuthan, A. P. Iliopoulos, J. G. Michopoulos, R. Saunders, and A. Bagchi, "Towards a Constitutive Model That Encapsulates Microstructural Features Induced by Powder Additive Manufacturing," in *Volume 1: 37th Computers and Information in Engineering Conference*, vol. 1, pp. 1–11, American Society of Mechanical Engineers, American Society of Mechanical Engineers, aug 2017.

[216] S. M. Qidwai, D. M. Turner, S. R. Niezgoda, A. C. Lewis, A. B. Geltmacher, D. J. Rowenhorst, and S. R. Kalidindi, "Estimating the response of polycrystalline materials using sets of weighted statistical volume elements," *Acta Materialia*, vol. 60, pp. 5284–5299, aug 2012.

[217] M. Knezevic, H. F. Al-Harbi, and S. R. Kalidindi, "Crystal plasticity simulations using discrete Fourier transforms," *Acta Materialia*, vol. 57, pp. 1777–1784, apr 2009.

[218] F. Roters, M. Diehl, P. Shanthraj, P. Eisenlohr, C. Reuber, S. Wong, T. Maiti, A. Ebrahimi, T. Hochrainer, H.-O. Fabritius, S. Nikolov, M. Friák, N. Fujita, N. Grilli, K. Janssens, N. Jia, P. Kok, D. Ma, F. Meier, E. Werner, M. Stricker, D. Weygand, and D. Raabe, "DAMASK – The Düsseldorf Advanced Material Simulation Kit for modeling multi-physics crystal plasticity, thermal, and damage phenomena from the single crystal up to the component scale," *Computational Materials Science*, vol. 158, pp. 420–478, feb 2019.

[219] M. Taheri Andani, M. R. Karamooz-Ravari, R. Mirzaeifar, and J. Ni, "Micromechanics modeling of metallic alloys 3D printed by selective laser melting," *Materials & Design*, vol. 137, pp. 204–213, jan 2018.

[220] M. Taheri Andani, M. Ghodrati, M. R. Karamooz-Ravari, R. Mirzaeifar, and J. Ni, "Damage modeling of metallic alloys made by additive manufacturing," *Materials Science and Engineering: A*, vol. 743, pp. 656–664, jan 2019.

[221] M. Titsias, "Variational Learning of Inducing Variables in Sparse Gaussian Processes," in *Proceedings of the Twelth International Conference on Artificial Intelligence and Statistics* (D. van Dyk and M. Welling, eds.), vol. 5 of *Proceedings of Machine Learning Research*, (Hilton Clearwater Beach Resort, Clearwater Beach, Florida USA), pp. 567–574, PMLR, 2009.

[222] J. Hensman, N. Fusi, and N. D. Lawrence, "Gaussian Processes for Big Data," in *Proceedings of the Twenty-Ninth Conference on Uncertainty in Artificial Intelligence*, (Bellevue, WA), pp. 282–290, sep 2013.

[223] J. Steuben, J. Michopoulos, A. Iliopoulos, and C. Turner, "Inverse characterization of composite materials via surrogate modeling," *Composite Structures*, vol. 132, pp. 694–708, nov 2015.

[224] T. Zhou, E. L. Droguett, and A. Mosleh, "Physics-Informed Deep Learning: A Promising Technique for System Reliability Assessment," *arXiv*, pp. 1–29, 2021.

[225] A. Y. Sun, H. Yoon, C.-Y. Shih, and Z. Zhong, "Applications of physics-informed scientific machine learning in subsurface science: A survey," pp. 1–20, 2021.

[226] B. Lütjens, C. H. Crawford, M. Veillette, and D. Newman, "PCE-PINNs: Physics-Informed Neural Networks for Uncertainty Propagation in Ocean Modeling," pp. 1–7, 2021.

[227] E. Haghighat and R. Juanes, "SciANN: A Keras/TensorFlow wrapper for scientific computations and physics-informed deep learning using artificial neural networks," *Computer Methods in Applied Mechanics and Engineering*, vol. 373, p. 113552, 2021.

[228] E. Haghighat, M. Raissi, A. Moure, H. Gomez, and R. Juanes, "A physics-informed deep learning framework for inversion and surrogate modeling in solid mechanics," *Computer Methods in Applied Mechanics and Engineering*, vol. 379, p. 113741, 2021.

[229] G. E. Karniadakis, I. G. Kevrekidis, L. Lu, P. Perdikaris, S. Wang, and L. Yang, "Physics-informed machine learning," *Nature Reviews Physics*, vol. 3, no. 6, pp. 422–440, 2021.

[230] M. Vohra, P. Nath, S. Mahadevan, and Y.-T. Tina Lee, "Fast surrogate modeling using dimensionality reduction in model inputs and field output: Application to additive manufacturing," *Reliability Engineering & System Safety*, vol. 201, p. 106986, sep 2020.

[231] G. Teichert, A. Natarajan, A. Van der Ven, and K. Garikipati, "Machine learning materials physics: Integrable deep neural networks enable scale bridging by learning free energy functions," *Computer Methods in Applied Mechanics and Engineering*, vol. 353, pp. 201–216, aug 2019.

[232] L. Yang, M. Prabhat, G. Karniadakis, S. Treichler, T. Kurth, K. Fischer, D. Barajas-Solano, J. Romero, V. Churavy, A. Tartakovsky, and M. Houston, "Highly-scalable, Physics-Informed GANs for Learning Solutions of Stochastic PDEs," in *2019 IEEE/ACM Third Workshop on Deep Learning on Supercomputers (DLS)*, vol. 42, pp. 1–11, IEEE, nov 2019.

[233] N. Geneva and N. Zabaras, "Multi-fidelity generative deep learning turbulent flows," *Foundations of Data Science*, vol. 2, pp. 391–428, jun 2020.

[234] B. Lütjens, B. Leshchinskiy, C. Requena-Mesa, F. Chishtie, N. Díaz-Rodriguez, O. Boulais, A. Piña, D. Newman, A. Lavin, Y. Gal, and C. Raïssi, "Physics-informed GANs for Coastal Flood Visualization," pp. 1–10, 2020.

[235] L. Yang, C. Daskalakis, and G. E. Karniadakis, "Generative Ensemble Regression: Learning Particle Dynamics from Observations of Ensembles with Physics-Informed Deep Generative Models," pp. 1–35, 2020.

[236] L. Yang, D. Zhang, and G. E. Karniadakis, "Physics-Informed Generative Adversarial Networks for Stochastic Differential Equations," *SIAM Journal on Scientific Computing*, vol. 42, pp. A292–A317, jan 2020.

[237] A. Daw, M. Maruf, and A. Karpatne, *PID-GAN: A GAN Framework based on a Physics-informed Discriminator for Uncertainty Quantification with Physics*, vol. 1. Association for Computing Machinery, 2021.

[238] L. Liu, C. Zhang, and D. Tao, "GAN-MDF: A Method for Multi-fidelity Data Fusion in Digital Twins," pp. 1–23, 2021.

[239] B. Lütjens, B. Leshchinskiy, C. Requena-Mesa, F. Chishtie, N. Díaz-Rodríguez, O. Boulais, A. Sankaranarayanan, A. Piña, Y. Gal, C. Raïssi, A. Lavin, and D. Newman, "Physically-Consistent Generative Adversarial Networks for Coastal Flood Visualization," pp. 1–11, 2021.

[240] A. Mishra and T. Pathak, "Deep Convolutional Generative Modeling for Artificial Microstructure Development of Aluminum-Silicon Alloy," *Indian Journal of Data Mining*, vol. 1, pp. 1–6, may 2021.

[241] S. Kench and S. J. Cooper, "Generating three-dimensional structures from a two-dimensional slice with generative adversarial network-based dimensionality expansion," *Nature Machine Intelligence*, vol. 3, pp. 299–305, apr 2021.

[242] Y. Han, R. J. Griffiths, H. Z. Yu, and Y. Zhu, "Quantitative microstructure analysis for solid-state metal additive manufacturing via deep learning," *Journal of Materials Research*, vol. 35, pp. 1936–1948, aug 2020.

[243] K. Matouš, M. G. Geers, V. G. Kouznetsova, and A. Gillman, "A review of predictive nonlinear theories for multiscale modeling of heterogeneous materials," *Journal of Computational Physics*, vol. 330, pp. 192–220, feb 2017.